Time-Resolved Fluorescence Techniques for the Development and Characterization of Genetically-Encoded Biosensors

by

Brett L. Fiedler

B.S., State University of New York at Geneseo, 2011

A thesis submitted to the

Faculty of the Graduate School of the

University of Colorado in partial fulfillment

of the requirements for the degree of

Doctor of Philosophy

College of Arts & Sciences Department of Chemistry & Biochemistry

2017

This thesis entitled:

Time-Resolved Fluorescence Techniques for the Development and Characterization of Genetically-Encoded Biosensors.

written by Brett L. Fiedler

has been approved for the College of Arts & Sciences Department of Chemistry and Biochemistry

_____

Ralph Jimenez

_____

Amy E. Palmer

Date_____

The final copy of this thesis has been examined by the signatories, and we find that both the content and the form meet acceptable presentation standards of scholarly work in the above mentioned discipline.

Fiedler, Brett L. (Ph.D., Physical Chemistry)

Time-Resolved Fluorescence Techniques for the Development and Characterization of Genetically-Encoded Biosensors.

Thesis directed by Prof. Ralph Jimenez

Fluorescent biosensors are important measurement tools for *in vivo* quantification of pH, concentrations of metal ions and other analytes, and physical parameters such as membrane potential. Both the development of these sensors and their implementation in examining cellular heterogeneity requires technology for measuring and sorting cells based on the fluorescence levels before and after chemical or physical perturbations. We developed a droplet microfluidic platform for the screening and separation of cell populations on the basis of the *in vivo* response of expressed fluorescence-based biosensors after addition of an exogenous analyte. Screening with this instrument reveals increased heterogeneity in an array of targeted Zn^{2+} biosensors in HeLa cells that helps shed light on the complexities of these sensors in different chemical environments. Subsequently, the instrument is used to screen and assess diversity in a number of HeLa-cell based genetic linker libraries for a family of genetically-encoded Zn^{2+} sensors. Progress on sensor characterization is made using time-resolved fluorescence techniques to advance a deeper molecular understanding of these sensors to guide further development.

Dedication

For Mom, who saw who I could be.

For Dad, who drove who I would be.

For Helen, who believed in who I became.

Acknowledgements

I would like to acknowledge and thank those who took part in the journey that brought me here, whether only for a stroll or for the full trek. I'll begin with my advisor, Ralph Jimenez, who has supported me through these six years. At every turn, Ralph would ensure that I had a rich graduate career, both scientifically and personally. He always made sure he was available when I needed help and allowed me the independence to push forward in my own pursuits. It has been an honor to work with him. I would also like to show my appreciation for Amy Palmer. Amy treated me as a member of her group and included me in every meeting and celebration. She was always available to be a second advisor whenever I needed it and for that I thank her.

I would like to thank all those at CU that I have come to know over these years. I thank the Jimenez group, both past and present for their support and putting up with the amount of biology I forced on them. In particular, I acknowledge Felix Vietmeyer for his part as friend and mentor even after his time as a labmate. I thank the Palmer group for their conversation, endless willingness to help, and putting up with the amount of physics I forced on them. I thank the lasting friends I've made at CU: Jasper Cook, Carla and Steele Reynolds. Even after they've gone off to other ventures, I can count on them every day. I thank the PER department and those involved with PISEC for enriching the last few years of graduate school and welcoming me in.

Lastly, I would like to thank my family for their unstoppable belief that I could accomplish any goal I put before myself, even from halfway across the country. My father reminds me often that I am the first in my family line to pursue a Ph.D and I am proud to take that mantle. Though she is not here, my mother was always proud of my academic pursuits and I take solace in knowing she would be proud of me now. I would be nowhere without my wife, Helen. She experienced the challenges that come with being the spouse of a doctoral student and never backed down from being the pillar that held me up.

Contents

Chapter 1 – Introduction

1.1 Fluorescent Proteins 1

1.2 Genetically Encoded Biosensors 2

1.3 Quantitative Use of FRET Biosensors 3

1.4 Genetically Encoded Zn^{2+} Biosensors 9

1.5 Strategies for FRET Biosensor Optimization 13

1.6 Conclusions 16

Chapter 2 - Methods and Instrumentation

2.1 Publication Note 17

2.2 Microfluidics 17

2.2.1 Design Considerations 17

2.2.2 Droplet Generation 19

2.2.3 Reagent Mixing 22

2.2.4 Droplet Occupation 24

2.2.5 Droplet Sorting 26

2.2.6 Microfluidic Fabrication 29
2.3 Experimental Design 30
2.3.1 Optical Configuration 30
2.3.2 Pressure Driven Flow Configuration 33
2.3.3 Electronics 34
2.3.4 Sample Preparation and Instrument Operation 36
2.3.5 Cell viability 42

Chapter 3 - Droplet Microfluidic Flow Cytometer for Sorting on Transient Cellular Responses of Genetically-Encoded Sensors

3.1 Publication Note 44
3.2 Motivation 45
3.3 Experimental Setup 46
3.3.1 Sensor Constructs 46
3.3.2 Design of ZapCV2 and ZapCV5 Zn^{2+} sensors 47
3.3.3 In vitro characterization of ZapCV2 and ZapCV5 47
3.3.4 Cellular imaging for in vivo calibration 49
3.3.5 Sample Preparation 51
3.3.6 Microfluidic Design and Experiment Parameters 52
3.4 Calibration experiments for FRET sensors 53
3.5 Tracking cells through pair-matching 57
3.6 Time-resolved differentiation of ZapCV2/ZapCV5 sensor mixture 59
3.7 Sorting of a mixed population 62
3.8 Impact of throughput and operation on instrument applications 66
3.9 Conclusions 73

Chapter 4 - Systematic Evaluation of ER Sensors and Development of a Sensor Linker Library

4.1 Publication Note and Author Contributions 74

4.2 Genetically Encoded Zn^{2+} Sensors Targeted to Subcellular Organelles 74

4.3 Experimental Setup 76

4.3.1 ER Sensor Cloning and Cell Culture 76

4.3.2 Library Cloning 77

4.3.3 Mammalian Cell Culture for Libraries 79

4.3.4 Viral Transduction for Libraries 79

4.3.5 Genomic DNA Extraction 81

4.4 Zn^{2+} Sensor Response in Subcellular Organelles 82

4.4 Heterogeneity in the Unbound State 82

4.5 Dynamic Response of ER and Cytosol Targeted Sensors and Sensor Variability 91

4.6 Generation of Linker Randomized Targeted Zn^{2+} Sensor Libraries 94

4.6.1 Library Rationale 94

4.6.2 Library Design and Selection Process 97

4.6.2 Initial Library Screening and Platform Iteration 100

4.7 Microfluidic Screening and Initial Sorting of Sensor Libraries 104

4.7.1 Pro/Ser Library 104

4.7.2 VVC1-2 Library 104

4.7.3 VVC3 Library 107

4.7.4 VVC1-2 Sort and Troubleshooting 107

4.8 Conclusions and Future Directions 113

Chapter 5 - Time-Resolved Photophysical Characterization of Zn^{2+} FRET Sensors

5.1 Time-Resolved Fluorescence of Genetically-Encoded Sensors 114

5.1.1 Fluorescence Lifetime Measurements 114

5.1.2 Fluorescence Anisotropy 116

5.1.3 Fluorescent Proteins as Anisotropy Probes 120

5.1.4 Time-resolved FRET 120

5.2 Experimental Setup 123

5.2.1 Sample Preparation 123

5.2.2 Instrumentation 124

5.3 Fluorescence Anisotropy Calculations 126

5.4 Time-resolved Fluorescence Results 131

5.4.1 TRF of a Small Molecule Dye 131

5.4.2 Effect of His-tag on ECFP Zn^{2+} Response using TRF 133

5.4.3 Time-resolved Fluorescence Measurements on Zinc Sensors 137

5.4.4 Time-resolved Fluorescence Anisotropy Results for Zinc Sensors 141

5.5 Conclusions and Future Directions 151

Bibliography 152

Appendix

Appendix A - Protocols 166

A.1 PDMS Device Manufacturing Protocol 166

A.2 Microfluidic Operation Protocol 171

Appendix B - Code 175

B.1 Microcontroller Code 175

B.2 Mathematica Code for Anisotropy Calculations 191

B.3 Mathematica Code for Microfluidic Device 195

Tables

Table

3.1 ZapCV2/ZapCV5 Sorting Results 64

4.1 FRET Distribution Statistics for ZapCY1, eCALWY-4, and e-ZinCh-2 89

4.2 FRET Distribution Statistics for Screened Libraries 109

5.1 Cyan and Yellow Fluorescent Protein Absorption Coefficients 123

5.2 Fluorecein Dianion Anisotropy Fit Results 131

5.3 ECFP Anisotropy Fit Results 135

5.4 ZapCY1 TCSPC Fit Results 140

5.5 eCALWY-4 TCSPC Fit Results 140

5.6 eZinCh-2 TCSPC Fit Results 140

5.7 ZapCY1 FRET Channel Anisotropy Fit Results 146

5.8 ZapCY1 CFP Channel Anisotropy Fit Results 146

5.9 eCALWY-4 and eZinCh-2 FRET Channel Anisotropy Fit Results 150

5.10 eCALWY-4 and eZinCh-2 CFP Channel Anisotropy Fit Results 150

Figures

Figure

1.1 Jablonski Diagram for FRET 6

1.2 Crystal Structure of ECFP 7

1.3 Zap family Zinc Sensor Schematic 12

2.1 Droplet Failure in Absence of Surfactant 21

2.2 Y-shaped Mixing Junction 23

2.3 Poisson Distrubution and Single Cell Droplet Occupation 25

2.4 Droplet Sorting and Droplet Sorting Junction 28

2.5 Droplet Merging After Dilelectrophoretic Field Exposure 29

2.6 Epifluorescence Microscope and Microfluidic Implentation 32

2.7 Raw Signal from HeLa Cells Passing Interrogation Beam 33

2.8 Microcontroller Setup and Streaming Data Trace 35

2.9 Sensor Expression in HeLa-S3 and HeLa Cells 37

2.10 Image of Inlet with Cell Aggregation 39

2.11 OptiPrep Optimization Experiment Images 41

3.1 ZapCV2/ZapCV5 Schematic and *In Vitro* Titrations 50
3.2 Optical Configuration and Microfluidic Assay Schematic 54
3.3 ZapCV2 and ZapCV5 Calibrations 55
3.4 Schematic Comparing Calibrations to Microfluidic Assay 56
3.5 Schematic of Sorting Logic and Example Time Delay Histogram 60
3.6 FRET Histograms for Zinc Sensor Mixtures for Dynamic Range Differentation 61
3.7 Kinetic Resolution of ZapCV2 and ZapCV5 63
3.8 Pairmatched Scattergram of Mixed ZapCV2/ZapCV5 Sorting Experiment 65
3.9 Fluorescence Images Demonstrating Sorting Enrichment 66
3.10 Zinc Concentration Profile in Mixing Junction 70

4.1 FRET Histograms for ZapCY1 in Three Cellular Compartments 83
4.2 Calibrations for Three Zinc Sensors in the ER and Cytosol 84
4.3 ZapCY1 Calibration Illustrating Response Time Window in Microfluidic 86
4.4 FRET Histograms for ZapCY1, eCALWY-4 and eZinCh-2 88
4.5 Fluorescence Images and Western Blot of Three Zinc Sensors 90
4.6 Intensity Scattergram and Histograms of Three Zinc Sensors 93
4.7 Workflow for Library Generation and Sorting 99
4.8 FRET Histogram for Transiently Expressed ER-ZapCY2 100
4.9 FRET Histogram for Virally Transduced Expression of ER-ZapCY2 101
4.10 Sequence Homology for ECFP and mCitrine 102
4.11 FRET Histogram for ER-OptiZap 103
4.12 Cytometry Data for Pro/Ser Library 105
4.13 Cytometry Data for VVC1-2 Library 106
4.14 Cytometry Data for VVC3 Library 108

4.15 Sorting Data for VVC1-2 Library 110

4.16 DNA Gels for gDNA PCR Amplification of Zinc Sensor Sequence 112

5.1 Molecular Definitions for FRET 119

5.2 Overlaid ECFP and mCitrine Absorption and Emission Spectra 125

5.3 Time-Resolved Anisotropy Calculation Results 130

5.4 Fluorescein Dianion TCSPC and TRFA Histograms 132

5.5 Steady-State Anisotropy of Zinc Sensors 134

5.6 TCSPC Histograms for TEV Treated ECFP 136

5.7 TCSPC Histograms for ZapCY1 138

5.8 TCSPC Histograms for eCALWY-4 139

5.9 TCSPC Histograms for eZinCh-2 139

5.10 Raw FRET TRFA Traces of Zinc Sensors 141

5.11 TRFA Traces for ZapCY1 in the FRET Channel 144

5.12 TRFA Traces for ZapCY1 in the CFP Channel 145

5.13 TRFA Traces for ZapCY1 in the FRET Channel 148

5.14 TRFA Traces for eCALWY-4 and eZinCh-2 in the CFP Channel 149

Chapter 1

Introduction

1.1 Fluorescent Proteins

The discovery of the fluorescent protein shuttled in an unparalleled shift in the way researchers studied cellular structure and processes *in vivo*. Beginning with the green fluorescent protein (GFP) derived from *Aequorea victoria*, it was possible to avoid the problems associated with the loading of cells with exogenous small molecule dyes, as well as difficulties with dye localization to subcellular organelles. GFP is a highly structured, cylindrical protein characterized by an 11-stranded beta barrel and a buried chromophore formed by the autocatalytic reaction of three amino acids (Ser65-Tyr66-Gly67) in aerobic conditions.[1] The chromophore is non-fluorescent in the absence of a rigidifying environment (e.g. embedded within an amino acid pocket or frozen in a solvent) and highly sensitive to changes in that environment.[2,3] This has allowed for extensive study and alteration of the chromophore environment to tune its spectral properties through mutation of surrounding amino acids. GFP is easy to incorporate into the genome of any organism compatible with genome editing and is amenable to the inclusion of targeting sequences to localize the protein to subcellular organelles.[4]

The existing palette of fluorescent proteins (FPs) has expanded substantially through the discovery of similar proteins from other organisms, as well as mutations to the chromophore and its surrounding amino acids to change its electronic structure and consequently the absorption and emission wavelengths. The available range of fluorescent proteins now expands from the near-UV to the near-infrared with notable visible categories including the blue, cyan, green, yellow, orange and red fluorescent proteins.[5] This has enabled the ability to generate experiments with multiplexed FPs or FPs and dyes. Additionally, the segregation of FPs into separate but overlapping optical windows have made them ideal candidates for utilization in Förster Resonance Energy Transfer (FRET) experiments. Fluorescent proteins are simple to incorporate in fusion protein constructs, making them invaluable for tagging intracellular proteins or adaptation as biological analyte sensors (biosensors).[6–9]

1.2 Genetically Encoded Biosensors

Spatiotemporal investigations of molecular species are among the cornerstones on which the modern understanding of cellular function is built. Biosensors based on fluorescent proteins have been constructed to quantify free levels of many important cellular analyte including Ca^{2+}, pH, NAD^+/NADH, ADP/ATP, cGMP, halides and many metal cations.[1,6,10,11] Sensing is achieved by a number of mechanisms including, but not limited to Förster Energy Resonance Transfer (FRET) and emission intensity or wavelength shifts modulated by conformational changes and environmental sensitivity.[12] Full characterization of a biosensor's dynamic range, a critical parameter for determining its usefulness, requires fluorescence measurements prior to and after cellular perturbation. These fluorescence changes *in vivo* typically occur on the tens of milliseconds to several minutes timescale, for example in response to a signal cascade, such as

Ca^{2+} and IP_3 oscillations after stimulation by glutamate[13] or cGMP production in response to NO[14,15]; transient perturbations in the cellular environment, such as cellular pH changes and reactive oxygen species bursts[16,17]; or changes in membrane potential.[18,19] In addition to biosensing, cellular control *via* optogenetic tools intrinsically involves the measurement of transient responses. For example, when photoexcited at 488 nm, components of the CRY2 optogenetics system cluster on the second timescale and then revert to a diffuse state after exposure is terminated.[20,21] In all these cases, quantifying the heterogeneity of these responses and determining whether it is intrinsic to the sensor or to genetic or epigenetic cell variability is a difficult subject of investigation which is impeded by the low-throughput microscopy techniques traditionally employed in this field. Beyond applications to existing biosensors, development of next-generation sensors and optogenetics tools would be facilitated by the high throughput screening and sorting of genetic libraries based on transient cellular response.

1.3 Quantitative Use of FRET Biosensors

This thesis will focus specifically on the use of sensors utilizing FRET as their sensing mechanism. Measurements of FRET sensors in live cells generally involve using standard widefield fluorescence microscopy or confocal microscopy, as this is the most available instrumentation. As such, FRET ratios are generally measured by sensitized emission, rather than more complicated methods such as lifetime or anisotropy microscopy. Sensitized emission is measured by exciting at the donor wavelength and measuring the emission at the donor detection window (CFP donor) and the acceptor detection window (FRET channel). FRET ratios, specific to CFP/YFP sensors are defined as:

$$R = \frac{I_{FRET} - I_{FRET\ bkgd}}{I_{CFP} - I_{CFP\ bkgd}} \quad (1.1)$$

where I is the intensity in the respective channels and 'bkgd' indicates the background signal in that channel. Determining the dynamic range of a sensor requires the measurement of R during depletion of the analyte, denoted R_{min} or R_{apo}, and again during saturation of the analyte, denoted R_{max}. The dynamic range can then be defined either as the ratio

$$DR = R_{max}/R_{min}, \quad (1.2)$$

the difference

$$DR = R_{max} - R_{min}, \quad (1.3)$$

or the normalized ratio

$$DR = (R_{max} - R_{min})/R_{min}. \quad (1.4)$$

The first formulation is the one most often cited in the literature. Put together, the measurement of a resting R, R_{max} and R_{min} are the basis of a calibration experiment. The fractional saturation, Y, can be also be determined at an arbitrary value of R between these bounds in a one site binding model as

$$Y = (R - R_{min})/(R_{max} - R_{min}). \quad (1.5)$$

Combining Y with the measured *in vitro* K_D for the sensor results in a measured concentration of the ligand, given that the concentration falls within a factor of 10 on either side of the K_D. This is one reason an array of sensors must be produced and no one sensor for a given analyte is sufficient or appropriate in all biological contexts.

The quantitative use of intramolecular FRET sensors is complicated by numerous factors as mentioned in the previous section. First, the dynamic range of the sensors is dependent on the parameters that determine the FRET efficiency between the donor/acceptor pair. FRET is the radiationless transfer of energy from one singlet to a coupled singlet state, where the rate of

transfer is steeply dependent on both the distance and orientation between the transitions dipole moments (TDMs) of the donor and acceptor chromophore. A simplified Jablonski diagram for the relevant transitions for the ground and first excited state of the donor and acceptor is shown in Figure 1.1. The formulation of the FRET rate, k_T, is

$$k_T = \left(\frac{9000 \ln 10}{128 \pi^5 n^4 N_A}\right) \frac{\kappa^2 Q_D J(\lambda)}{R^6 \tau_D} \tag{1.6}$$

where n is the refractive index of the surrounding media, N_A is Avogadro's number, κ^2 is the orientation factor based on the TDMs of the FRET pair, Q_D is the fluorescence quantum yield of the donor, $J(\lambda)$ is the normalized overlap integral between the emission of the donor and absorption of the acceptor, R is the distance between the chromophores, and τ_D is the fluorescence lifetime of the donor. For any given FRET pair, all terms but κ and R are constants. Thus, for any FRET pair, to optimize the dynamic range of a sensor, both the distance and orientation between the two fluorescent proteins must change substantially. Fluorescent proteins present an immediate drawback when used for FRET for the same reason the chromophore shows remarkable resilience to environmental conditions, namely the protective amino acid barrel. This barrel makes the protein relatively large compared to the length scales over which FRET takes place (nm). The width of the barrel is ~2 nm for most FPs, meaning two FPs could not get closer than 2 nm, restricting the value of R in the high FRET case. See Figure 1.2 for the top-down view of a fluorescent protein with chromophore and barrel distances visible. The implications of the distance and orientation factor are discussed in detail in Chapter 5.

Secondly, all three portions (donor, acceptor, binding domain) of the construct are sensitive to environmental factors including pH, oxidation/reduction, and crowding to name a

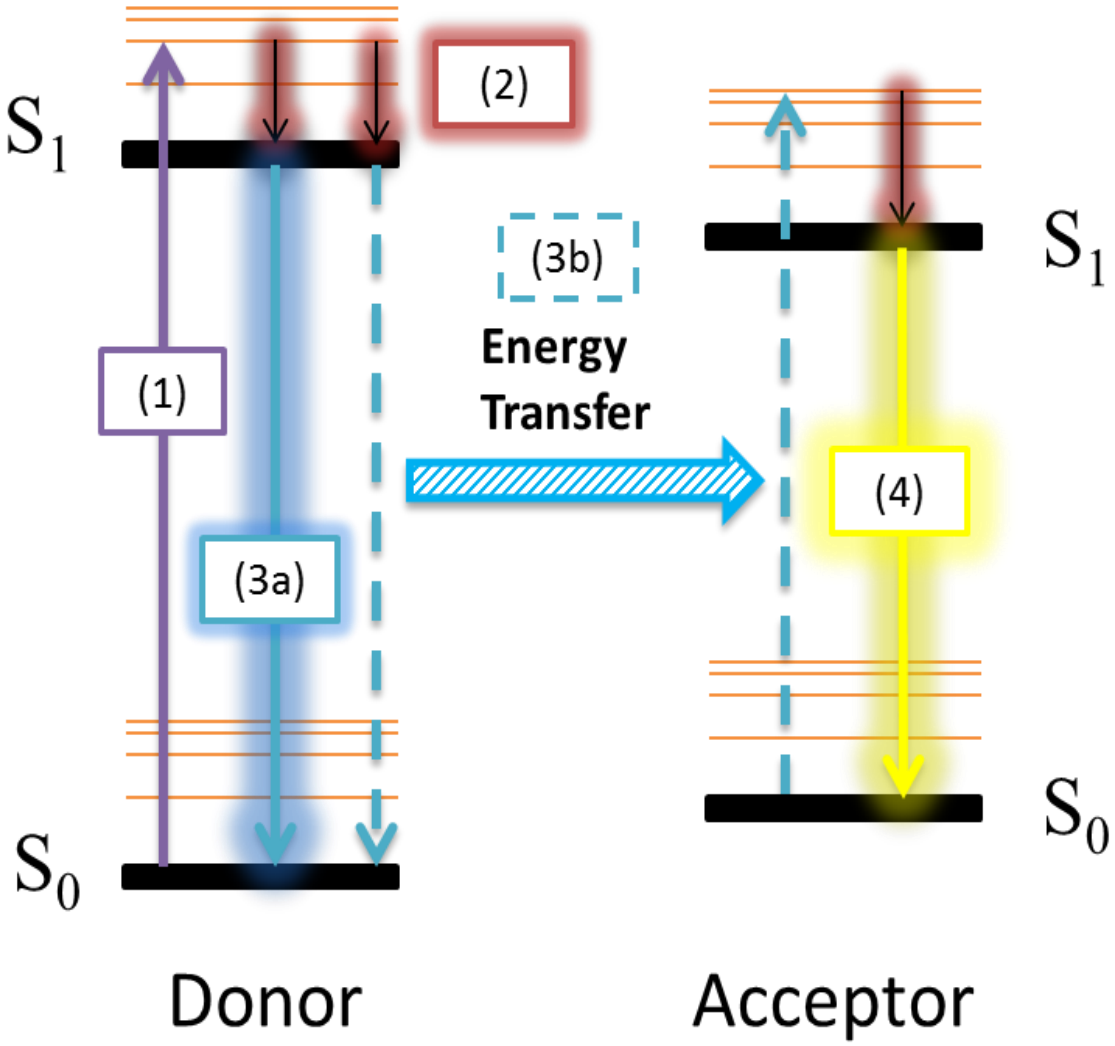


Figure 1.1. Jablonski diagram for the relevant transitions for the ground and first excited state of the donor and acceptor. Transition are shown for (1) the attosecond absorption of a photon for the donor, (2) femtosecond to picosecond vibrational relaxation to the first excited state for donor, (3a) piscosecond–nanosecond donor fluorescence, (3b) picosecond–nanosecond radiationless energy transfer, and (4) picosecond–nanosecond acceptor fluorescence.

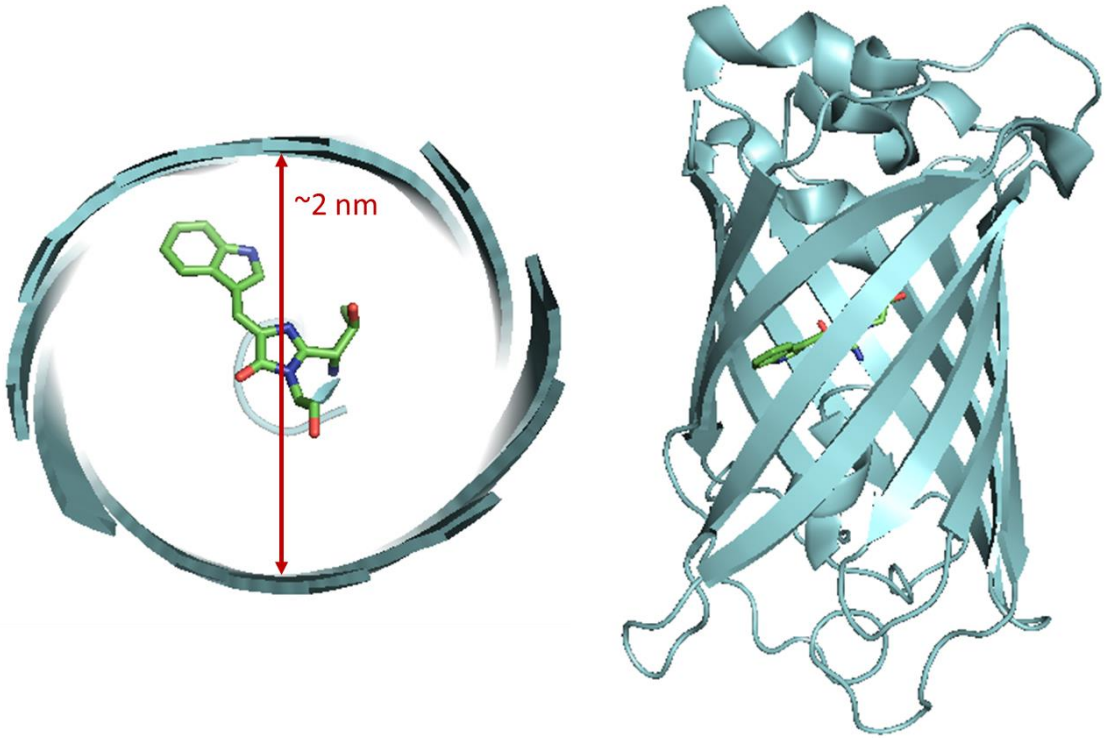


Figure 1.2. Crystal structure of ECFP (top-down view and side view). The barrel of fluorescent proteins is fairly consistent across variants with a minimum radius of ~1 nm. This results in a minimum separation of ~2 nm between 2 juxtaposed fluorescent proteins. PDB 2WSN.

few. The most popular FRET pair is the CFP/YFP pair with ECFP remaining the most prevalent donor despite a number of improved variants now available. Extensive work has been done to show that ECFP has high sensitivity to a number of biological molecules and ions through interaction with outward facing amino acids (His148, Tyr145).[22] The YFP family, especially those that have been circularly permuted, such as mVenus, show high sensitivity to pH.[23] FPs, originally derived from dimers, have shown tendencies to form weak homodimers and tetramers even after mutations meant to convert them to monomeric forms.[2] The analyte binding domains, especially those responsible for binding metal ions, are generally pH sensitive and redox sensitive. Zn^{2+} specific sensors often contain cysteine residues with their redox capable sulfihydryl groups and potential for disulfide bond formation. All of these factors must be accounted for when optimizing FRET sensors for localized *in vivo* measurements.

The ideal sensor is difficult to achieve given the number of variables needed to control. In a perfect world, a sensor would show high brightness (above background fluorescence of endogenous autofluorescence), high photostability (does not bleach over the course of the experiment) with no photoconversion, fast maturation (sensor is quickly and completely expressed in as many organisms as possible), monomeric (does not dimerize or aggregate unless it is a feature of the sensor), environmentally insensitive (only changes due to ligand concentration contribute to signal change) and, lastly, a large dynamic range (high signal to noise).

1.4 Genetically Encoded Zn^{2+} Biosensors

The field of Zn^{2+} homeostasis is of particular interest due to the implication of Zn^{2+} in all aspects of cellular function. Zn^{2+} has long been known to play a critical role in biological function, ranging from a cofactor in enzymes, a structural component in many proteins, and a necessary component of many transcription factors.[24] Studies have shown Zn^{2+} release in glutamatergic neurons[25,26], as well as a discovery of a Zn^{2+} 'spark' accompanying expected Ca^{2+} dynamics during human egg activation.[27,28] These discoveries also implicate Zn^{2+} as a signaling ion, shedding a whole new light on Zn^{2+} in biology. Fluorescent Zn^{2+} sensors are invaluable in their ability to spatially and dynamically resolve Zn^{2+} homeostasis *in vivo*. There are a number of existing platforms with which to make these measurements, each with its own advantages and pitfalls.

The first molecules made available for *in vivo* Zn^{2+} monitoring were small molecule dyes combined with a specific metal chelator for intensity-based sensing. Such Zn^{2+}-dependent fluorescent sensors are now available over a range of binding constants, wavelengths, and brightness (molar extinction coefficient × fluorescence quantum yield).[29] These sensors also boast impressive dynamic ranges from 2-200-fold. Ratiometric sensors also exist, which utilize emission changes at different wavelengths, albeit with smaller dynamic ranges. While customization of small molecule sensors is extensive and invaluable for in vitro Zn^{2+} determination, their use in vivo is hampered by the need for the molecules to bypass the plasma membrane and localize to the cellular compartment of interest. The uptake and localization of these dyes is complex and heterogeneous. There are many strategies for membrane permeation including the incorporation of a cleavable AM ester to the molecule or microinjection.[7] Many dyes show significant mislocalization and aggregation within cells due to a number of

environmental factors outside of a researcher's control.[30] Several properties influence the localization of a sensors including molecular charge, lipophilicity, and solubility in the cellular environment.[29] In some cases, these properties can be manipulated to influence accumulation in specific organelles, such as the use of sensors designed from a positively-charged rhodamine derivative, which is driven across the negative membrane potential of the mitochondria.[31] Controlling the amount of dye that is present in the cells presents an additional challenge. With respect to measuring metal ion homeostasis, which is effectively measuring the unbound concentration of metal ions in the cell, accumulation of excess sensor can deplete free ion concentration. Depletion of the free ion pool can sway ion homeostasis and greatly affect cellular function.[9,32]

Genetically encoded Zn^{2+} sensors generally incorporate a fluorescent protein as a fluorescent readout, either intensity-based or wavelength ratiometric, and a Zn^{2+} binding domain. FRET-based sensors undergo a conformational change upon Zn^{2+} binding such that the distance and orientation between the FPs is altered, changing the measured FRET ratio measured as the $I_{FRET/}$. The first fully genetically encoded Zn^{2+} sensor were based on the FRET based Ca^{2+} sensors. These incorporated a ECFP/Citrine FRET pair flanking a single zinc finger binding domain for Zn^{2+} measurement in mammalian cells.[33] Since then, several groups have introduced a variety of platforms for FP-based FRET-mediated Zn^{2+} sensing. Two popular sensor platforms, the eCALWY family and the eZinCh family, were generated by the Merkx lab utilizing different Zn^{2+} binding motifs and modifications to the FPs to optimize the FRET properties of the sensors.[34,35] These sensors will be discussed in more detail in Chapter 4. Other genetically encoded Zn^{2+} sensor platforms exist, including but not limited to a hybrid platform utilizing a red FP and a small molecule dye, intensity-based single FP sensors based on Zn^{2+} binding induced

chromophore quenching, and a sensor utilizing bioluminescence resonance energy transfer.[36–38] These sensors are currently underutilized outside of the labs in which they were generated.

The work presented in this thesis was performed in close collaboration with the Palmer lab at CU-Boulder, which generates genetically encoded Zn^{2+} sensors and utilizes them to study Zn^{2+} dynamics in an array of cell lines and their subcellular organelles. The FRET sensors constructed by this group include CFP/YFP sensors, as well as the red-shifted sensors using GFP/RFP, across a range of affinities and dynamic ranges. The sensors developed to date share a zinc finger binding domain consisting of either the mammalian derived zinc finger Zif268 or the first two fingers of the yeast derived Zap1 zinc finger. A schematic of the Zap1 containing sensors is found in Figure 1.3. The zinc finger has been shown to be largely unstructured in the absence of Zn^{2+}, taking on the characteristic zinc finger structure upon binding.[39]

The panel of genetically encoded Zn^{2+} sensors is quickly growing, but all current sensors share a number of problems complicating their use. First and foremost is a lack of dynamic range. The goal of these sensors is, when combined with the affinity of the sensor, to use the full range of the sensor to establish a fractional saturation (% of sensor bound to ligand) and correlate that with a Zn^{2+} concentration. When the dynamic range of a sensor is small, it is difficult to distinguish response from the noise. It was shown that a decrease in dynamic range can affect the measured fractional saturation for sensors with similar affinity.[40] Furthermore, measurements with sensors of small dynamic range, may miss important signaling events or transient fluxes that could be mistaken for noise. It has been rigorously shown that these sensors respond differently, often less well, when targeted to organelles other than the cytosol.[41,42] This indicates the importance of studying these sensors in varying environmental conditions including the variance of pH, redox, and molecular crowding. These sensors should be optimized for the

cellular environment for which they will be used. This topic will be discussed and analyzed in more detail with respect to the FRET-based Zn^{2+} sensors in Chapter 4. A keen molecular understanding of these constructs will be necessary for developing more robust and high dynamic range sensors.

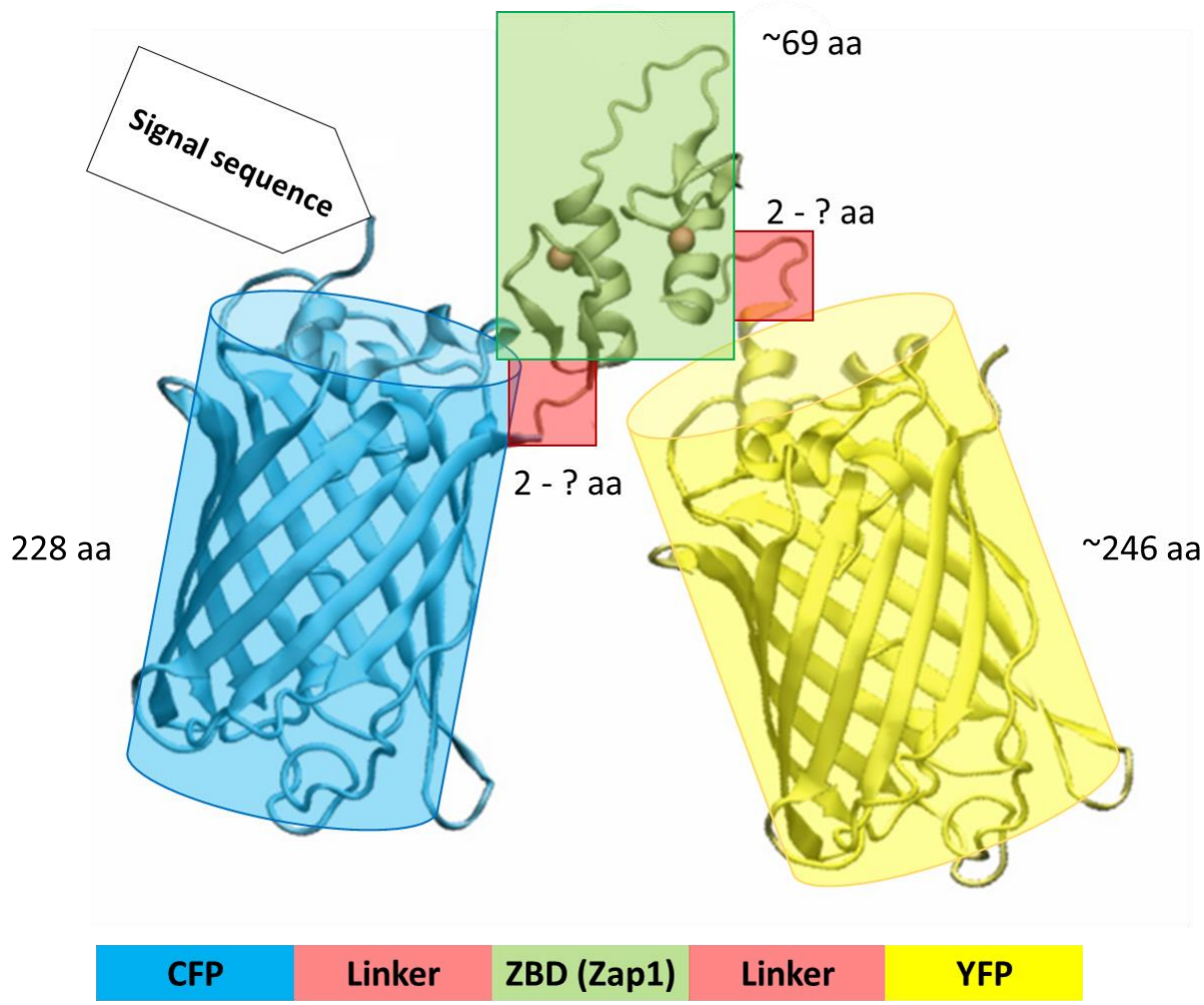


Figure 1.3. Sensor schematic for the Zap family of Zn^{2+} sensors. The sensors incorporate ECFP as the FRET donor and either mCitrine or mVenus circularly permuted at position 173 as the acceptor. The FPs are connected to the Zap1 Zn^{2+} binding domain by small amino acid linkers designated by the nucleic acid restriction sites and small glycine/serine repeats. Sizes are shown next to each domain in number of amino acids (aa).

1.5 Strategies for FRET Biosensor Optimization

FRET biosensor optimization can be performed using a myriad of methods. It is common for initial construction of a sensor to consist of choosing a FRET pair and sandwiching it around a domain known to bind the ligand of interest. While this may generate a functional sensor, the mutations required to increase dynamic range and sensor kinetics are not well understood for every sensor platform. It is common to make incremental mutations to the FPs, linker regions, or binding domains with literature precedent and test each variant generated.[32] This method rarely samples the full space of potential mutations that could lead toward an optimized sensor and is slow due to the laborious manual screening process of expressing and calibrating each variant. An example of this type of methodology that has resulted in significant improvement is the circular permutation of the acceptor domain in genetically encoded calcium indicators.[43] Another includes the simple lengthening of the linker region in a family of Zn^{2+} sensors.[34]

Higher throughput methods for sensor optimization employ large libraries of mutations. The mutations result in randomization of the amino acids in regions of the sensor guided by rational engineering of a parent sensor and literature precedent. Manually screening large library sizes ($>10^2$) is laborious, requiring expression and *in vivo* testing of each mutant. The process of screening and selecting improved variants benefits greatly from automation via high-throughput methods. This is further complicated by transient responses of many sensors, which required more vigilant monitoring after addition of ligand. The ideal method would probe the FRET state of the molecule both before and after exposure to ligand with adequate mixing times (msec-sec) to assess the full dynamic range of the sensor. Additionally, this method would allow for sensor screening in mammalian cells which are of great interest to researchers due to their use in

medicine. An overview of the instrumentation available to screen large libraries of genetically encoded fluorescent sensors is detailed below.

Fluorescence activated cell sorters (FACS) and flow cytometers are laser-based technologies that probe cell suspensions at the single cell level based on their fluorescence or light-scattering properties. This is often used for cell counting or fluorescently-labeled biomarker detection.[44] In the case of FACS, cells with desired optical properties can also be physically separated from the initial suspension. These technologies are highly optimized for speed (thousands of cells analyzed per second), and single-time point, multi-wavelength excitation and emission measurements, but they are not suitable for introducing analytes and measuring transient biosensor responses on the msec-to-sec timescale. Commercial instruments operate at flow velocities of m/s, with a maximum delay of hundreds of microseconds between laser excitation points. Customized flow cytometers adapted for kinetic measurements on the order of ms to minutes have been developed.[45–48] In these instruments, the addition of electronic timers, mixing networks during sample introduction, and nozzle modifications have enabled reagent mixing. These developments introduced the capability to measure population shifts as a function of delay time and reagent concentration by in-line dilution, but they do not offer cell-by-cell response measurements or sorting.

Plate-based colony screening platforms in which each colony represents a single member of a library offer a robust method for determining and improving sensor dynamic range, but they are typically limited to screening or selection in bacterial or yeast cell lines. Plate screening technology measures the fluorescence intensity changes on the colony level through image analysis after chemical permeabilization and addition of ligands or chelators.[49–51] While automation of colony plate screening offers the potential for measurements on large sensor

libraries (> 10^3 clones), current technology employs manual chemical application and image capture which is inherently labor and time intensive. This technology does not permit measurements of single cells and averages out cell-to-cell variability, thereby decreasing overall sensitivity. Furthermore, techniques for uniformly and reproducibly applying solutions to the colonies are still under development. Depending on the application technique, reported coefficients of variation for the FRET ratio changes range from 67% when a manual sprayer was employed for dispensing ligand to 37% when a spraygun with a lasersight was used.[49] Some of the limitations in plate screening technology could be improved with the use of high throughput-high content microscopy which could allow for single-cell measurements, though the implementation of cell selection in this technology is not straightforward. Finally, it is known that sensor performance varies between organisms,[52] and even within different cellular compartments of the same organism.[42] Technology for screening and selection of biosensors based on responses in mammalian cell lines has not yet been reported.

Droplet microfluidics flow cytometry provides potential throughput comparable to FACS while vastly expanding the types of single-cell measurements possible.[53–55] Most efforts involving time-dependent phenomena capitalize on the stable encapsulation of cells to enable directed evolution of enzyme function, which requires incubation of single cells for minutes to hours, or drug toxicity assays also on timescales of hours.[56] These assays employ single cell encapsulation, incubation, and droplet reinjection in separate devices,[57,58] so responses are not individually tracked. Designs incorporating minute to hour-long delay lines for monitoring kinetics have been developed and implemented for enzymatic assays in picoliter reaction volumes, but thus far do not provide single-cell tracking and sorting.[59–61] Prior to this thesis work there has been no report of a single microfluidic device that incorporates all three aspects required for biosensor

characterization and development: on-chip mixing for initiation of a cellular response, interrogation before and after the reaction, and sorting based on the response of each cell prior to the publication of this instrument.

1.6 Conclusions

Genetically encoded FRET sensors have been derived for a wide range of biological ligands, but the vast majority suffer from a small dynamic range. While there are existing strategies to improve these sensors, complications arise when the sensor response cannot stably report both the analyte free and analyte bound form for long times. The work in this thesis presents alternative, high throughput methodology for the characterization and optimization of the dynamic range of such sensors with a focus in the field of Zn^{2+} homeostasis. Furthermore, work towards a better molecular understanding of the current array of FRET-based Zn^{2+} sensors is presented.

In chapter 2, an in-depth discussion of the design principles guiding the creation of a time-resolved microfluidic cell sorter is presented. In chapter 3, the microfluidic sorter is applied to a set of previously designed Zn^{2+} sensors to verify its ability to sort on the basis of a time-resolved response to Zn^{2+} perturbation. In chapter 4, the microfluidic system is applied as a screening tool for heterogeneity and population analysis of the leading Zn^{2+} sensors in the endoplasmic reticulum (ER). This is followed by the construction and screening of a number of randomized linker libraries for the optimization of the Zap sensor family in the ER and cytosol. In chapter 5, the many factors that influence the behavior of these sensors at the molecular level is discussed. Progress in characterizing the orientational and time-resolved behavior of several Zn^{2+} sensors is presented.

Chapter 2

Methods and Instrumentation

2.1 Publication Note

Portions of this chapter were adapted from Fiedler, B. L. *et al.* Droplet Microfluidic Flow Cytometer for Sorting On Transient Cellular Responses of Genetically-Encoded Sensors. *Anal. Chem.* **89,** 711–719 (2017) and the corresponding Supplementary Information. Figures present in the publication are unmodified in this chapter.

2.2 Microfluidics

2.2.1 Design Considerations

The benefits of using microfluidic devices are derived from the micron-scale features that define their name, which include low volume use and a high level of fluid control. While this is not meant to be an exhaustive review of fluid dynamics at the microscale, the basics as they apply to the design of the microfluidic devices used during this thesis will be discussed. Interested readers are referred to thorough introduction to microscale fluid physics for microfluidics.[62] At this scale, the fluid behavior is simplified beyond the usual Navier-Stokes

formulation due to the lack of inertial forces present. The Reynold's number is the ratio of inertial forces to viscous forces and can be defined as,

$$Re = \frac{\rho u l}{\eta} \tag{2.1}$$

Where ρ is the fluid's density, u is the flow speed, l is the length scale, and η is the viscosity. For the typical buffers used in biological applications and nm - μm length scales used for microfluidics, even at speeds exceeding meters per second, *Re* will remain << 1. Fluid dynamics at this low Reynold's number are defined by viscous forces and this regime is known as laminar flow. Laminar flow is defined by its predictable nature, lacking the complicated flow dynamics and vortices present in the turbulent flow regime (*Re* > 1000). For microfluidics, this means that fluid motion in the channels is entirely governed by the applied force (pressure). If the force is reversed, the fluid motion will also be reversed returning it to its original state.[63] This allows for highly controllable and sophisticated microfluidic designs.

Device design for this work was initially based on the earlier work of Weitz *et al*.[57] The overall scale of the devices was designed to accommodate the size of cultured HeLa cells which have a diameter on the order of 15-20 μm when in suspension.[64] The total length of the devices from inlet to outlet is long to accommodate the use of long time delays between measurement regions and therefore steps were taken to decrease the overall resistance of the device and therefore the required driving pressure for a given fluid velocity. The resistance of a microfluidic device is determined by performing an Ohm and Kirchoff's laws type calculation in which each channel segment is assigned a resistance value and added either in parallel or series to determine total device resistance. The resistance of a rectangular channel can be calculated by[65]:

$$R = \frac{12\eta x}{(h^3 w)\left(1-0.630\frac{h}{w}\right)} \tag{2.2}$$

Where η is the viscosity of the medium, x is the length of the channel segment, w is the width of the channel segment, and h is the height of the channels. In 2D microfluidics, the height will remain constant across the design. It should be noted in the above equation that the resistance has a strong dependence on the height of the device. The resistance of the device used in this work was limited by keeping the designs between 40-50 μm in channel height to accommodate cell size. For the devices used in this work, the total device resistance was on the order of 1-10 $x10^{14}$ N s m^{-5}. Increasing the input resistance relative to the output resistance will increase the stability of the device as fluids will move naturally from high to low resistance. See Appendix B for example code for calculating the device resistance.

2.2.2 Droplet Generation

Droplet generation can be achieved by a number of different structures in microfluidics. Popular designs are a T-junction, flow-focusing junction, or a coaxial junction.[66] The flow-focusing junction was chosen for these devices due to the superior control of droplet size from sheering forces on both sides of the dispersed phase.[53,67] Droplets can be generated by a number of active methods including, but not limited to, the use of surface acoustic waves[68], pulsed laser excitation[69], and pneumatic chopping'.[70,71] Passive generation of droplets, including pressure driven, relies on the balance between surface tension and the shear forces introduced by the continuous phase (oil) on the dispersed phase (aqueous) and is separated into three regimes: squeezing, dripping, and jetting. The regime is determined by the capillary number (Ca = μU/γ, μ viscosity, U characteristic velocity, γ surface tension between water/oil interface), which increases from squeezing to jetting. Squeezing is characterized by the contact of the dispersed phase with the channels walls dominated by surface tension. Dripping is increasingly dominated

by shear forces. Jetting is visualized by a thread of dispersed phase past the droplet junction from which droplets begin generating. Droplet size is most controllable in the squeezing and dripping regimes. These are the regimes targeted in the devices for this work.

Droplet generation and stability in fluorinated oils (such as Novec 7500 or FC-40), which are known to be biocompatible with a range of organisms, is hindered without the addition of a fluorinated surfactant (fluorosurfactant). These surfactants decrease the surface tension to allow greater droplet control through external pressure modulation.[72] For purposes of droplet incubation (or where droplet-droplet contact is possible), the surfactants also prevent droplet merging. Many fluorosurfactants obtainable through commercial means are proprietary and the exact structure is not available, but extensive work has gone into detailing the synthesis of suitable and biocompatible fluorosurfactants.[73,74] The surfactants are most often characterized by a fluorophilic head (such as Krytox-FSH) and a hydrophilic tail (such as PEG). Initial studies (Chapter 3) in this thesis made use of a "Droplet Generator Oil" (BioRad) diluted 100-fold in Novec 7500 to concentrations in which droplet generation was observed. Later studies (Chapter 4) switched to a proprietary surfactant made by RAN Biotechnologies used at 0.1% w/v. The lack of a proper fluorosurfactant can lead to a failure of droplet formation as shown in Figure 2.1.

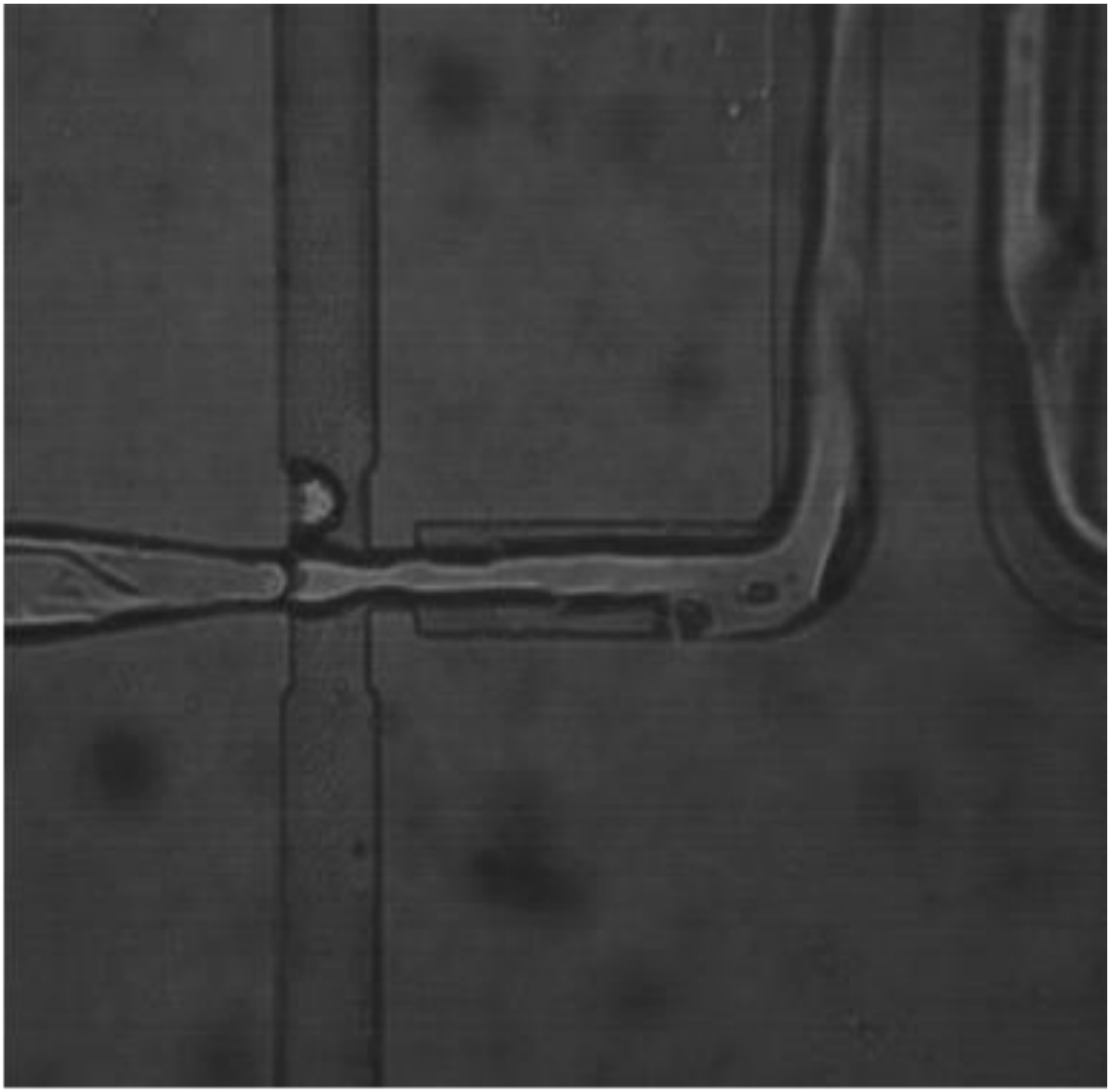


Figure 2.1. A microfluidic device using only Krytox-FSH as a surfactant. Droplet formation was not observed at all pressures tested.

2.2.3 Reagent Mixing

The implications of the laminar flow as it pertains to designing microfluidics extends to the mixing process. The lack of inertial forces and turbulence, in a straight channel where two solutions meet, means the mixing is dominated by diffusion. The characteristic mixing time $t = l^2/D$, where l is the distance over which mixing takes place and D is the diffusion coefficient for a particle, can be used as a rough estimate of the mixing time for small molecules in a straight channel where two solutions meet. The diffusion coefficient for small molecules is on the order of 10^{-5} cm^2/s, which corresponds to a diffusion time of 100 ms - seconds across 10-100 μm channels.

Mixing in fluidic channels with a finite fluid velocity becomes more complicated due to the uneven velocity of particles across the width of the channel. In pressure driven channels in the laminar regime, particles travel in a parabolic flow profile due to the no-slip boundary condition at the walls of the microfluidic channel (no fluid flow at the surface of an object).[63] This leads to enhanced diffusion across the channel and the calculation of an effective diffusion coefficient, $D_{eff} = l^2U^2/\sigma D$, where σ is a dispersion constant for the cross section of the channel equal to 0.0084 for approximately square channels and 1/210 for planar channels.[75] This enhanced diffusion is known as Taylor-Aris diffusion. Application of Taylor-Aris diffusion to our system using flow velocities on the order of 1-100 mm/s in 50-100 μm channels yields D_{eff} values that are 2 orders of magnitude higher than D. Analysis of Deff for our system reveals that mixing times are in the 100s of ms for our system. All of the work in this thesis employed a two spot interrogation design to probe the state of cells prior to mixing with analyte and again after mixing with the analyte. The long mixing time relative to our flow rates and length of the mixing channel (100 – 300 μm) is a desirable feature to prevent premature sensor response.

Approximate mixing time calculations for the most utilized microfluidic design in this work are presented in Chapter 3.

Characterizing mixing time after droplet formation becomes much more complicated as droplet convection begins due to contact with the walls of the channel. Extensive numerical calculations have been done to characterize droplet convection in context of droplet microfluidics and the resulting mixing effects.[76] Mixing within droplets is enhanced further when a moving droplet encounters a turn in the channel, resulting in a 'folding' effect. Given the variability of the cell position (also affected by convection) within the droplet, it is assumed the cell is exposed to saturating analyte-ionophore concentrations soon after droplet encapsulation. The Y-mixing junction used in these devices and an example of the position of the cells relative to the reagent stream is shown in Figure 2.2.

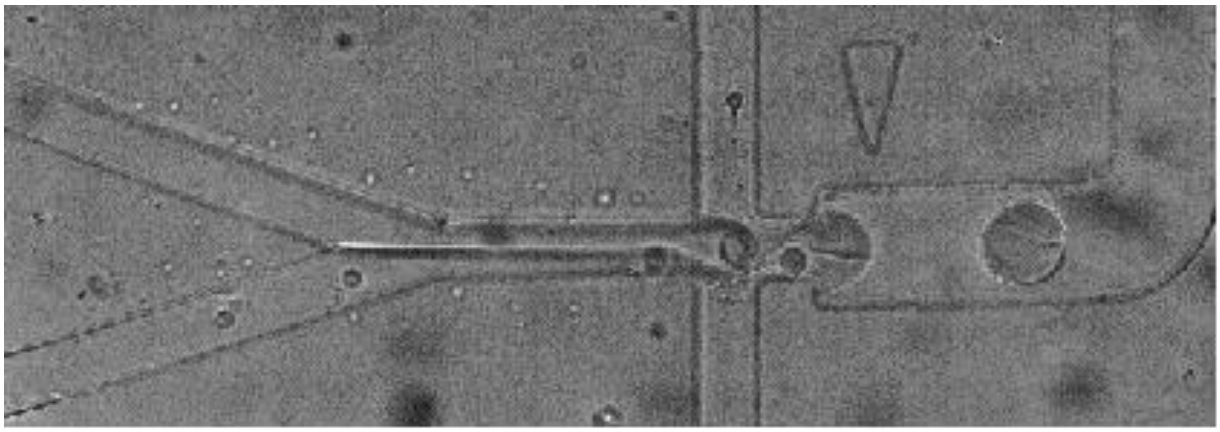
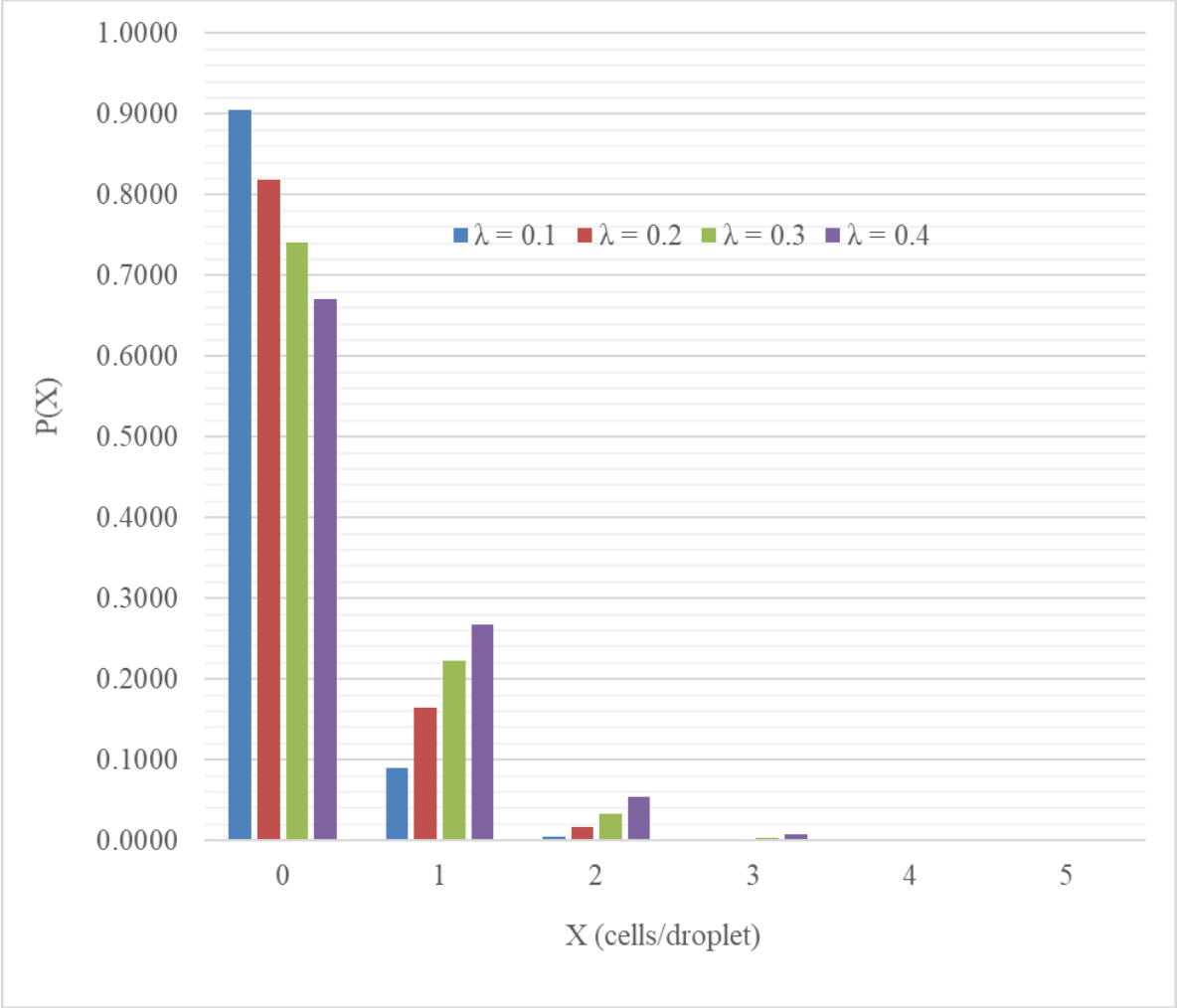


Figure 2.2. Y-shaped mixing junction used in the microfluidic devices presented in this thesis. The presence of OptiPrep in the cell buffer changes the refractive index of the media, leadingto a clear visual differentiation between the cell buffer and the added ligand buffer. The cell buffer (bottom channel of the Y) is distinguishable by the presence of cells in the channel.

2.2.4 Droplet Occupation

Single-cell interrogation and sorting hinges on the ability to isolate single-cells. In the context of droplet microfluidics, this means the accuracy of any experiment is limited by the capacity to generate droplets with only one cell. Droplet occupation follows a Poisson distribution according to $P(X) = \exp(-\lambda)(\lambda^X/X!)$ where X is the number of cells per droplet, P(X) is the probability, and λ is the average number of cells in the droplet volume. As shown in Figure 2.3, the probability of multiple cells in a droplet remains below 2% for values of λ between 0.1 – 0.2. This results in most of the droplets generated containing no cell at all, which is a necessary loss in throughput to keep the chance of multiple occupancy low. Strategies to increase the rate of single cell occupation have been discussed at length elsewhere [66], but add an additional layer of complexity to any device. Droplets with a volume of 150 pL correspond to an input cell (or fluorescent bead) concentration of ~$1x10^6$ cells/mL. It should be noted that while these concentrations work well for cells that naturally grow in single-cell suspension or with beads, cultured adherent cells that show a high degree of cell-cell adhesion and surface adhesion will complicate the arrival of single cells. Strategies to reduce cell aggregation will be discussed further in this chapter. An example of single HeLa cell encapsulation in our system is shown in Figure 2.3 (bottom). A detailed discussion of the interplay between droplet generation, droplet occupation and screening/sorting throughput is located in Chapter 3.



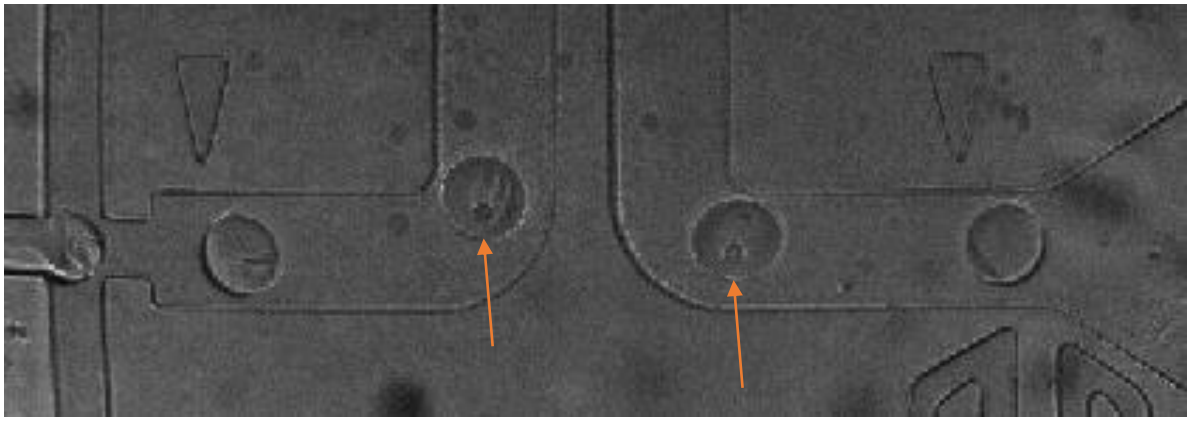


Figure 2.3. (Top) Poisson distribution derived probabilities of finding a cell in a droplet for values of λ relevant to this work. (Bottom) Example image of single cell encapsulation in droplets.

2.2.5 Droplet Sorting

The benefits of droplets extend beyond the ability to use them as discrete reaction vessels. A water-in-oil droplet configuration was chosen for the microfluidic assays in this thesis as it is simple to set up a sorting mechanism by coupling the droplet device to electrodes capable of dielectrophoresis (DEP). There are many methods for sorting cells including optical trapping, valve-based sorting, surface acoustic waves, and electro-osmosis.[77] Dielectrophoresis is an easily implemented sorting strategy based on the generation of an induced dipole in the droplet by an oscillating electric field gradient. The force applied to move a particle by dielectrophoresis is

$$F_{DEP} = 2\pi\varepsilon_m R^3 CM(\nabla E^2) \quad (2.3)$$

where ε_m is the absolute permittivity of the surrounding medium, R is the radius of the particle, CM is the Clausius-Mossotti factor (the real portion of a complex variable dependent on the polarizability of the particle at the applied frequency), and ∇E is the gradient of the rms amplitude of the electric field. The direction of the force is determined by the dielectric difference between the continuous phase and the dispersed phase. It is immediately apparent why droplet sorting is advantageous from Equation 2.3 based on the low permittivity of the fluorinated oil phase and the large size of the droplets relative to the cells. This enables lower voltages to be used in the sorting process to greatly reduce the risk of electric field induced cell death. The sharp natured shape of the electrodes used in the device is designed to increase the term ∇E^2. Sorting actuation occurs when F_{DEP} exceeds the Stokes' drag force which is proportional to the size and velocity of the particle, as well as the viscosity of the surrounding media. Experimentally, this is determined by modulating the applied voltage until droplets begin to move toward the sorted channel, typically on the order of 0.2-0.5 kV for these flow conditions. The frequency of the applied field is based on literature precedent for droplets of a similar size

and set to 30 kHz square pulses. An example of a sorting event and the asymmetric, pointed electrodes is shown in Figure 2.4 (top).

The geometry of the sorting junction and the implementation of cell collection also plays a factor in the efficiency of sorting. For two-way sorting, the junction breaks off to a ‘waste’ channel and a ‘keep’ channel. The resistance of these channels is fixed so that the resistance of the keep channel is at least 1.5 times higher than the waste channel. Droplets will naturally flow toward the channel of least resistance, allowing passive disposal of undesirable cells. Problems occur for this portion of the device if the droplet spacing is small. The divergence of the interrogation channel into the sorting channels necessitates a region the is wider than the previous channel and therefore droplets slow down in this area (Figure 2.4, bottom left). This was modified in later iterations to reduce the size of this region (Figure 2.4, bottom right) This allows for two closely spaced droplets to collide or increase the local resistance of the waste channel, resulting in the latter droplet to improperly enter the keep channel. The presence of the islets between the keep and waste channels is designed to reduce the effect of one droplet modifying the resistance of a channel for subsequent droplets by permitting the free movement of the continuous phase.[78] The addition of microtubing to the device outlets can have a drastic effect on the ratio of the output resistances. The tubing rises vertically out of the device before curving down to the output reservoirs (which are kept at ambient pressure). This introduces a small gravity head that can be used advantageously by modifying the height of the microtubing if droplets are moving down the keep channel in the absence of an electric field.

An interesting effect of the electric field is shown in Figure 2.5. Droplets that have been exposed to the 200V, 30 kHz, 15 ms pulse as they passed the electrodes merge over after making

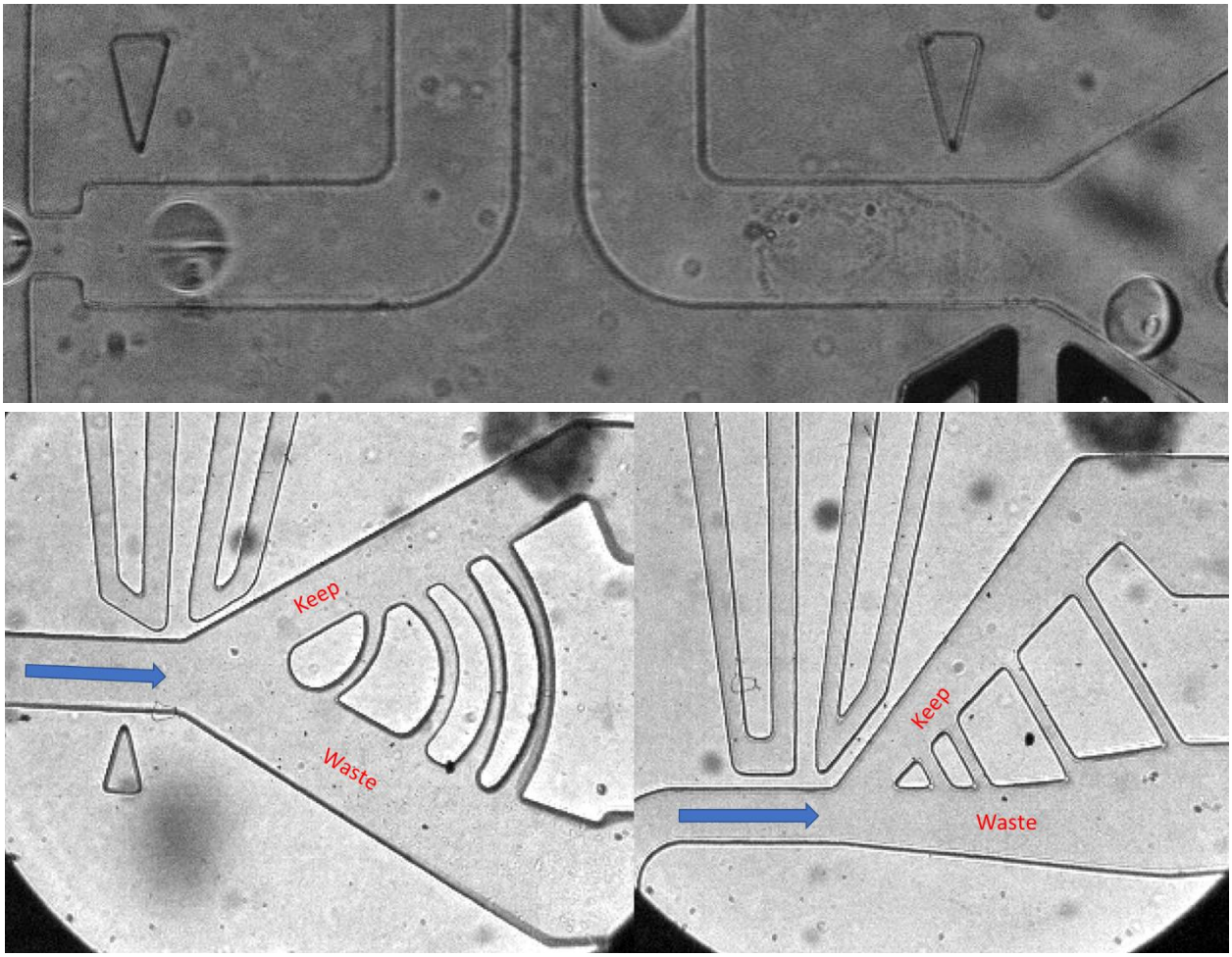


Figure 2.4: (Top) Example image of a sorting event of an encapsulated cell after determination of a gated FRET response. (Bottom) Evolution of the droplet sorting junction over the course of this thesis. Channel widths were decreased and rate of growth from delay channel to sorted channels was decreased to reduce droplet slowdown in the area resulting in droplet collision. Blue arrow indicates direction of flow.

contact in the slower output channel. This is due to an electric field mediated rearrangement of the surfactant molecules on the surface of the droplet with recovery times on the order of seconds. This effect has been taken advantage of for applications involving droplet merging as a means to introduce reagents to already formed droplets.[55,79] This effect could be useful for the current assay if sorted droplets were able to collect in close proximity. The current implementation, however, has sorting events that are too spaced and a continuous flow scheme that prevents droplet pooling until the outlet reservoir.

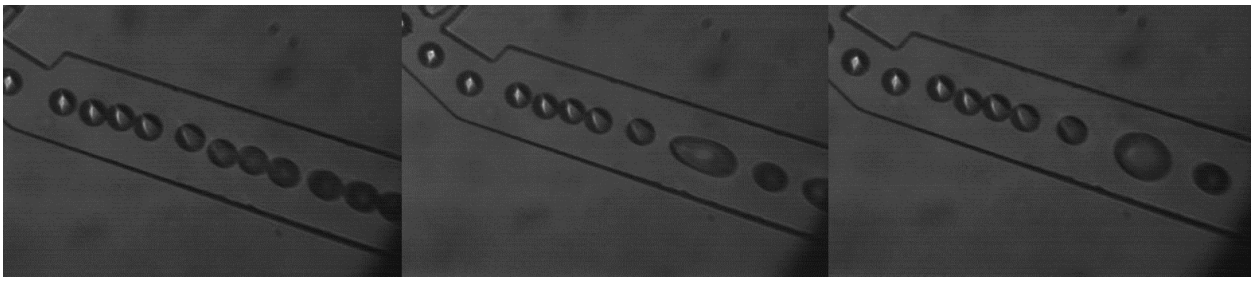


Figure 2.5: Three consecutive frames showing the merging of three droplets after exposure to the electric field present at the electrodes.

2.2.6 Microfluidic Fabrication

Microfluidic devices are prepared using standard soft lithographic techniques. SU8 3000 photoresist (MicroChem) is spin-coated onto a 3" silicon wafer and exposed to uniform UV illumination under an acetate mask printed with the inverted image of the device design (CAD/Art Services). The wafers are developed and hard-baked to complete the master, then exposed to (1H,1H,2H,2H-perfluorooctyl)trichlorosilane (TCS) for several hours under vacuum. Poly-dimethyl-siloxane (PDMS) pre-polymer and bonding agent (Sylgard 184, Dow Corning) are mixed in a 10:1 weight ratio and poured onto the master to achieve 4 mm thickness. PDMS slabs and clean 40x22 mm No. 1.5 glass coverslips are O_2 plasma treated, then pressed together to achieve

an irreversible seal. Lastly the devices are treated with TCS in Novec 7500 (3M) to passivate the surface to the fluorinated continuous phase (Novec 7500), then blown out with air. The devices are then placed, one at a time, on a 150 ^{o}C hotplate and the electrode channels are filled with a low melting point In-Sn solder (Custom Thermoelectric). Small lengths of 1000V tolerant wire are inserted in contact with the solder and the assembly is sealed with epoxy to prevent liquids from entering the electrode inlets during the experiment. Devices are stable for months if stored in an opaque container at room temperature until use. A detailed protocol for the fabrication of PDMS microfluidic chips used in this work is provided in Appendix A.

2.3 Experimental Design

2.3.1 Optical Configuration

The optical layout is a standard inverted microscope utilizing epifluorescence capture. See Figure 2.6A for a picture of the setup. Excitation in two positions is provided by a 445 nm laser diode beam-shaped with a cylindrical lens to achieve a relatively flat beam profile across the width of the channel with a 1 μm focus and 1 kW/cm^2 irradiance in the interrogation region of the microfluidic channel. As discussed previously, this beam shape minimizes signal variations due to variation in cell position across the channel width.[80] In the reported system, this led to a 35-fold reduction in the signal variation when compared to circularly shaped beams.

Detector gains are adjusted to accommodate the diversity of cell brightness observed in these experiments such that droplet scatter/fluorescence is not observed, however it is evident that the background is constant from droplet to droplet by modifying the detector gain. Droplet scatter can be increased by increasing laser power or detector gain. This is useful when characterizing the system to identify droplet generation frequency.

The optical components are as follows, as they relate to Figure 2.6A: a) 50:50 beamsplitter, b) cylindrical lens, c) 445/20 nm bandpass, d) epifluorescence longpass filter, e) 580 nm camera longpass filter, f) 510 nm fluorescence dichroic filter, g) 483/32 nm CFP bandpass filter, h) 542/27 nm YFP bandpass filter, and i) 590 nm transmitted light longpass filter. Epifluorescence is collected with a 20X (0.75 N.A.) objective (Olympus) and passed through a series of dichroics to separate the emission from light used for excitation and visualization, ending with a dichroic to partition FRET donor (CFP) and acceptor (YFP) emission. The emission is split at the image plane by a pair of 1" broadband dielectric D-shaped mirrors. Emission is further selected by a bandpass filter on each PMT.

The incorporation of a second detector arm enabled a significant simplification of the algorithm necessary to do real-time pairmatching of cells between the two interrogation regions. The algorithm no longer needed to identify which spot the cell event belonged to, which was previously identified using the FWHM of the Gaussian-like signal. This split the image into two regions that then go on to a separate set of PMTs. The second detector also prevented the loss of cell events due to the simultaneous arrival of two cells at both Spot 1 and Spot 2. Figure 2.7 shows the overlap in two simultaneous cell events that would not have been resolvable in a 2 PMT setup. The presence of very bright events (large fluorescence signal), introduces the possibility of crosstalk between the spots. Minimization of the crosstalk can be achieved by sufficient separation of the beams (650 μm in the current iteration of the instrument) without approaching the edges of the field of view to avoid aberration at the edges of the objective.

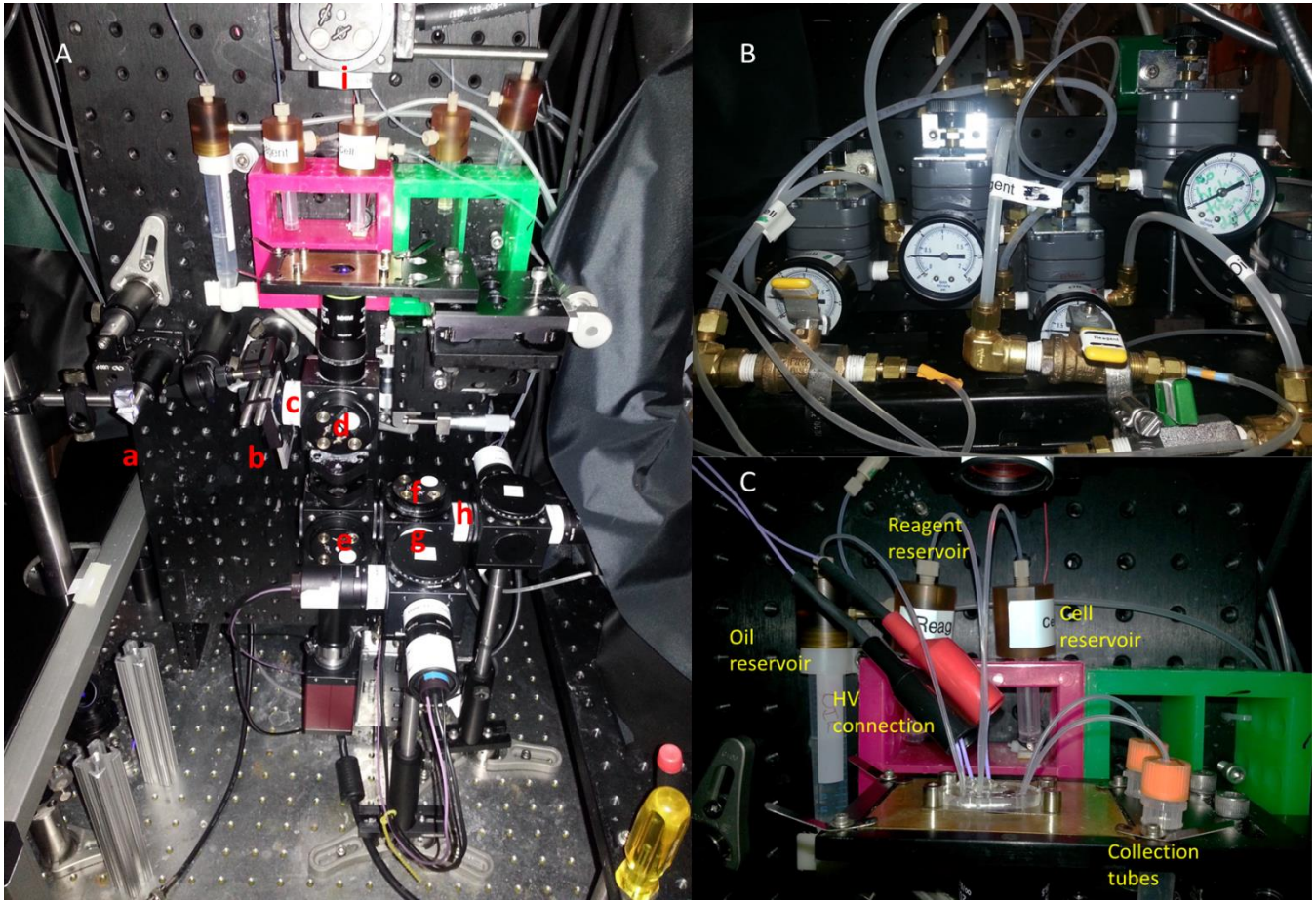


Figure 2.6: A.) Image of the epifluorescence microscope setup with labels as detailed in the text. B.) Image of the pressure controller setup used in this work for pressure driven flow. Pressure is down-regulated from building provided compressed air at 75 PSI. C.) Image of a fully connected microfluidic device as implemented during an experiment.

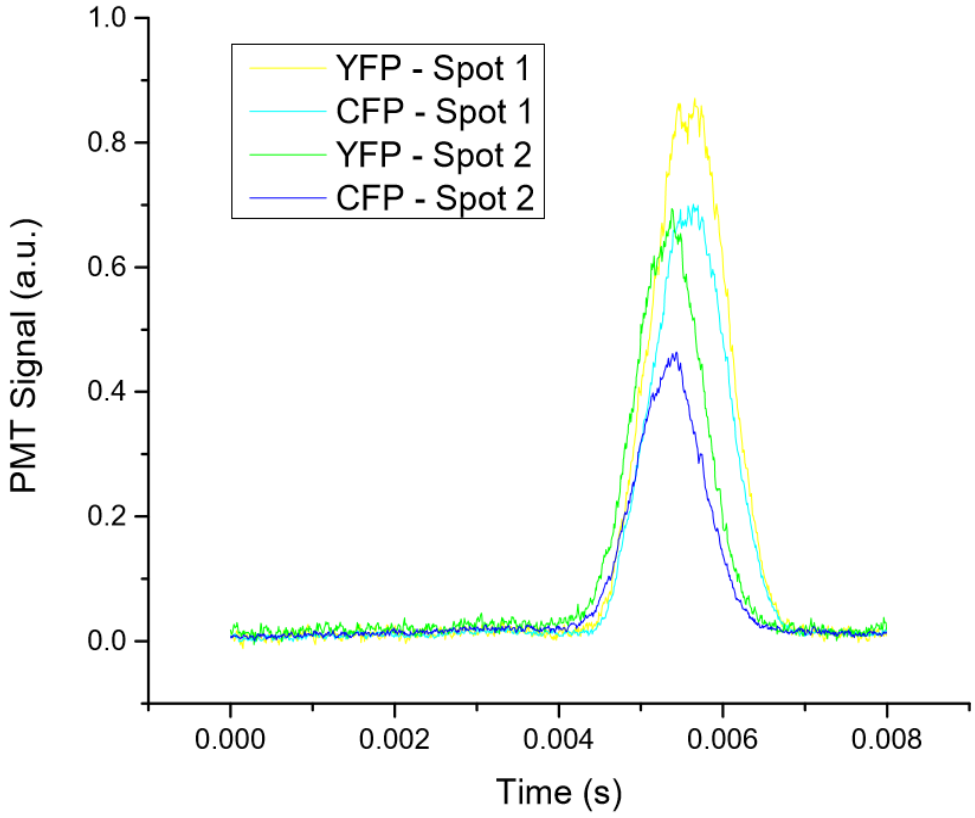


Figure 2.7: Raw data generated from ADC processed data from the photomultiplier tube. The graph shows two cell events that arrived simultaneously at interrogation beam 1 (yellow and cyan) and 2 (green and blue) that would not be distinguishable in a single detector arm

2.3.2 Pressure Driven Flow Configuration

Three 25 PSI pressure regulators (Figure 2.6B) are connected *via* microtubing to three off-chip reservoirs to maintain buffer/solution isolation prior to mixing on-chip. The three reservoirs consist of the cell suspension/microfluidic buffer, the metal-ionophore solution, and fluorinated phase. Microtubing from the reservoirs is inserted into the microfluidic device (Figure 2.6C). Microtubing is inserted into the outlets of the device after it has been started and an approximate time delay has been set. Inlets on the microfluidic device are punched smaller than the outer

diameter of the microtubing. This is sufficient to create an airtight seal at the pressures used, as long as the thickness of the PDMS slab is 4 mm or greater. The outlet tubing is inserted into collection vials maintained at ambient pressure.

2.3.3 Electronics

Signals from the two photomultiplier tubes (R9880U-20, Hamamatsu) are sampled at 50 kSamples/sec by an A/D converter on an LPC1769 microcontroller (Figure 2.8) in a home built circuit. Parameters such as signal threshold, FRET ratio thresholds for the two measurement points FRET 1 (YFP1/CFP1) and FRET 2 (YFP2/CFP2) and the FRET ratio change, R_2/R_1 or FRET 2/FRET 1, threshold, as well as timing parameters for the pair-matching and sorting signal are sent over a FSUSB connection to the microcontroller. Data are simultaneously collected by a National Instruments DAQ (NI 6251) board and processed by custom LabView software for calculations that are too CPU-intensive for the microcontroller. For example, compiling the signal timing histograms for determining delay times between interrogation regions requires operations on large arrays. Encapsulated cells with signals satisfying the gate conditions are sorted using dielectrophoresis. Sorting is triggered by a TTL signal from the microcontroller for the duration of the desired sorting time to a function generator (Keysight Technologies) which sends a square wave pulse to a high voltage amplifier (TREK) connected to the electrodes (visible in Figure 2.6C) on the microfluidic device. The code driving the microcontroller, including the pairmatching algorithm, is located in Appendix B.

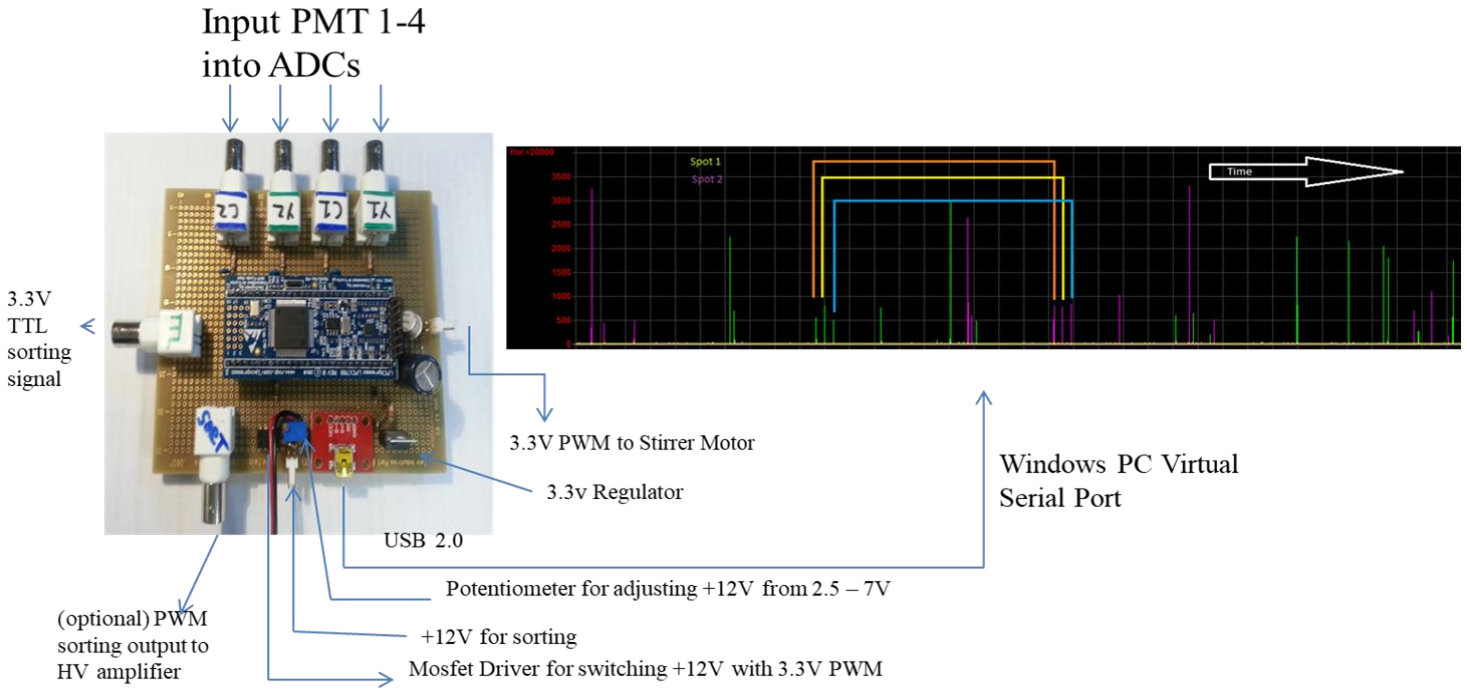


Figure 2.8: Microcontroller setup used in this work. Inset graph is streaming data with colored bars indicating 3 peaks which would be matched in the pairmatching algorithm due to the constant time spacing between them. Green peaks refer to spot 1 signal, while purple peaks refer to spot 2 signal.

2.3.4 Sample Preparation and Instrument Operation

The success of any screening or sorting experiment is highly dependent on the preparation steps leading up to the cytometry portion. Determination of the proper cell concentration to prepare using the Poisson statistics previously mentioned becomes useless if the experiment does not begin with a single cell suspension. This section provides some details and reasoning for the preparation of the cells and the buffers used in the microfluidic experiment, as well as some procedural guidelines, which are pertinent to a successful screen on single cells.

Adherent mammalian cell lines such as HeLa, MIN-6, and HEK-293 grow with high cell-to-cell contact on cell culture plates that must be broken up prior to further preparation. In this thesis, HeLa and HeLa-S3 cell lines are used for all cytometry data presented. HeLa-S3 is a line derived from HeLa cells that was selected through several rounds of growth and was found to grow successfully in suspension.[81] The HeLa-S3 line has proven easier to create cluster-free single cell suspension than the parent HeLa line. However, the HeLa-S3 cell line suffers from a decrease in transfection efficiency when treated with the same chemical transfection conditions as HeLa cells. An example is shown in Figure 2.9, in which HeLa cells and HeLa-S3 cells are both treated with equal concentrations of Lipofectamine 3000 reagent components and 1 µg of two different CFP/YFP Zn^{2+} sensor plasmids (pcDNA3.1+ backbone for each) for transient transfection. The images are taken 48 hours after transfection with identical exposure settings using a GFP filter set. The decreased efficiency of gene introduction has also been verified for Transit-LT1 and adenovirus transfection. Stable line creation is possible for HeLa-S3 cells, but must be FACS enriched for high intensity prior to use. Harvesting either line of these cells by physical detachment (cell scraper) did not generate proper separation of cell clusters; instead, harvesting requires trypsinization to fully isolate the cells.

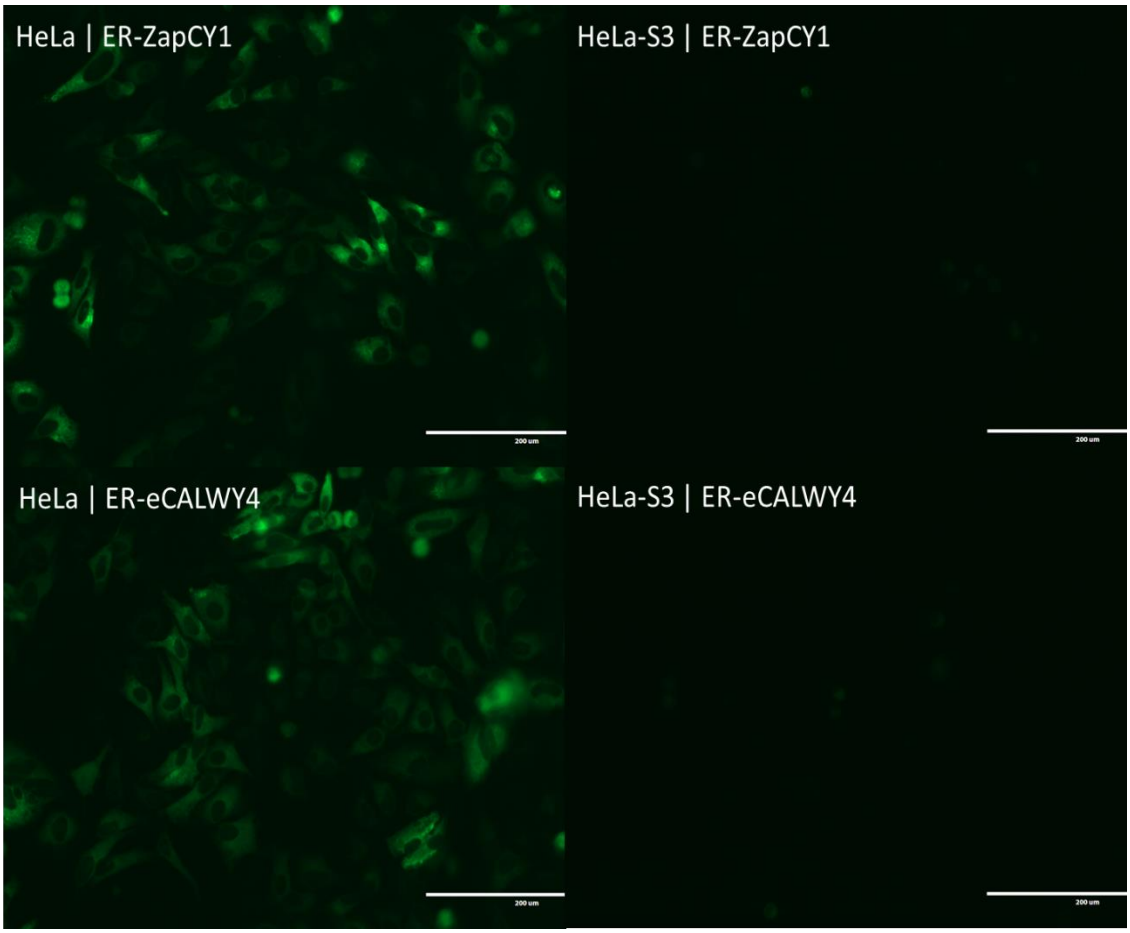


Figure 2.9. Microscope images of ER localized Zn^{2+} sensor expressing cells under identical transfection conditions. The left column shows HeLa cells, while the right column contains HeLa-S3 cells. Images are taken under identical illumination and exposure settings.

All steps prior to introduction of the cells into the microfluidic device should avoid exposure to high concentrations of divalent cations (Ca^{2+}, Mg^{2+}). The typical protocol for deactivating trypsin and suspending mammalian cells includes the addition of serum, however without treating the serum with chelator, the metals are immediately reintroduced. Cells will begin to aggregate in these conditions. The current protocol involves adding Ca^{2+} and Mg^{2+} free HEPES buffer Hank's Balanced Salt solution (HHBSS), pH 7.4, with added 0.1% bovine serum albumin (BSA) to the trypsinized cells. Otherwise, normal FACS protocol for the preparation of cells should be followed. This includes any precaution to avoid cell damage during preparation such as: avoid bubbles during pipetting, avoid aspirating the entire solution during buffer exchange, and use the fewest possible centrifugation steps as required by the assay.[44] Cells and solutions should be kept on ice at all times until the experiment. Cell passage number can also have a significant impact on the ability to isolate single cells. If no work-up of the cells is necessary after the microfluidic experiment, DNase I can be added to discourage cell aggregation. Lastly, all buffer solutions should be filtered through 0.2 μm filters and cell solutions through 40 μm filters.

The cell buffer contains two key components to ensure steady arrival of cell events in the microfluidic. The first is BSA added to 0.1-1% by weight to discourage the re-aggregation of the cells during incubation. Additionally, the BSA coats the PDMS and glass coverslip upon contact when the cells and reagent are introduced to the microfluidic device. The devices are initially coated with a fluorophilic compound to increase wettability of the fluorinated oil phase. The aqueous channels cannot be selectively treated with a BSA solution prior to device startup. The presence of BSA prevents cells from adhering to the walls of the device and encourages a steady stream of cell events. Figure 2.10 shows a problematic buildup of poorly separated cells at the

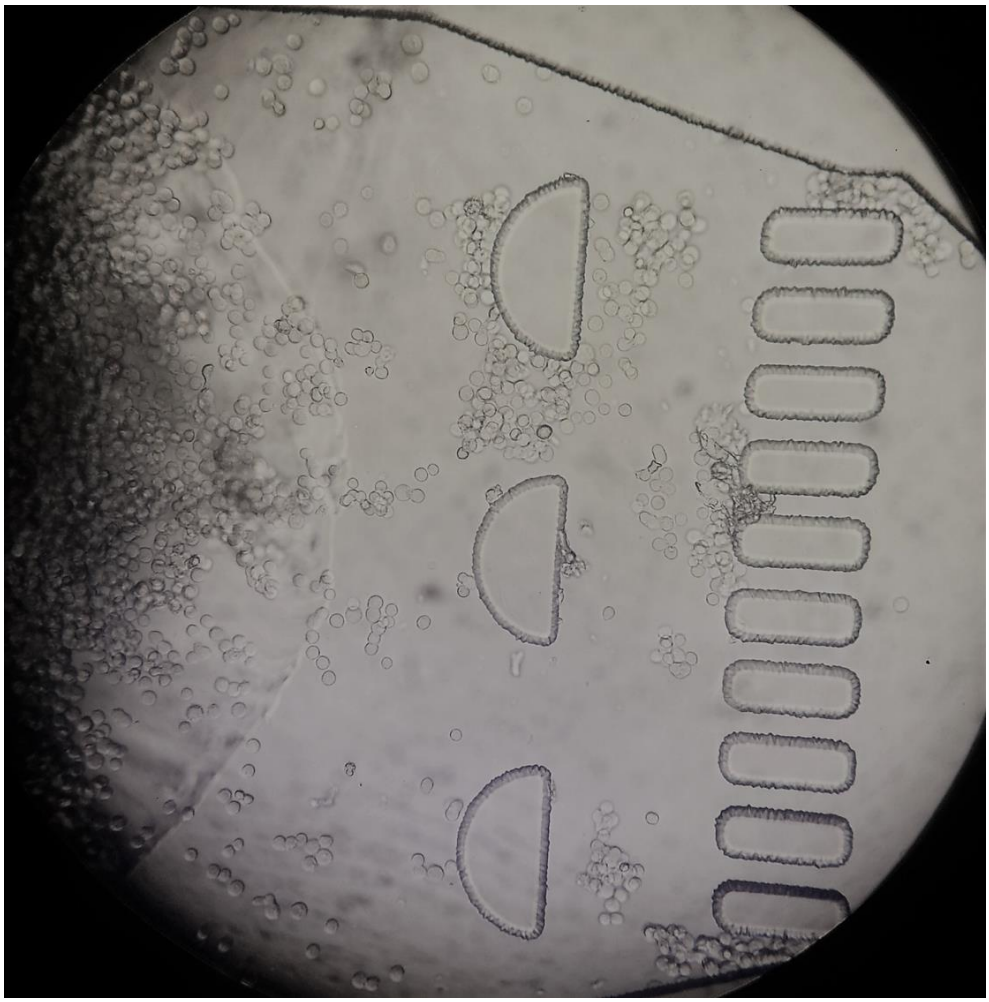


Figure 2.10: Image of the inlet of a microfluidic device in which cells were poorly isolated prior to introduction in the device and BSA was not used in the cell buffer.

inlet of the microfluidic device in the absence of BSA which led to very slow arrival of cells to the interrogation region of the device.

The second critical component in the cell buffer is a density matching reagent. Another problem encountered during long cytometry experiments is the sedimentation of cells due to the mismatch in density between cells and the surrounding media. One method for preventing cell sedimentation is to add a micro stir bar to the cell reservoir (or syringe for many microfluidic flow systems). However, this method potentially promotes cell death at the speeds required to maintain a homogeneous distribution of cells over long experiments (> 1 hr).[54] Additionally, the micro stir bar does not prevent cell sedimentation in the micro tubing. OptiPrep (AxisShield, 60% iodixanol) is a suitable reagent for this purpose. OptiPrep is added directly to the buffer in a percentage that adjusts the density to the density of the cells and prevents cell sedimentation over time. A simple experiment was conducted to determine the optimal concentration of OptiPrep for suspending HeLaS3 cells (it was not assumed that HeLa cells and HeLa-S3 cells have the same properties). Increasing concentrations of OptiPrep were added to separate vials of cells at a concentration of 1 million/mL in HHBSS (pH 7.4). Cells were collected from the top 1/3 of the solution and plated immediately for t = 0 hr. After 4 hours of unperturbed incubation, cells were again collected from the top 1/3 of the solution. As shown in Figure 2.11, at concentrations above 16%, cells were still present in the top portion of the solution, indicating they had not settled to the bottom due to density differences. The lowest concentration that contained cells, 16% v/v, was chosen as the working concentration for HeLa-S3 cells. The percentage indicates volume of OptiPrep, not iodixanol.

With regards to instrument operation, it is important to introduce each fluid into the microfluidic device in a specific order. The fluorinated oil (continuous phase) should be

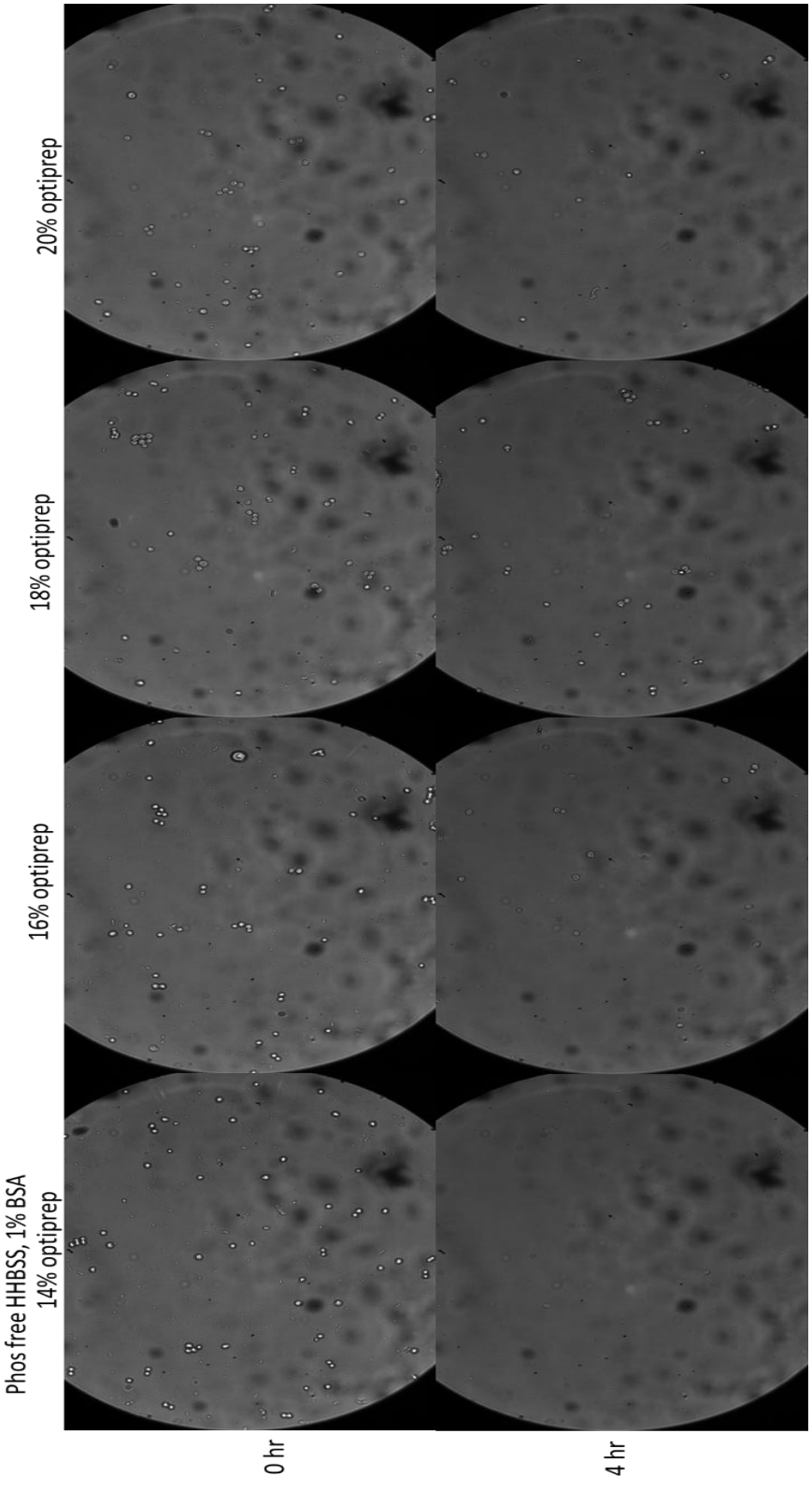


Figure 2.10: Experimental determination of the optimal concentration of Optiprep to keep cells suspended for several hours. Time increases down, while OptiPrep concentration increases to the right. Optiprep concentration is in unites of % v/v.

introduced first and allowed to fill the delay channel prior to turn on the aqueous buffers (dispersed phase). This prevents the aqueous phase interfering with the fluorophilic coating in the channels and prevents wetting of the aqueous phase to the coverslip. Next, both aqueous phases should be introduced simultaneously in order to avoid either channel from backing up into the other at the Y-mixing junction. If reagent is allowed to back up into the cell channel, cells may begin an early response to the high levels of Zn^{2+}/pyrithione, altering the FRET 1 value. Additionally, the system should be started at higher speeds (pressures > 7 PSI per channel) than may be used in the experiment. The pressures can be decreased to operating pressures after this. Stopped or very slow flow can cause cell buildup in the inlet which will need to be cleared with high pressure prior to the start of the experiment. See Appendix A for a detailed protocol for microfluidic operation.

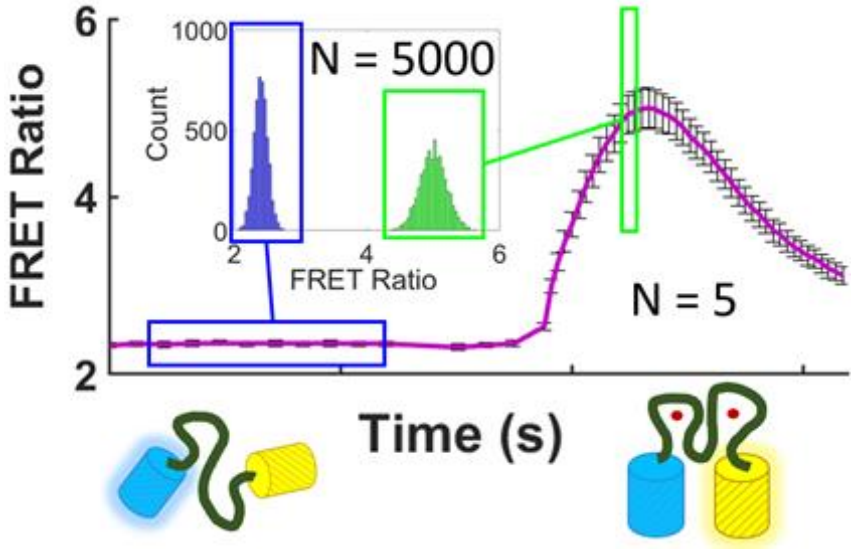
2.3.5 Cell viability

Cell viability in this system has been an ongoing problem that is coupled to the microscopy experiments discussed in Chapter 3 and 4. The introduction of Zn^{2+} and pyrithione (a membrane permeable Zn^{2+} ionophore) results in a complete lack of cell viability for the exposed cells. Cell viability was explored multiple times across multiple experiments in which cells were recovered from droplets and plated in DMEM (30% fetal bovine serum) after exposure to Zn^{2+}/pyrithione on the microfluidic device, both in the presence and absence of the electric sorting field. The resulting cells remained non-adherent and morphologically necrotic after 24 hours in cell culture conditions (37 ^{o}C, 5% CO_2) with no washing. Additional experiments which excluded Zn^{2+}/pyrithione resulted in ~90% adherent vs. non-adherent cells after 24 hours (as a crude measure of viability without added stain) in the absence of an electric field and ~73% in

the presence of a 300V, 30kHz field as they passed the electrodes. The implications of the 100% cell death rate are discussed in Chapter 3 and strategies to work around it in Chapter 4.

Chapter 3

Droplet Microfluidic Flow Cytometer for Sorting on Transient Cellular Responses of Genetically-Encoded Sensors



3.1 Publication Note

This chapter was adapted from Fiedler, B. L. *et al.* Droplet Microfluidic Flow Cytometer for Sorting On Transient Cellular Responses of Genetically-Encoded Sensors. *Anal. Chem.* **89,** 711–719 (2017) and the corresponding Supplementary Information. Figures present in the publication are unmodified in this chapter.

3.2 Motivation

Fluorescent biosensors are important measurement tools for *in vivo* quantification of pH, concentrations of metal ions and other analytes, and physical parameters such as membrane potential. Both the development of these sensors and their implementation in examining cellular heterogeneity requires technology for measuring and sorting cells based on the fluorescence levels before and after chemical or physical perturbations. We developed a droplet microfluidic platform for the screening and separation of cell populations on the basis of the *in vivo* response of expressed fluorescence-based biosensors after addition of an exogenous analyte. We demonstrate the capability to resolve the responses of two genetically-encoded Zn^{2+} sensors at a range of time points spanning several seconds and subsequently sort a mixed-cell population of varying ratios with high accuracy.

Specifically, we describe a droplet microfluidic system that introduces each cell expressing a FRET sensor to the appropriate analyte, probes the baseline FRET level and the sensor response at multi-second time delays set by the geometry of the fluidic network and driving pressures, and then sorts on the basis of the response with dielectrophoresis (DEP). This work represents a significant advance over a previous study conducted by the Jimenez group of cytosolic and extracellular-membrane-expressed D3cpV and D3pdD Ca^{2+} and ZapCY1 Zn^{2+} sensor response in HeLa-S3 cells.[82] This previous study established that cellular response occurred on the ms-sec timescale in a two-dimensional hydrodynamic flow-focusing geometry. The response of cytosolic sensors was ~30 fold slower than the response of sensors expressed on the cell surface, and the response appeared to be limited by cation transport across the plasma membrane. Our previous study also revealed heterogeneity in the ZapCY1 Zn^{2+} sensor response. The sensor response heterogeneity was attributed to viral recombination during stable

transfection of mammalian cells with the sensor resulting in response and unresponsive sensor populations. A major limitation of the instrument employed in the previous study was that signal post-processing was required to determine the single-cell response. Here, we demonstrate real-time signal processing and sorting with a microcontroller-based system, and clear measurement resolution and sorting based on the responses of two closely-related Zn^{2+} sensors. This new instrument provides a platform for directed evolution of new cellular sensors. Although we specifically optimized the system for screening genetically encoded Zn^{2+} FRET sensors, the technology is directly applicable to many other sensors.

3.3 Experimental Setup

3.3.1 Sensor Constructs

Two genetically-encoded Zn^{2+} sensors, ZapCV2 and ZapCV5, were chosen for study due to their structural similarity, yet differing dynamic ranges as would be expected for a library of these sensors. These sensors are comprised of a fluorescent protein FRET pair including a 11-residue truncated enhanced Cyan Fluorescent Protein (CFP) as the donor and circularly permuted Venus (cp173) as the acceptor. The FRET pair is connected by a Zn^{2+} binding domain (ZBD) consisting of the first two Zn-fingers in the Zap1 transcription factor adopted from *S. cerevisiae*. These sensors only differ by two mutations. The native Zn-finger contains two Cys and two His as coordinating ligands. In ZapCV2, one of these Cys residues is mutated to His in both fingers. In ZapCV5 all four Cys residues are mutated to His. Both constructs contain N-terminal nuclear exclusion sequences (NES) to achieve cytosolic localization. The FRET response is defined as the ratio of the acceptor to donor fluorescence intensities upon donor excitation, $R = I_{FRET}/I_{CFP}$. Upon Zn^{2+} binding, the donor-acceptor pair undergoes a conformational change and the value of

R increases.[40,41,83] The *in vitro* K_D values (Hill coefficient, n) of the sensors are 2.3 nM (n = 0.53) and 0.3 µM (n = 0.55) in buffer (150 mM HEPES, 100 mM NaCl, 10% glycerol, pH 7.4) and the dynamic ranges (defined as the ratio R_{max}/R_{min}) are 2.1 and 1.5 for ZapCV2 and ZapCV5 respectively. A schematic of the Zn^{2+} sensors with sequence differences highlighted and the data used to obtain *in vitro* binding affinities can be found in Figure 3.1.

3.3.2 Design of ZapCV2 and ZapCV5 Zn^{2+} sensors

ZapCV sensors are modified based on previously characterized ZapCY2 sensors.[41] The FRET acceptor (citrine fluorescent protein, YFP) in ZapCY2 was replaced by circularly permuted (at amino acid 173 position) Venus fluorescent protein, which generated ZapCV2 (YFP changed to Venus). The lower affinity ZapCV5 was created by quick change mutagenesis of the Zn^{2+} binding domain (C586H and C623H). The cytosolic NES-ZapCV sensors include an N-terminal nuclear export signal (MLQLPPLERLTL). These sensors were cloned in the pcDNA3.1 and PiggyBac Transposon vector backbone for mammalian cell expression and in the pBAD vector backbone for bacterial expression.

3.3.3 In vitro characterization of ZapCV2 and ZapCV5

For *in vitro* studies, the sensors were cloned into pBAD and expressed in Top-10 Escherichia coli with the addition of 0.2% arabinose. Sensor proteins were purified using Ni^{2+} ion affinity chromatography and the His tag was removed with TEV protease in 20mM Tris, 100 mM NaCl, pH8 buffer at room temperature overnight (sensor to TEV protease ratio was 10:1). The sensor was then concentrated with an Amicon centrifugal filter to 50-100 µM as determined by the absorbance at 516 nm using $\varepsilon = 77000\ M^{-1}\ cm^{-1}$.

Purified sensor was titrated with Zn^{2+} to determine the disassociation constants of Zn^{2+} from the sensors. Zn^{2+} titrations were performed in HEPES buffer (150 mM Hepes, 100 mM NaCl, and 10% glycerol, pH 7.4) with 1 µM sensor protein, treated for 5 minutes immediately prior to titration with 0.5 mM TCEP, and different concentration of free Zn^{2+} as described previously.[41] The in vitro fluorescence measurements used for Zn^{2+} titrations were made on a Tecan Safire-II fluorescence plate reader using the following parameters: excitation: 420 nm, emission: 435-649 nm, and the emission bandwidth was 10 nm. The apparent dissociation constant was determined using the fitting method described by Pomorski et al.[84] The intensities of the fluorescence emission at 481 nm were used as λ_1 and at 529 nm for λ_2. The ratios of these intensities were plotted against the zinc concentration and fitted using one of the following equations depending on the ratio used (λ_1/λ_2 vs. λ_2/λ_1).

$$R_{\frac{2}{1}} = \frac{(I_{2b}\cdot Z^n)+(I_{2u}\cdot {K_d}^n)}{(I_{1b}\cdot Z^n)+(I_{1u}\cdot {K_d}^n)} \qquad (3.1)$$

$$R_{\frac{1}{2}} = \frac{(I_{1b}\cdot Z^n)+(I_{1u}\cdot {K_d}^n)}{(I_{2b}\cdot Z^n)+(I_{2u}\cdot {K_d}^n)} \qquad (3.2)$$

Where the $I_{2b,}$ $I_{2u,}$ $I_{1b,}$ I_{1u} are fixed using the average intensity at λ_1 or λ_2 at the five most or least concentrated Zn^{2+} conditions, Z is equal to the –log of the free zinc concentration, K_d is the disassociation constant, and n is the hill coefficient. The reported K_d's are the average of 2 or more titrations of the sensor.

3.3.4 Cellular imaging for in vivo calibration

Imaging experiments were performed on a Nikon Ti-E wide-field fluorescence microscope equipped with Nikon elements software, Ti-E perfect focus system, an iXon3 EMCCD camera (Andor), mercury arc lamp, and YFP FRET (434/16 excitation, 458 dichroic, 535/20 emission), CFP (434/16 excitation, 458 dichroic, 470/24 emission), and YFP (495/10 excitation, 515 dichroic, 535/20 emission) filter sets. External excitation and emission filter wheels were controlled by a Lambda 10-3 filter changer (Sutter Instruments), while dichroic mirrors were placed on cubes in the dichroic turret. Images were collected using a 60X oil objective (NA 1.40), 100 ms exposure time, EM gain 1 MHz at 16-bit readout mode with an EM gain multiplier of 100, and a neutral density filter with 12.5% light transmission.

For the calibration experiments shown in Figure 3.5, sensor constructs were transfected into HeLa cells with TransIT-LT1 (Mirus Bio). Cells were imaged 48 hours post-transfection. Cells were maintained at 37°C and 5% CO_2 in a LiveCell™ environment chamber (Pathology Devices) during the experiment. Cells were imaged in phosphate-free HEPES-buffered HBSS, pH = 7.4 to prevent zinc precipitation. Resting images were collected for 5 minutes, followed by treatment with 150 µM TPEN to collect R_{min} data until a stable signal was achieved. Cells were then washed with phosphate, calcium, and magnesium-free HEPES-buffered HBSS, pH = 7.4, then cells were treated with 1 µM pyrithione and 50 µM $ZnCl_2$ to obtain R_{max} data. Resting and R_{min} images were collected every 1 minute, and R_{max} images were collected every 20 seconds. All data were analyzed in MATLAB (Mathworks). Images were background corrected by

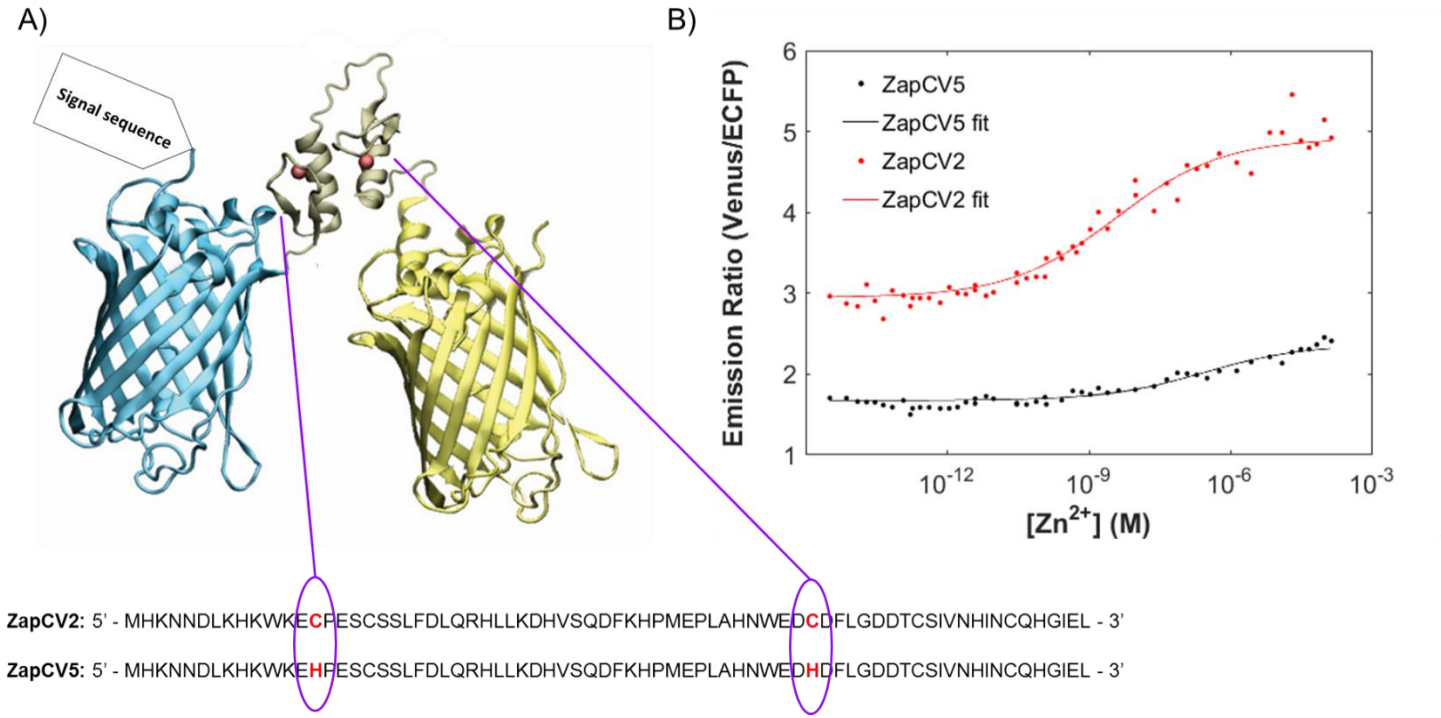


Figure 3.1: A) A cartoon of a representative FRET-based Zn^{2+} sensor used in this work. The structure from N-terminus to C-terminus consists of a localization signal sequence, ECFP (blue), Zap1 Zn^{2+} binding domain (green), Venus (yellow). Zn^{2+} ions are shown as red spheres. Sequences of the Zn^{2+} binding domains of ZapCV2 and ZapCV5 are shown below with the differing residues bolded and highlighted in red. B) In vitro titration curves showing the binding affinities and Hill coefficients for ZapCV2 and ZapCV5. Experimental details shown below.

drawing a region of interest (ROI) in a blank area of image and subtracting the average fluorescence intensity of the background ROI from the average intensity of each cell. FRET ratios for each cell were calculated by dividing the background-corrected YFP FRET intensity by the background-corrected CFP intensity ($(I_{cellular\ FRET} - I_{background\ FRET})/(I_{cellular\ CFP} - I_{background\ CFP})$). This background subtraction and FRET response measurement is done in image post-processing, though it should, in theory, be possible to speed up the process of dynamic range determination by incorporating a real-time algorithm in the acquisition software.

3.3.5 Sample Preparation

HeLa-S3 cells stably transfected by the PiggyBAC transposon system (SBI) with the desired genetically encoded Zn^{2+} sensor, NES-ZapCV2 co-transfected with mCherry-NLS or NES-ZapCV5, are grown in DMEM (Gibco) supplemented with 10% fetal bovine serum and 1% penicillin/streptomycin. They are harvested using 0.05% trypsin-EDTA in DMEM and resuspended in Ca^{2+}, Mg^{2+}, PO_4^{2-}-free HEPES-buffered Hanks Balanced Salt Solution (HHBSS) prepared with chelex treated water. Cells are pre-treated with 50 µM N,N,N',N'-tetrakis(2-pyridylmethyl)ethane-1,2-diamine (Sigma Aldrich), TPEN, for 10 minutes to generate the apo-form of the sensor prior to the experiment. Cells are washed twice with HHBSS, before being resuspended in a microfluidic HHBSS solution with 0.5 µM TPEN and 16% v/v OptiPrep (Sigma Aldrich) to prevent cell sedimentation during the course of the experiment. A solution of 50 µM $ZnCl_2$ and 25 µM pyrithione (2-Mercaptopyridine *N*-oxide, Sigma Aldrich) in HHBSS for the reagent reservoir is prepared fresh at the same time. The fluorinated oil phase for droplet generation is Novec 7500 (3M) mixed with 10% BioRad droplet generator oil (which contains a surfactant to stabilize the droplet generation and prevent droplet merging). After sorting, 100-400

μL of phenol-free growth media is added to the droplets, along with a volume of 2,2,3,3,4,4,4-Heptafluoro-1-butanol (Sigma Aldrich) equal to 1% of the oil phase. After < 5 minutes of incubation, the emulsion is centrifuged at 50*g* for 1 min to break the droplet emulsion and extract cells into the aqueous phase, which is then collected for analysis.

3.3.6 Microfluidic Design and Experiment Parameters

A PDMS microfluidic device was designed to initiate the cell reaction with exogenous Zn^{2+}, monitor the time-resolved response, and subsequently sort on the single cell response. HeLa cells pre-treated with TPEN to chelate free Zn^{2+} and desaturate the sensors enter the PDMS chip parallel to the input of a buffer containing a pre-defined concentration of $ZnCl_2$ and pyrithione, a cell membrane permeable Zn^{2+} ionophore. As detailed in Figure 3.2B&C, the two channels meet at a Y-junction where mixing begins, followed by a flow focus junction droplet generator to create water-in-fluorinated-oil droplets stabilized by a fluorinated surfactant. Encapsulated cells pass an initial laser excitation spot to measure the unbound FRET state, R_1 and flow along a delay channel outside the field of view. Cells return to the field of view at a later time defined by the channel geometry and input pressures, pass through a second interrogation spot to measure a bound FRET state, R_2, with the time between the interrogation spots defining Δt.

Three 25 PSI pressure regulators are connected *via* microtubing to three off-chip reservoirs to maintain buffer/solution isolation prior to mixing on-chip. The three reservoirs consist of the cell suspension/microfluidic buffer, the metal-ionophore solution, and fluorinated phase. Microtubing from the reservoirs is inserted into the microfluidic device. The implementation and pressure control is fully described in Chapter 2 (section 3.2).

Channels have a uniform height of 50 μm and widths vary from 50 μm in the input channels, to 100 μm in the middle section, and 200 μm in the outlets. The input channels use fluidic resistors to compensate for the output resistance of the chip. Resistance of the "keep" or sorted channel is 1.5 times higher than that of the "waste" channel to bias droplet flow away from the sorted channel. The sorting junction features several small islets to prevent resistance changes when a droplet occupies an outlet channel.[78]

The optical scheme (detailed in Figure 3.2A) is described in full in Chapter 2 (section 3.1). Briefly, the optical layout is a standard inverted microscope utilizing epifluorescence capture. Excitation in two positions is provided by a 445 nm laser diode beam-shaped with a cylindrical lens to achieve a relatively flat beam profile across the width of the channel with a 1 μm focus and 1 kW/cm^2 irradiance in the interrogation region of the microfluidic channel. Epifluorescence is collected through a train of dichroic and bandpass filters to a set of PMT detectors. The image is split in two at the focal plane, segregating signals from either interrogation spot.

3.4 Calibration experiments for FRET sensors

The microfluidic system is designed to measure the sensor parameters which are conventionally obtained from low-throughput fluorescence microscopy. In a typical microscopy measurement (Figure 3.5) a resting FRET ratio, R, is observed and subsequently a cell permeable Zn^{2+} chelator (N,N,N',N'-tetrakis(2-pyridylmethyl)ethane-1,2-diamine: TPEN) is added to desaturate the sensor and obtain an R_{min}. The cell is then treated with an agent to permeabilize the plasma membrane or an ionophore, such as pyrithione, and $ZnCl_2$ to saturate the sensor and establish an R_{max}. After the full saturation of the sensor has been achieved, the R_{max} signal in

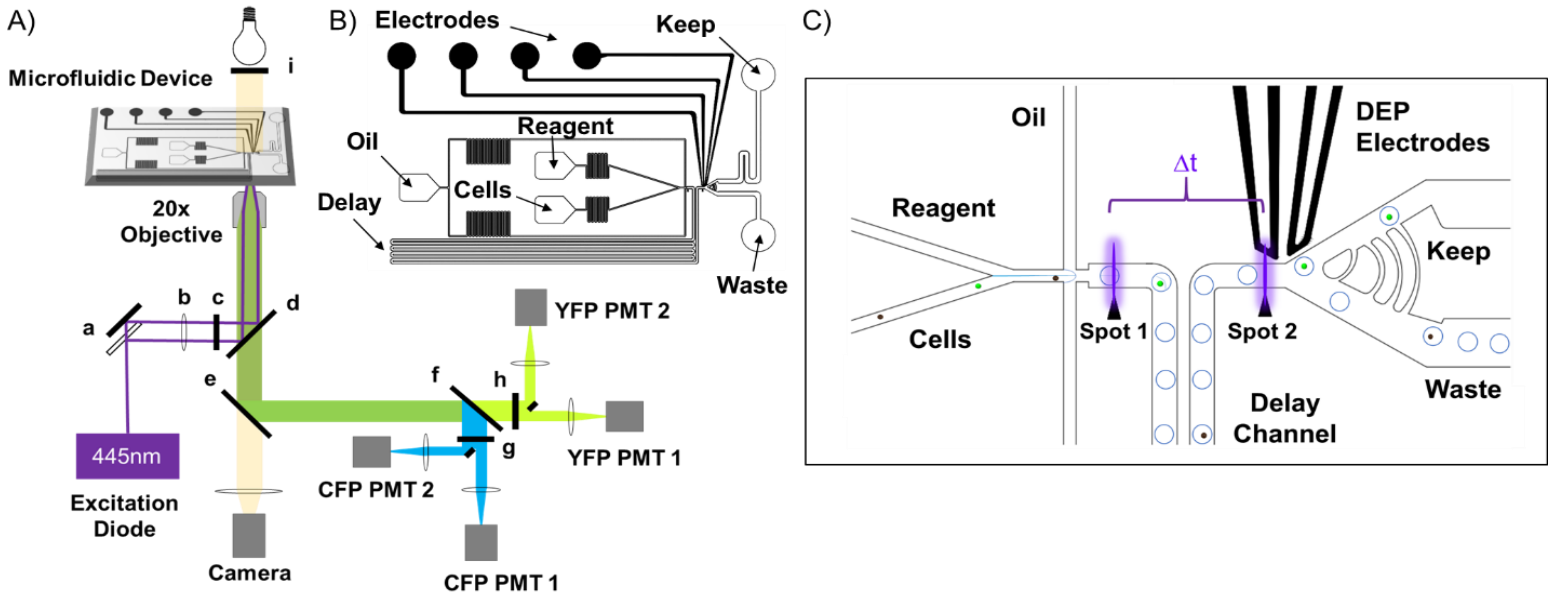


Figure 3.2. A) Epifluorescence microscope optical layout consisting of a) 50:50 beamsplitter, b) cylindrical lens, c) laser clean-up bandpass filter, d) epifluorescence longpass filter, e) camera longpass filter, f) fluorescence dichroic filter, g) CFP bandpass filter, h) YFP bandpass filter, and i) transmitted light longpass filter. B) Microfluidic device design used in this study. C) Close-up of analysis and sorting region of the microfluidic device. Optical details are provided in Chapter 2.

mammalian cells often diminishes by a currently unknown mechanism. The decay of the response may be due to cell death or homeostatic regulation of the Zn^{2+} levels. The transient nature of these signals define the requirements for the time-resolution of the cytometer.

Figure 3.4 provides a schematic that connects the calibration experiments to the schematic of the microfluidic assay as well as some of the data obtainable. Spot 1, the first interrogation beam (prior to complete mixing) measure the desaturated FRET signal, Rmin. This results in the black histogram (left-most) in Fig. 3.4C. At a time after Zn^{2+}/ionophore addition, defined by the delay (Δt) in the device, the cells are probed again at spot 2 which corresponds to

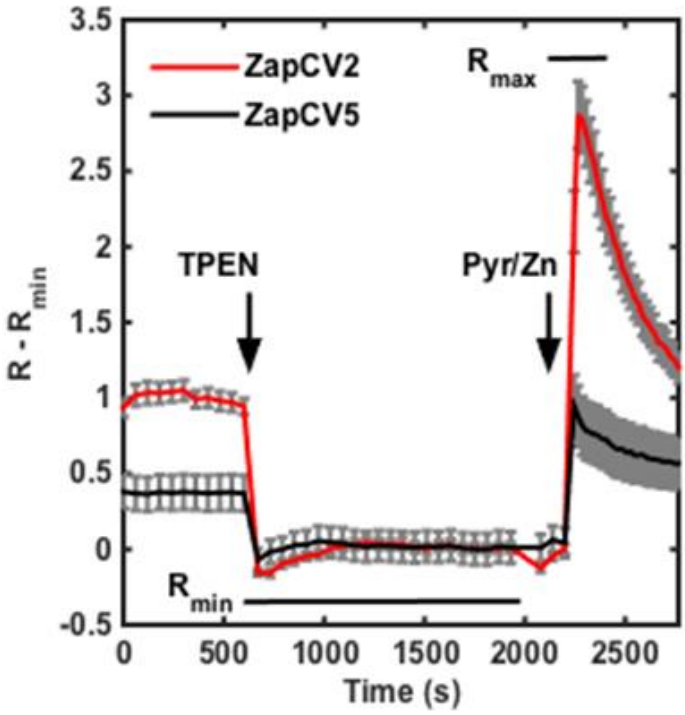


Figure 3.3. Representative calibration plots of ZapCV2 (red, n = 4 cells) and ZapCV5 (black, n = 9 cells). TPEN (150 μM) and Pyr/Zn (1 μM pyrithione and 50 μM $ZnCl_2$) were added at the indicated times. Data are displayed as R – R_{min} for each sensor, where R is the FRET ratio at each time point and R_{min} is the minimum FRET ratio obtained after incubation with TPEN. Error bars are the standard error of the mean. Regions used to determine R_{min} and R_{max} are denoted with bars at the appropriate locations.

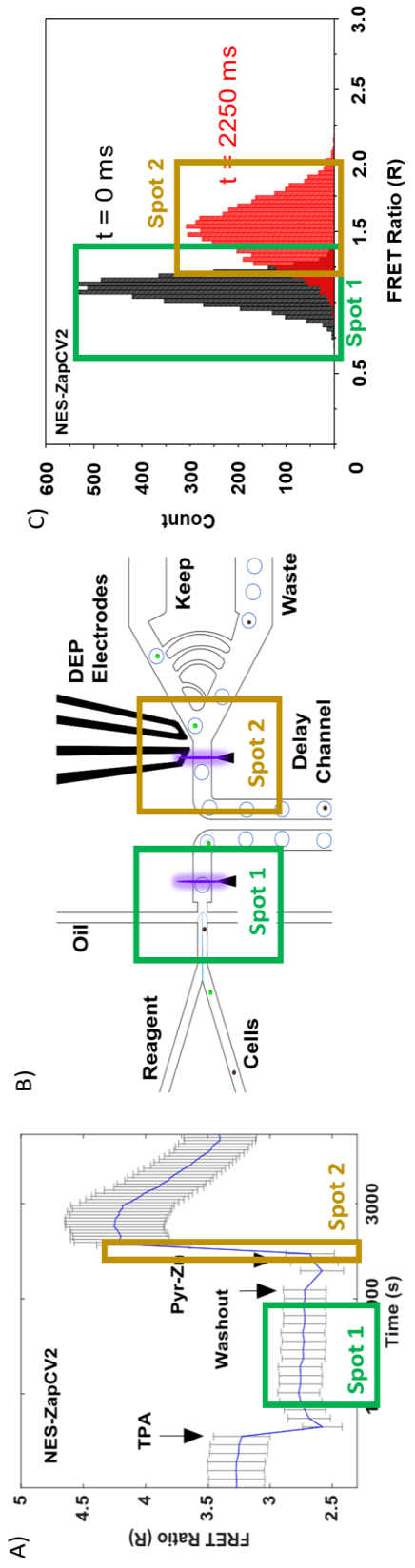


Figure 3.4. Schematic indicating the connection between the A) traditional microscope calibration experiments, B) microfluidic assay, and C) data obtained by the cytometer. Spot 1 corresponds to Rmin in this setting, while Spot 2 corresponds to the sensor FRET value at some time delay after Zn^{2+} addition.

a point in the rise of the sensor response shown in Fig. 3.4A and the right-most (red) histogram in Fig. 3.4C. This window can be modulated by adjusting the pressures and delay channel geometry to encompass early time or saturation for cytosolic sensors.

3.5 Tracking cells through pair-matching

Sorting requires real-time analysis of cellular response based on the fluorescence signals from spatially and temporally separated points in the flow channel. We previously reported a simple post-processing algorithm with a sliding time window and linear velocity distribution for matching the response of each cell at two time-points (*i.e.* "pair-matching") using a single pair of donor/acceptor PMTs The successful time-demultiplexing of signals into matched pairs from individual cells in a single PMT-pair arrangement is limited by the number of cells, n_{crowd}, that occupy the delay channel. The previous system suffers a loss in pair-matching accuracy for $n_{crowd} > 5$.[82]. Here, we implemented new signal collection and signal processing to enable real-time flow analysis and sorting. We spatially separated the signals from the two interrogation points, each of which is then directed into a pair of PMTs. This separation permits the sensor response from each cell to be tracked by a simple time window based pair-matching algorithm implemented on a microcontroller. Additionally, spatially segregated signals eliminate the problem of simultaneous cell arrival events at each interrogation region. This scheme would also generally apply to measurements with a larger number of interrogation beams. In the new scheme, there is no realistic limitation for the algorithm to the number of cells that can occupy the delay channel and is instead affected most by the presence of multiple cells per droplet or cell clumping, in which cell events are either potentially mismatched or must be discarded. In a properly dispersed single-cell emulsion, with the appropriate input cell density and droplet spacing (which is

considered in the discussion), pair-matching efficiencies exceed 90% for cells that pass the signal threshold at both interrogation regions (likely due to either photobleaching at spot 1 or the increase in FRET signal due to a FRET change near the signal threshold at spot 2). For this study, ~5% of detected cells were discarded in this manner, with 98% pair-matching efficiency for the remaining events (% of those detected cells at spot 2 that were matched to a previous cell event at spot 1).

A flowchart describing the sorting logic is presented in Figure 3.5A. Emission from each single cell passing through an interrogation beam is observed to have a near-Gaussian time profile. The peak times are compiled into a histogram. Given the discrete and stable dynamics of droplet generation, there is a narrow distribution of droplet transit times between the two interrogation spots. For an elapsed run time the average time delay is determined from the difference in peak positions of the frequency histogram from spot 1 (from PMT#1) and spot 2 (from PMT#2). An example time-delay histogram is given in Figure 3.5B. The largest amplitude peak in the histogram, or the most frequent time difference between cells detected, indicates the time delay between interrogation spots. In the event of clusters of cells or frequent multiple cell droplet occupation due to incorrect calculation of input cell density, the timing histogram loses the clean, separated nature of peaks and we observe a broadening in the width of the timing delay, $w_{\Delta t}$. This can have a detrimental effect on pair-matching, which stresses the need for single-cell encapsulation, as discussed later. To determine the time delay for a sorting run, a number of cells are screened prior to sorting. Once the time window has been established, every event detected on PMT#2 is checked against the history of PMT#1 peaks and matched if it falls within the established window. As shown in Figure 3.5A, if no match is made no action is taken. With this process the FRET ratio, R_1, at spot 1 can be matched to the ratio, R_2, at spot 2 to

determine the ΔFRET, R_2/R_1. This parameter provides a very useful sorting gate because it permits identification and sorting of cells that have a large response, yet do not fall in the lowest portion of the unsaturated population and the highest portion of the saturated population as may be found in a heterogeneous sample such as a library.

3.6 Time-resolved differentiation of ZapCV2/ZapCV5 sensor mixture

Determination of the instrument's ability to resolve a mixed-cell population consisting of different binding domains was initially tested through a ~50:50 mixture (determined by a Neubaur cytometer separately and mixed) of NES-ZapCV2 and NES-ZapCV5 expressing HeLa-S3 cells. Figure 3.6A shows the results of this screening experiment at a time delay of 6 seconds. The two populations are unresolvable in their FRET 1 distributions, but following Zn^{2+} exposure, separate into two resolvable peaks by the end of the delay channel. Figure 3.6B is a histogram for data obtained in a separate experiment conducted much later (Apr 2017, compared to Jan 2015 for the previous dataset), but is relevant to the present discussion. A ~50:50 mixture of NES-ZapCY2 and NES-ZapCV2 expressing HeLa cells was screened after Zn^{2+}-pyrithione exposure. The purpose of this experiment was to verify the resolvability seen in the two sensors with different ligand kinetics was also seen in two sensors with the same ligand binding domain, but different acceptor proteins (ZapCY2, ECFP-Zap2-mCitrine; ZapCV2, ECFP-Zap2-cpVenus173).

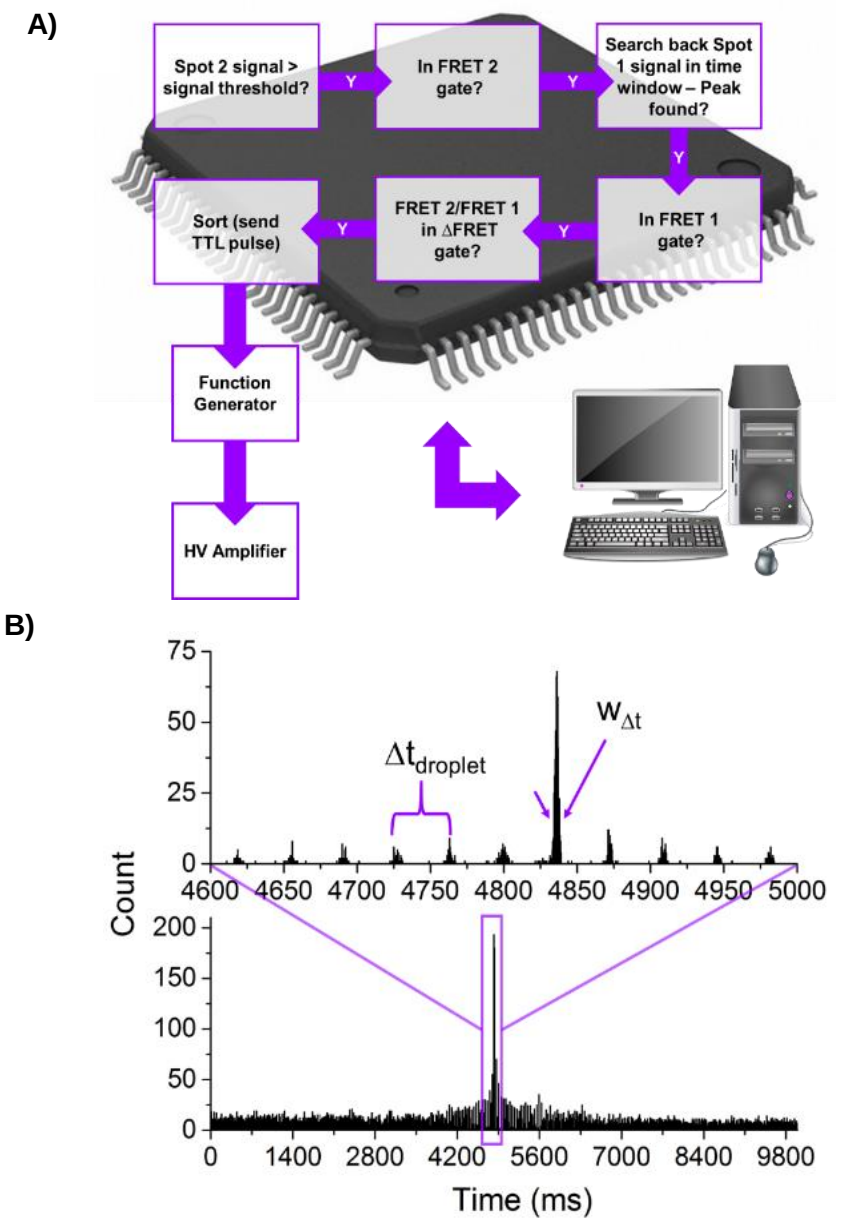


Figure 3.5. a.) Schematic data flow and sorting logic diagram, and b.) a typical histogram of cell event time differences observed between detection spots with annotations representing the droplet spacing in the time domain, $\Delta t_{droplet}$, and the width of the delay time measurement, $w_{\Delta t}$, around the largest peak which indicates the highest frequency time difference (i.e. time delay) used to determine the pair-matching time window gates. Top graph shows an expanded window of the same data set.

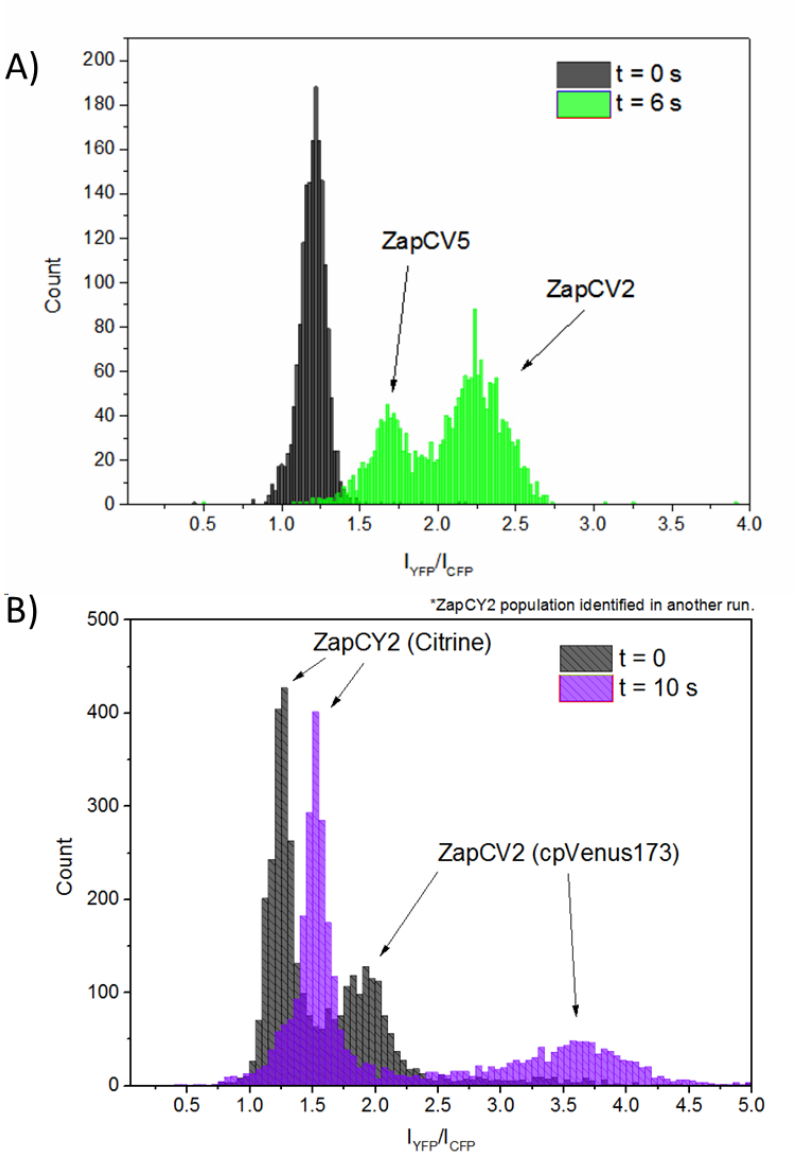


Figure 3.6. A) ~50:50 mixture of NES-ZapCV2 and NES-ZapCV5 after 6 s of Zn^{2+}/pyrithione exposure. An unresolvable FRET 1 distribution separates into two distinct FRET 2 peaks. n = 2000. B) ~50:50 mixture of NES-ZapCY2 and NES-ZapCV2 after 6 s of Zn^{2+}/pyrithione exposure. Two FRET 1 distributions respond with different dynamic ranges. Identity of the peaks was determined by a screening run done immediately after with isolated ZapCY2. n = 2000.

To demonstrate the kinetics of response to Zn^{2+}, HeLa-S3 cells expressing ZapCV2 and ZapCV5 in the cytosol were run separately and the FRET changes were measured over a range of times achievable in a single device by tuning the input pressure (Figure 3.7). The rise time of the response does not significantly differ between sensors and is limited by the timescale for the Zn-ionophore complex to diffuse across the cellular membrane and equilibrate with the sensor pool. Sensor expression and hence concentration is similar for both cell lines. At time delays exceeding 5.5 seconds, the population peak FRET values exceed the width of the FRET distributions for reliable separability. Coefficients of variation for the measurements of these sensors are 9% for spot 1 measurements and range from 10-20% for spot 2 measurements.

3.7 Sorting of a mixed population

To verify sorting accuracy, a stable cell line of HeLa-S3 cells was constructed in which NES-ZapCV2 was co-expressed with mCherry-NLS (nuclear-localization sequence). The fluorescence of mCherry falls outside the optical window for FRET detection and therefore does not contribute to the response. The two cell lines were mixed in either an 80:20 or 90:10 ratio (NES-ZapCV5:NES-ZapCV2), where cell numbers were estimated using a Neubaur hemocytometer. These mixtures were sorted to a target of 3500 cells over the course of 2 hours to enrich the lower percentage ZapCV2 population. Based on the response kinetics determined previously, the cells were sorted with a time delay of 5.6 seconds to provide a balance of resolution *vs.* sorting speed. Figure 3.8 displays a pair-matched scattergram for the sorting experiment with applied gates shown as colored lines and the sorting region shaded in red. After sorting, an aliquot of pre-sorted cells and sorted cells were imaged to quantify the ratio of NLS-mCherry tagged NES-ZapCV2 stable cells versus NES-ZapCV5 stable cells. Cell counts to

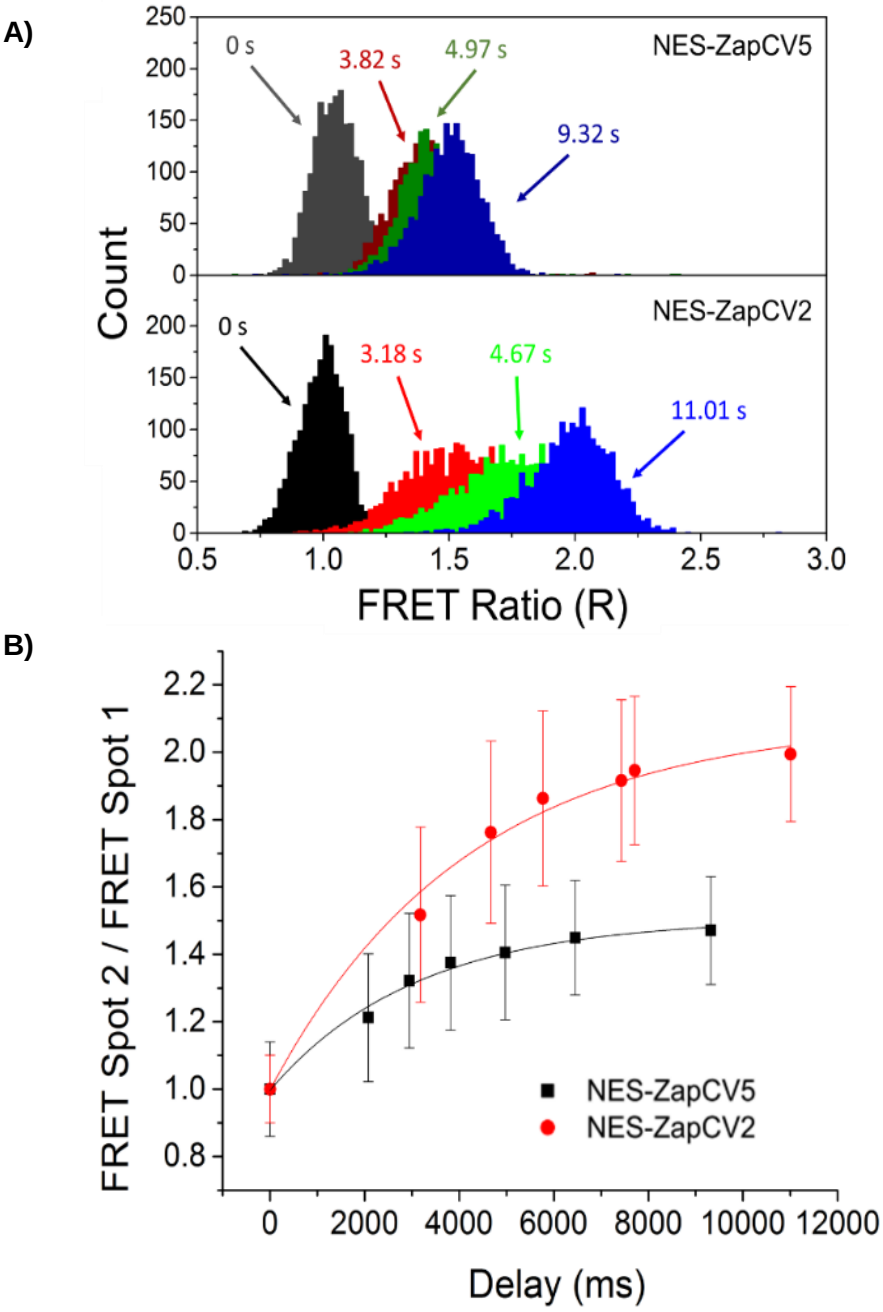


Figure 3.7. A) Histograms of peak FRET ratio (I_{FRET}/I_{CFP}) distribution for the two Zn^{2+} sensors at a selection of delay times, Δt, between interrogation regions (each delay time is represented by a different color) and B) ratio of peak FRET ratio as a function of Δt. Error bars indicate peak half width. Time points (2000 cells each) were obtained on a single device by varying only the pressure inputs. Δt = 0 refers to FRET population at FRET spot 1.

determine enrichment[54] were done manually and indiscernible particles/cells were reported as negatives, therefore reported sorting accuracies are likely artificially low. Example images used for determining sorting accuracy can be found in Figure 3.9. Sorting parameters used for the experiments are summarized in the caption of Figure 3.8. Enrichment information is summarized in Table 3.1. For an estimation of maximum possible enrichment attainable in this experiment, results shown in Figure 3.8 were fit to 2D Gaussian peaks to estimate population overlap. We estimate the percent of ZapCV5 cells that match the gates applied to the sorting experiment have an upper bound of 2.5% of the total cells sorted (with 97.5% maximum ZapCV2 sorting potential or a 130-fold enrichment).

Initial % NES-ZapCV2	Sorted % NES-ZapCV2	Enrichment (η)
23	96	75.1
10	92	96.3

Table 3.1. Cell sorting results demonstrating enrichment of ZapCV2 from an initial mixture of ZapCV2 and ZapCV5. The enrichment, η, is defined as $\left(\frac{N_{ZapCV2}^{sorted}}{N_{ZapCV5}^{sorted}}\right) \Big/ \left(\frac{N_{ZapCV2}^{initial}}{N_{ZapCV5}^{initial}}\right)$.

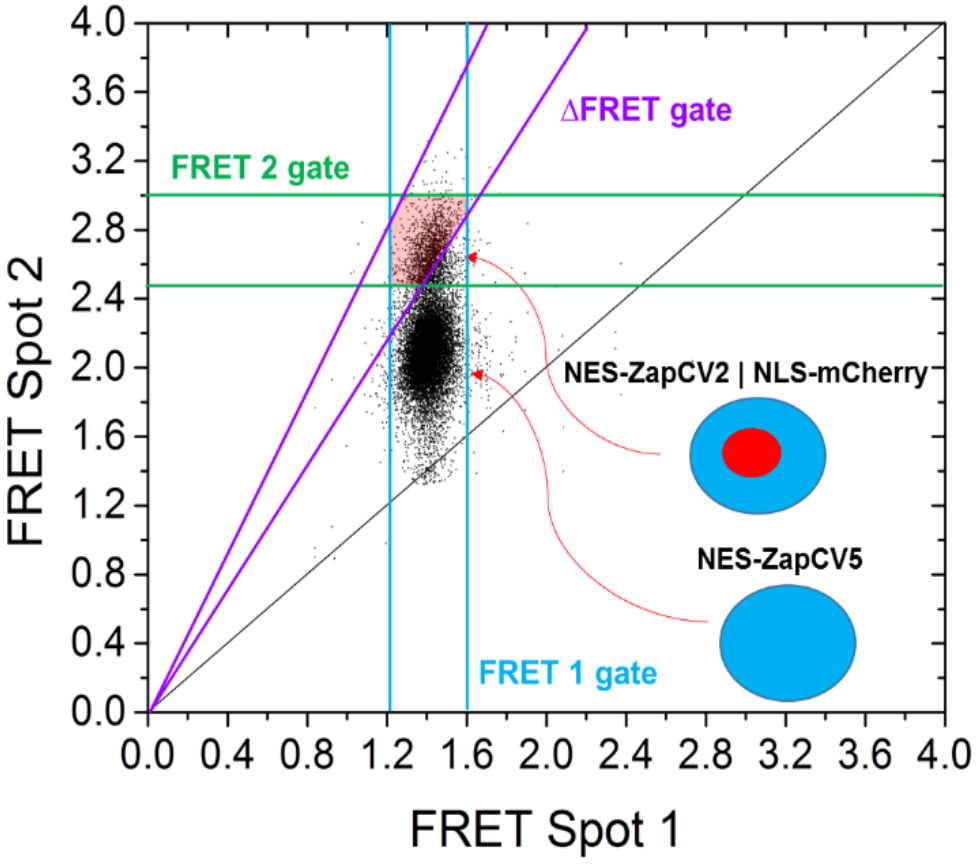


Figure 3.8. Time resolved pair-matched Ratio Spot 2 *vs.* Ratio Spot 1 for sensors in HeLaS3 cells (17,000 cells). FRET 1 Gate: 1.21 - 1.60, FRET 2 Gate: 2.50 - 3.00, ΔFRET Gate: 1.75 - 2.50, time delay: 5.6 ± 0.012 seconds with pair-matching gates applied at 5.6 ± 0.020 sec. The region corresponding to the cells sorted with the applied gates is shaded in red.

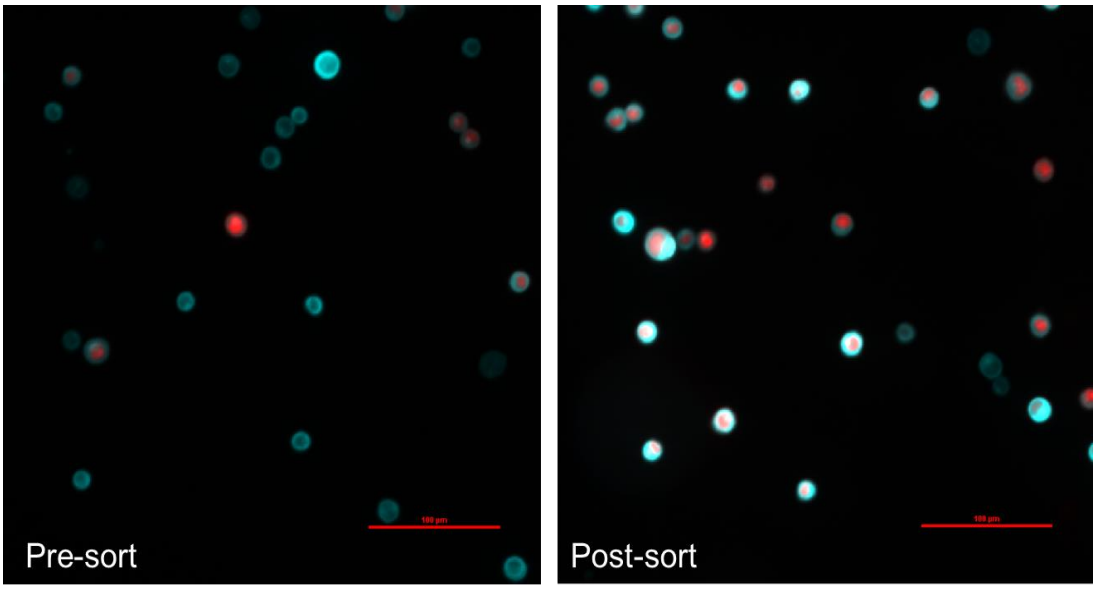


Figure 3.9: Representative, pseudo-colored images using CFP (434/16 excitation, 458 dichroic, 470/24 emission) and mCherry channels (560/20 excitation, 585 LP, 610/50 emission) showing pre- and post-sort collections of cells used to collect data in Figure 3.8. Images were collected using a 20X air objective (NA 0.8), 100 ms exposure time for CFP and 200 ms for mCherry, EM gain 1 MHz at 16-bit readout mode with an EM gain multiplier of 100, and a neutral density filter with 12.5% light transmission. Cell expressing ZapCV2 are coexpressed with an NLS-mCherry. Scale bar = 100 uM.

3.8 Impact of throughput and operation on instrument applications

We now evaluate the scope of potential applications for this instrument in light of its design and operation characteristics. For quantifying heterogeneity of cellular response and for development of new sensors, measurement precision and number of cells screened per session are important performance metrics that are impacted heavily by the inter-dependent factors influencing droplet generation and loading, the time needed for sensor response (delay time), the timing parameters needed for successful pair-matching, and run-time. These factors in turn

determine the sorting rate and accuracy, which are additional considerations for screening and sorting genetic libraries of sensors.

We begin with a discussion of the operational parameters governing droplet generation and the loading of single cells into the droplets, which linearly affects the screening rate of a given device. The factors contributing to droplet control have been discussed previously but will be described here briefly.[85] The parameters used in the discussion of device performance are best illustrated in Figures 2 and 3. Droplet spacing, size, and speed can be adjusted by changing the ratio of aqueous inlet pressures to the oil inlet pressure, P_a/P_o. Increasing the ratio decreases droplet speed and spacing while increasing droplet size. This control is critical for optimizing throughput while preventing droplet collision at the sorting junction, which causes droplets to incorrectly enter the sorted channel. As discussed later, controlling the droplet spacing is also key to successful sorting. The input cell concentration dramatically impacts both sort throughput and sort accuracy. Droplet occupancy, the average number of cells per droplet, follows Poisson statistics.[66] For sorting operations, input cell concentration is chosen to ensure most droplets are empty, which maximizes the probability of single occupation. If the cells are too concentrated ($>2x10^6$ cells/mL) such that a large number of droplets are doubly occupied, the sorting throughput decreases as potentially desirable cells will be discarded when gating or potentially undesirable cells will be sorted if one is below the set signal threshold which will decrease sorting purity. At the opposite extreme, the throughput will be low if the cell concentration is decreased ($<1x10^6$ cells/mL). Occupancy also depends on the droplet size. Generally, the cell concentration is tuned such that 90% of droplets are unoccupied and therefore < 1% chance double or higher occupancy. For the measurements presented here, with a cell input

concentration of ~1-1.5x10^6 cells/mL, the droplet volume was ~ 200 pL with half of the volume taken by the cell input fraction.

To continue the discussion of throughput and to justify the use of this technique for a range of sensors, it is necessary to point out the factors in determining and setting the delay time for a given microfluidic device. The available range of delay times permitting the screening of alternate sensors that have much faster (> 50 ms) or moderately slower (< 15 sec) kinetics of response is determined by the input pressures and the device geometry. Longer delays are preferably achieved by increasing the length of the channel between the two interrogation regions. The increased output resistance is then compensated with an increase in the fluidic resistance of the input channels. Increasing the delay by decreasing input pressure, necessitates a decrease in fluid speed, which is undesirable because it decreases cell throughput given the limitation in cell concentration that can be used to maintain single cell droplet occupancy. Assuming cell concentration cannot be arbitrarily raised as discussed previously and delay line crowding is not a factor, by increasing the delay channel length, the throughput and delay time both increase. We found that delay channel lengths beyond 250 mm (> 15 seconds delay) pose operational challenges that limit performance. For example, longer channels present more opportunities for pressure fluctuations and vibrations to affect droplet spacing and thus the consistent flow of droplets between interrogation points. This becomes limiting at a point as it requires higher driving pressures to sustain desired time delays and stable flow: irreversible bonding of PDMS to borosilicate glass is rated for ~30-50 PSI input before delamination/failure.[86] For the experiments presented in this work, a delay channel of 140 mm was used. Flow speeds in this device are adjustable from 10 mm/s to 250 mm/s with continuous phase driving pressures of 1 – 20 PSI. It should be noted that, while this delay length was chosen

for this experiment, several lengths were tested and utilized, from a direct path between interrogation beams as might be ideal for rapid extracellular sensor response to the 250 mm device mentioned above, for sensor screening at a variety of ligand concentrations to observe heterogeneity and response timing. In adjusting pressures to generate a particular delay time it is important that cells do not dwell in the channel prior to the low FRET interrogation region, as increasing the droplet spacing will slow the aqueous phase flow velocity relative to the continuous phase. It important to limit pre-interrogation exposure to ensure proper assessment of the low FRET state ratio as arbitrarily slowing the flow speed can eventually exceed the time it takes for Zn-pyrithione to penetrate the cell membrane and begin equilibrating with the sensor, causing a rise in response at the first interrogation beam. The mixing times for the small ion-metal complex can be estimated for the short, straight channel after mixing but before droplet generation and we provide simulated results in Figure 3.10. In short, within the operating range of flow velocities, mixing is incomplete prior to the cell reaching the droplet generator where cell position becomes highly variable and more complicated advection takes place within the droplet. It is reasonable at this point that the cell experiences saturating ligand concentrations due to the use of ligands concentrations several orders of magnitude above the K_D of the sensors and the rise of the sensor response is expected to be dominated by membrane permeation. Under the concentrations and geometry used in this study, no increase in FRET is found for the first spot until flow speeds in the mixing region decrease below 2.5 mm/s or 120 ms spent in the mixing region. In practice, it is best to modulate the input pressure ratio and monitor the low FRET population to verify it does not show an increase at the across the desired delay times.

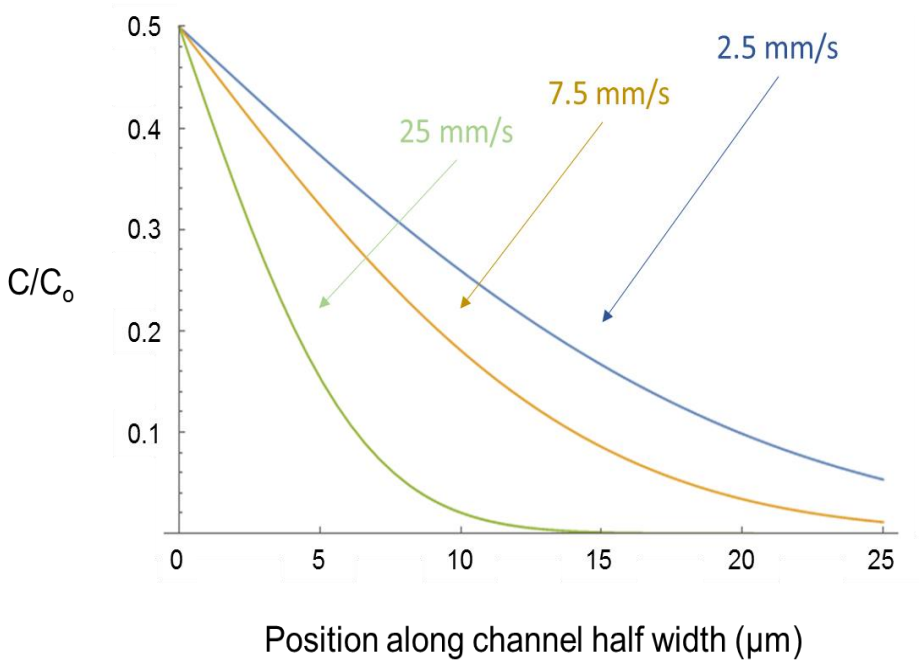


Figure 3.10: A slice of the calculated concentration profile at x = 300 μm (where x is the distance along the axis of flow) after the mixing junction. The y-axis shows the concentration C, normalized by the input concentration C_o. The x-axis is the position along the width of the channel, beginning in the middle. Equation used is $\frac{C(x,y)}{C_o} = \frac{1}{2}\left(1 - erf\left(\frac{y\sqrt{U}}{\sqrt{4D_{eff}x}}\right)\right)$, where y is the distance perpendicular the axis of flow, U is the flow velocity, and D_{eff} is the effective diffusion constant (estimated at 1E-9 m^2/s for the small ion/ionophore complex). Plotted at a series of flow velocities relevant to chip operation.

Lastly, the parameters necessary to obtain successful pair-matching and accurate determination of the timing variables are the most stringent and limiting with regards to throughput and are inextricably linked to the parameters discussed in previous paragraphs. The width of the time window for pair-matching and sorting is limited by the closest spacing between occupied droplets and the timing variation introduced by the cell position in the droplet. The spacing between droplets can be increased by increasing the pressure of the oil input to provide a time interval during which a cell event is not detected. The key to successful pair-matching is to maintain a droplet spacer larger than the variation in cell arrival time. The largest contributor to this variation is typically the variation in cell position in the droplet along the axis of flow. This spatial variation increases with the size of the droplet. For constant volume, the timing width scales linearly with the droplet speed. At the sorting speeds employed here, the contribution from cell position in the timing width is about 3 ms at 25 mm/s and a 5.6 s delay. Droplet spacing in the time domain is typically 15 ms or greater, owing to the large spacing required to prevent droplet collision at the sorting junction. This generally limits our potential cell sorting rates to < 7 s^{-1} at our cell concentrations and desired droplet occupation frequency (~9 %). For shorter delay lengths, faster responding sensors (*i.e.* extracellular sensors), and less stringent sorting accuracy the cell throughput can be raised.

A potentially powerful application of this instrument would be screening a library of sensors in mammalian cells and selecting winning sensors based on direct measurement of sensor response in the target environment of interest (i.e. mammalian cells). This could be accomplished by generating a library of sensor plasmids with mutations specifically targeting linker and ligand binding domains, and incorporating the library into mammalian cells by viral transduction. A low multiplicity of infection could be used to ensure that each mammalian cell

is statistically likely to be infected by a single virion, and hence express only a single library member.[87] Transduced cells could then be enriched, if necessary, by FACS or antibiotic selection markers. This heterogeneous population of cells, each expressing a single library clone, could then be screened with our instrument for ligand response. The diversity of FRET responses within a library is likely to far exceed the difference between the two sensors in the mixture reported here. Cells that respond above a designated threshold could be collected and analyzed for high dynamic range clones. Depending on the nature of the reagents, the cells could then be expanded and subjected to additional rounds of sorting or, if the reagent treatment renders cells non-viable, DNA could be immediately extracted and analyzed by deep sequencing.[88,89] The sorter is set up to run with minimal interference for several hours with sorting rates typically on the order of 2-5 s^{-1}, or up to 20,000 hr^{-1}, facilitating the screening of libraries on the order of 10^4 with several-fold coverage over a run time of a few hours.

While the throughput is inherently limited by the timing parameters required to successfully make a measurement, we remark that it is orders of magnitude faster than the equivalent throughput for screening large numbers sensor variants in mammalian cells. This contrasts droplet technology for single time point fluorescence interrogation, which approaches FACS-like speeds on the order of kHz cell throughputs.[57] Our instrument is comparable of sorting speeds on the order of 1-10 s^{-1} and 50-150 fold enrichment found in technologies utilizing optical trapping, electro-osmosis, and hydrodynamic mechanisms for cell sorting.[90–97] Low coefficients of variation < 20% are achievable, likely due to the consistent and fast exposure each cell experiences to the saturating ligand and ionophore complex. This offers an improvement to the plate-based technologies for FRET sensors mentioned in the introduction.

3.9 Conclusions

This work presents a cell sorter for the screening and enrichment of biological systems that exhibit transient intensity signal or ratiometric signal changes on a millisecond to second timescale. Due to the flexibility of microfluidic technology, the idea can be easily extended to other systems that do not require mixing steps, but rather other methods of signal modulation (i.e. optical photoswitching or clustering events) or require more time points.

Chapter 4

Systematic Evaluation of ER Sensors and Development of a Sensor Linker Library

4.1 Publication Note and Author Contributions

Portions of this chapter were adapted from Carter, K.P; Carpenter, M.C.; Fiedler, B.L. *et al*. Critical Comparison of FRET-sensor Functionality in the Cytosol and Endoplasmic Reticulum and Implications for Quantification of Ions. *Anal. Chem.* (2017) (in review at time of thesis submission) and corresponding Supplementary Information. Figures present in the publication are unmodified in this chapter. Microfluidic work was performed by BLF. *In vitro* studies were performed by MCC. Imaging experiments were performed by KPC and MCC.

4.2 Genetically Encoded Zn^{2+} Sensors Targeted to Subcellular Organelles

Fluorescent sensors are powerful tools for visualizing and quantifying ions, metabolites, and other species in cells, offering the potential to define the concentration and spatial distribution of such species. Realizing this potential requires systematic and careful

characterization of sensor platforms in the complex environment of a living cell and in different subcellular locations. The need for a robust analytical framework for comparing sensor performance and defining sensor functionality in different cellular locations is illustrated by comparing the three families of genetically-encoded FRET-based sensors, Zap, eCALWY, and eZinCh, which have been applied to define Zn^{2+} pools within the cell.

Each family is engineered by fusing fluorescent proteins (FP) to Zn^{2+} responsive protein domains. The Zap family links a donor CFP to an acceptor citrine YFP through the zinc-binding domain of the yeast transcription factor Zap1.[41] In the eCALWY family of sensors, cerulean FP and citrine YFP were mutated to recognize each other in the apo state of the sensor, and the metal-binding domains of Atox1 and WD4 were engineered to coordinate Zn^{2+}.[34] In the eZinCh family a Zn^{2+} coordination site was directly engineered into an interface between the β-barrels of cerulean and citrine, which were connected by a flexible linker.[35] A notable benefit of genetically-encoded sensors is that they can be targeted to organelles by fusing small peptide signaling sequences to the sensors. Members of these families of sensors have been targeted to different cellular compartments including: cytoplasm, mitochondria, Golgi apparatus, nucleus, and endoplasmic reticulum (ER).[41,35,98,83,42] Application of multiple platforms for measuring analytes in cells can increase confidence in the robustness of both the tools and their measurements. These three sensor platforms have been used in the cytosol to estimate labile Zn^{2+} within an order of magnitude, 82–600 pM.[30,99] In contrast, when the same sensors were targeted to the ER of HeLa cells the estimates of labile Zn^{2+} ranged widely from 0.9–1600 pM.[41,35,42] Qualitatively, ZapCY1 is more saturated in the cytosol than in the ER, while eCALWY-4 displays the opposite saturation pattern and eZinCh-2 is about equally saturated in both the ER and the cytosol.[41,35,42]

It is possible the chemical environment of the ER (pH, crowding, or redox state) differentially affects sensors, impacting sensor functionality and accuracy of quantifications. Defining whether the labile Zn^{2+} concentration is higher in the ER than in the cytosol is an important fundamental question in Zn^{2+} biology in order to establish whether the ER might serve as a store of Zn^{2+} that could be mobilized for cellular signaling. For these reasons, it is becoming increasingly clear that methodology for the optimization of sensors in the chemical environment they will ultimately be used is crucial. Additionally, establishment of the parameters that can be modified to improve these sensors should also be identified.

The overall goal of this work is to establish a framework for critically comparing ratiometric FRET-based sensors in an organelle of interest by comparing ZapCY1, eCALWY-4, and eZinCh-2 in the ER and cytosol of HeLa cells. In this thesis, focus will be drawn to the results generated from the microfluidic work. These findings will be extended to the generation of a linker library for the purpose of generating an improved ER sensor.

4.3 Experimental Setup

4.3.1 ER Sensor Cloning and Cell Culture

The instrument and assay are used as described in Chapters 2 and 3. For the ER sensor screening experiments, cells used in the microfluidic experiments are grown and transfected identically to those used in the microscopy experiments done alongside (presented in Figure 4.2). Plasmids containing eCALWY-4 and eZinCh-2 were obtained from Addgene, catalog numbers 22236 and 70009 respectively. In order to control for possible difference in transfection efficiency and protein expression due to differences in plasmid backbone or organelle targeting sequence, all three sensors were cloned into the same pcDNA3.1 backbone. The sensors were

targeted to the cytosol using the same nuclear exclusion peptide sequence (MLQLPPLERLTL), and targeted to the ER using the same calreticulin sequence (MLLPVPLLLGLLGA). eCALWY-4 and eZinCh-2 were PCR amplified and cloned into pcDNA3.1 between restriction sites BamHI and EcoRI using InFusion homologous recombination kit (Clontech) according to the manufacturer's instructions. HeLa cells (ATCC CCL-2) were cultured in DMEM medium (Invitrogen) supplemented with 10% fetal bovine serum and penicillin/streptomycin at 37°C with 5% CO2. All sensor constructs were transiently transfected with TransIT-LT1 (Mirus Bio) according to the manufacturer's instructions.

After the 48 hour transfection, cells are harvested using 0.05% trypsin-EDTA. Cells are centrifuged and resuspended in phosphate, calcium, and magnesium-free HEPES-buffered HBSS (R_{max} buffer) with 150 µM TPEN and incubated at room temperature for 10 minutes. Cells centrifuged again and resuspended in R_{max} buffer to rinse. Cells are subjected to one final spin down and resuspended in a microfluidic suspension buffer consisting of 0.1% BSA, 16% v/v Optiprep and 1 µM TPEN in R_{max} buffer on ice. The reagent buffer contains 100 µM $ZnCl_2$, 100 µM pyrithione, and 0.1% saponin for a final droplet concentration that is half of the stated values. Cells are kept on ice until placement in the microfluidic setup and are then kept at room temperature in a pressurized reservoir for the ~1-2 hour duration of the experiment. Delay channel length used in this experiment was 140 mm with applied pressures ~7 PSI per fluid reservoir to achieve the 7.5 second delay.

4.3.2 Library Cloning

For the library screening and sorting experiments, identical conditions were used to harvest and prepare the cells, but HeLa-S3 cells were used in place of HeLa cells.

CloneAmp HiFi PCR Premix (Clontech) was used for all PCRs according to the manufacturer's instructions. All restriction enzymes were obtained from New England Biolabs (NEB). All recombination or ligation reactions were transformed into Stellar competent *E. coli* cells (Clontech) and plated on LB with 100 µg/mL ampicillin.

Codon-diverged mCitrine, codon-diverged ECFP and codon-optimized Zap2 Zn^{2+}-binding domain were ordered as gBlocks (IDT) and recombined into a pBAD vector backbone using the In-Fusion HD Cloning Kit. The backbone was prepared by digesting ZapCY2 in pBAD with *Sph*I-HF and *Eco*RI-HF. The sensor fragment (OptiZap) was digested out of the vector using *Bam*HI and *Eco*RI-HF, then recombined using the In-Fusion HD Cloning Kit into a pcDNA3.1+ vector backbone (Invitrogen) with a 5'–calreticulin signal sequence (*MLLPVPLLLGLLGAAADG*) and a 3'–ER retention tag (*KDEL*). The sensor was then transferred to pLVX using the In-Fusion HD Cloning Kit.

To construct the libraries, the ZBD was amplified using OptiZap in the pLVX vector as a template using degenerate primers and recombined into pLVX using the In-Fusion HD Cloning Kit. Prior to the recombination reaction, all PCR products were gel purified using the Monarch DNA Gel Extraction Kit (NEB). The small libraries (< 1,000 variants) were plated on standard 10 cm agar dishes, while the larger libraries were plated on 20 cm dishes.

Once the genomic DNA was purified from cells (*vide infra*), the ZBD could be amplified by PCR. Initially, the ZBD was amplified with optizapZBDseqV1fwd (5'–*GGCGCATTCAAGATCAGACAC*–3') and optizapZBDseqV1rev (5'–*GGGCAAAACACATCAGGCCAT*–3'). The thermal cycler protocol used was 98°C for 3 minutes, then 23 cycles of 98°C for 15 seconds, 72°C for 75 seconds, then finally 72°C for 3 minutes, then the product was gel purified. For verifying cell lines, the purified PCR product was ligated

into the pJET2.1 vector using the CloneJET PCR Cloning Kit (Thermo Fisher Scientific), transformed into Stellar cells and plated on LB with 100 µg/mL ampicillin. For cloning the sorted cells, the pLVX vector was amplified from OptiZap in pLVX using PLVXsensorhits.rev (5'–*GTTGTGTCTGATCTTGAAGTGCGCCTTGATTCCGTTTTTTTGCTTGT CGG*–3') and PLVXsensorhits.fwd (5'–*GGCTATGGCCTGATGTGTTTTGCCCGGTACCCAG ATCATATGAAACAG* –3'), gel purified, and recombined with the ZBD PCR product using the In-Fusion HD Cloning Kit. Alternatively, to minimize parent sensor contamination during this step, the ZBD was amplified from gDNA using KeepersPLVXfwd (5'–*TTCCGGTGAATTCCTCGAGACTAG TGCGGC*–3') and KeepersPLVXrev (5'–*CGAGGGTGCGTACGGCCCGG*–3') with 0.5 M betaine and 5 % DMSO. The pLVX vector was digested with *Spe*I-HF and *Xma*I-HF for 16 hours at 37°C. Both products were gel purified and recombined together using the In-Fusion HD Cloning Kit.

4.3.3 Mammalian Cell Culture for Libraries

HeLa S3 cells (ATCC CL-2.2) and HEK293T cells (ATCC CRL-3216) were cultured in Dulbecco's Modified Eagle Medium (DMEM) (Gibco) supplemented with 10 % fetal bovine serum (FBS) at 37°C with 5% CO_2. Cells were split twice per week at a splitting ratio of 1:8 (HeLa S3) or 1:10 (HEK). HEK cells were transfected with viral plasmids using TransIT-LT1 (Mirus) according to the manufacturer's instructions.

4.3.4 Viral Transduction for Libraries

HEK293T cells were seeded in 15 cm plates at a density of 4×10^6 cells per plate. 24 hours later, the cells were transfected with lentiviral packaging plasmids and viral expression

plasmid (pLVX) containing a single Zn^{2+} sensor or a library of linker variants. The packaging plasmids were a gift from Professor Hubert Yin (CU Boulder). There are three plasmids required to package lentiviral particles: pRev (which contains the reverse transcriptase), pMDL (contains the Gag and Pol genes), and pVSV-G (contains the envelope protein). The packaging plasmids were mixed with equivalent amounts of each other and pLVX, usually 5 µg each plasmid per 15 cm plate, in 1 mL of OptiMEM reduced serum medium (Thermo Fisher). TransIT-LT1 (3 µL per 1 µg of DNA) was then added dropwise to the DNA mixture and the transfection complexes incubated at room temperature for 20 minutes before adding to cells. After 24 hours, the transfection complexes were removed from the HEK293T cells and fresh medium was added. The viral supernatant was harvested between 48-72 hours after transfection. Supernatant could be harvested multiple times over this period, always replenishing the medium on the HEK293T cells until the protocol was finished. The supernatant was gently filtered through a 0.45 µM surfactant-free cellulose acetate filter and either used immediately to transduce HeLa S3 cells or stored at 4°C. Supernatant from multiple harvests of the same virus could be pooled together. If desired, the viral particles were concentrated using a SW-28 rotor in an L-70 Ultracentrifuge (Beckman) at 25,000 rpm for 2 hours at 20°C. The supernatant was carefully aspirated and the viral pellet was resuspended in 1 mL DMEM.

Viral particles were added to HeLa S3 cells when the cells were 50-70 % confluent in a 6-well plate, 10 cm dish, or 15 cm dish, depending on the number of cells needed. Growth medium was removed from the HeLa S3 cells and replaced with fresh medium. Viral supernatant was then added (no more than 1/3 of the total medium on the cells) as well as hexadimethrine bromide (polybrene) at a final concentration of 8 µg/mL). 24 hours after adding viral particles, the medium was replaced on the HeLa S3 cells and they were trypsinized and transferred to a larger

dish if needed. Puromycin was added at 2 µg/mL 48-72 hours after adding viral particles to select cells that were successfully transduced. After 2-3 days of puromycin selection, the medium was replenished and the cells were allowed to grow.

4.3.5 Genomic DNA Extraction

Genomic DNA (gDNA) was purified from cells using phenol/chloroform organic extraction and ethanol precipitation. After harvesting or sorting, cells were resuspended in 200–400 µL gDNA extraction buffer (10 mM Tris, 1 mM EDTA, 0.1 M NaCl, 1 % SDS, pH 8.0) with 2 µL Proteinase K (NEB) and incubated for 16 hours at 37°C in a shaker at 200 rpm. The mixture was then extracted twice with equal volume phenol–chloroform–isoamyl alcohol mixture 25:24:1 (Sigma Aldrich) then twice with chloroform:isoamyl alcohol 24:1 (Sigma Aldrich). For extractions, organic solvents were added to the buffer and the mixed thoroughly by vortexing for 30 seconds. The organic and aqueous phases were separated by centrifugation at 13,000 × g for 2 minutes. The upper aqueous layer was transferred to a new tube. After the last phenol:chloroform extraction, DNA was precipitated by adding 20 µg RNA-grade glycogen (Thermo Fisher), 1/10 volume 3 M sodium acetate pH 5.2, and 3 volumes 100 % ethanol, mixing thoroughly, and incubating at –20°C for 4–6 hours. The gDNA was then pelleted by centrifugation at 16,000 × g for 30 minutes at 4°C. After aspirating the supernatant, the pellet was washed with 200 µL ice-cold 70 % ethanol and centrifuged at 16,000 × g for 5 minutes at 4°C. The resulting pellet was first air dried for 5 minutes, then resuspended in 20 µL TE buffer (10 mM Tris, 1 mM EDTA, pH 8.0) for 16 hours at 37°C in a shaker at 200 rpm.

4.4 Zn^{2+} Sensor Response in Subcellular Organelles

It was previously shown that the microfluidic cytometer introduced in the last chapter was capable of screening and differentiating sensor response with sensors targeted to the cytosol. General interest led to the examination of a high dynamic range sensor targeted to several cellular organelles. ZapCY1 was used in a few preliminary screening experiments in which it was localized to the cytosol, mitochondria and endoplasmic reticulum. The previously published dynamic ranges for this sensor is ~4, ~3.2, and 2.16 respectively.[41,98] As shown in Figure 4.1, it is clear that the cytometer is capable of resolving a response in each organelle on a timescale of a few seconds when transiently expressed in HeLa-S3 cells. However, it is also apparent that on this timescale, in this cell line, that the response does not achieve the same response magnitude relative to their respective dynamic ranges shown through long timescale microscopy experiments. The responses do appear in the same relative order as their dynamic range, with the ER sensor responding the least and the cytosolic sensor responding the most. Therefore, the cytometer was deemed capable of analyzing the response of organelle-targeted Zn^{2+} sensors.

4.4 Heterogeneity in the Unbound State

This cytometer permits measurement of variability in FRET states and FRET responses in thousands of cells to assess variability at the population-level. Here, the microfluidic cytometer is used to compare cytosolic and ER-targeted sensors for all three sensor platforms alongside traditional microscope calibration experiments (Figure 4.2). A distinct advantage of this platform is the ability to introduce reagents in a controlled manner that does not vary from cell to cell or experiment to experiment. However, the time window to resolve a sensor response

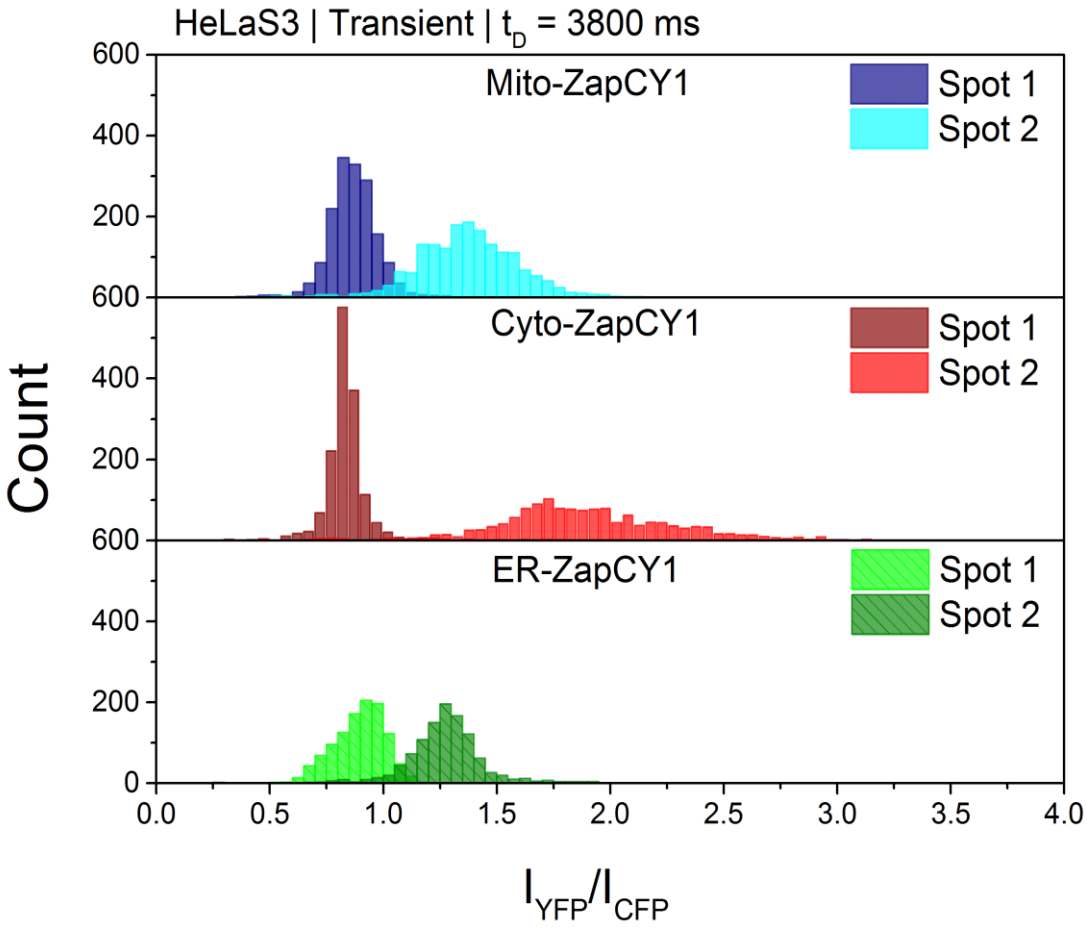


Figure 4.1. FRET histograms for the high dynamic range sensor, ZapCY1, localized to the mitochondria (top), cytosol (middle), and ER (bottom).

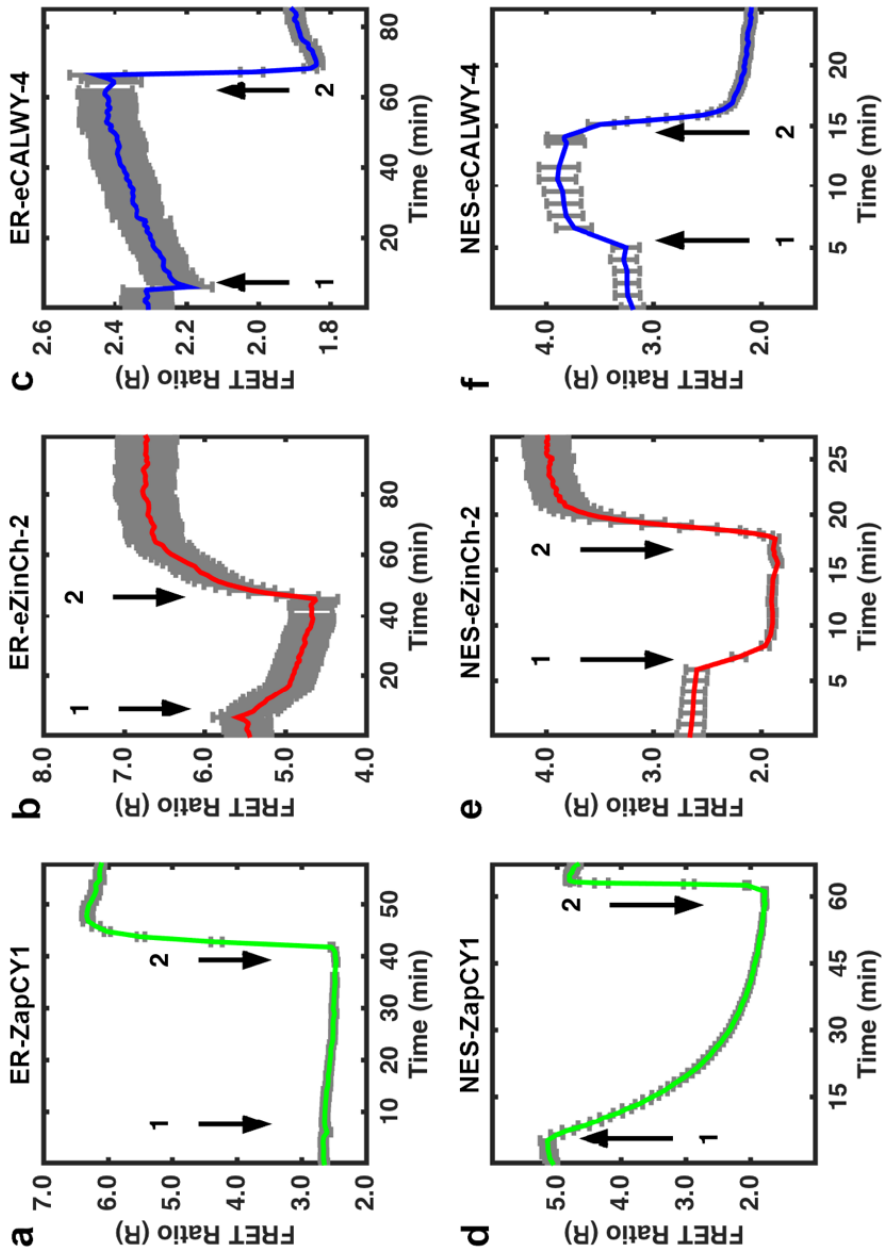


Figure 4.2. Optimization of zinc conditions for ER (a-c) and NES (d-f) sensors: ZapCY1 (green), eZinCh-2 (red), eCALWY-4 (blue). Arrows indicate washing of cells followed by addition of solutions containing 100 mM $ZnCl_2$ + 5 µM pyrithione (grey lines), 2 nM buffered Zn^{2+} + 0.75 µM pyrithione (black lines, not done for NES sensors (d-f)), or 2 nM buffered Zn^{2+} + 0.75 µM pyrithione + 0.001% (w/v) saponin (lines in color) to cells treated for 40 minutes with 50 µM TPEN. (credit: KPC and MCC)

is limited by the high resistance device geometry. Therefore, these measurements assess the sensor response within a short time window (7.5 sec), which only correspond to a part of the full magnitude of the response. Figure 4.3 shows an estimated window of sensor FRET response on a microscopy-obtained calibration trace of ER-ZapCY1 based on the conditions used in the microfluidic screening experiments. This calibration trace was obtained using the same, high Zn^{2+}/pyrithione concentrations used on the device, rather than the low concentrations used for a calibration experiment. During the first several seconds there is a significant rise in the response, but milliliter scale volume diffusion Zn^{2+}/pyrithione results in slower mixing times used in the microscopy calibrations. The full response does not occur for hundreds of seconds. It should be noted that this figure corresponds to ER-localized sensor only and that response in the cytosol nears saturation as shown in the previous chapter. In measuring the response to Zn^{2+}, it is important to note that transport and accumulation of Zn^{2+} in cells is rate limiting as proven in a previous publication.[82] Additionally, these measurements are made in HeLa cells to remain consistent with the microscopy experiments done alongside this work. It has not been demonstrated to achieve the same response under the same Zn^{2+} and pyrithione conditions and the same time delays when compared to HeLa-S3 cells for the ER localized sensors. There is a notable size difference observed for non-adherent HeLa cells and non-adherent HeLa-S3 cells. HeLa cells appear to have sizes ranging from 15-25 μm while HeLa-S3 vary between 10-15 μm. The smaller sensor response is likely due to Zn^{2+} diffusion and equilibration with the sensor pool across a larger volume. It is also possible that the Zn^{2+} buffering capacity of HeLa cells and HeLa-S3 cells differ. Therefore, the FRET 2/FRET 1 values do not represent the full dynamic range of the sensor under saturating conditions, and instead indicate the ratios at 7.5 sec after Zn^{2+} treatment. Given these considerations, the platform is used to define the initial FRET ratios

and variability of ratios in the apo state, and examine the qualitative responsiveness of sensors upon addition of Zn^{2+}, as opposed to the magnitude of response (i.e. dynamic range), within the defined time window.

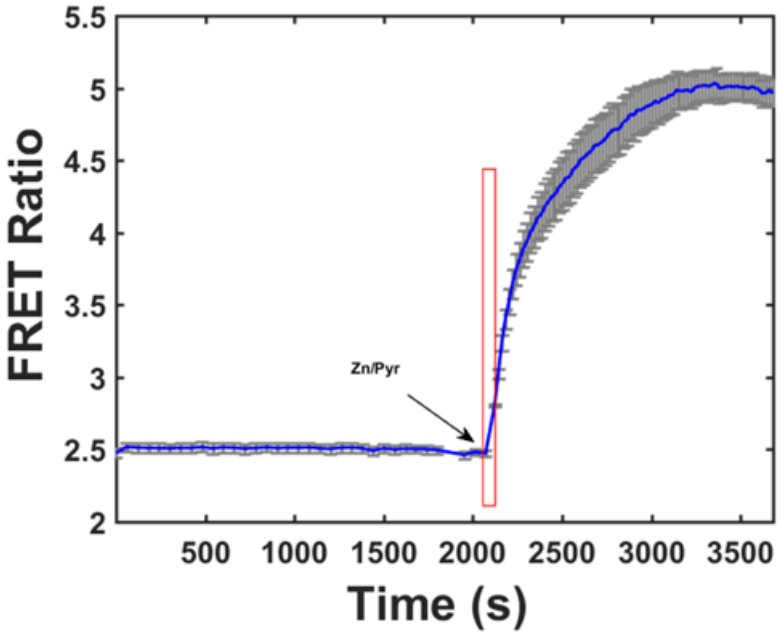


Figure 4.3. ER-ZapCY1 sensor calibration trace with a red box denoting the general region of sensor response probed by the microfluidic cytometer using reagent concentrations used for the microfluidic experiments. It is important to note that this time window, which is set by the microfluidic geometry, is too short to allow for a full sensor response in the ER. Cells were pre-treated with 150 µM TPEN for 10 minutes. Cells are washed and exposed to 5 µM TPEN (start of imaging) for 30 minutes before exposure to 50 µM pyrithione and 50 µM $ZnCl_2$. n = 7 cells.

Since the measured FRET populations did not exhibit a normal distribution, median based statistics were used to assess the center and heterogeneity of the cell populations. The robust coefficient of variation (RCV) was used to describe the width of the distribution, which serves as an indicator of the heterogeneity of a sensor in the apo state. RCV is defined as

$$RCV = 0.75 \times \frac{interquartile\ range}{median}, \qquad (4.1)$$

and expressed as a percentage.

Figures 4.4a and 4.4b show histograms of single cell FRET populations at FRET 1 and FRET 2 for ER- and cytosol-targeted sensors, respectively. The median and RCV values for sensors in each compartment are presented in Table 4.1. Comparison of these values for each sensor provides evidence to whether there were differences in the FRET state in different compartments. ZapCY1 showed similar RCV in the two locations (11.1% and 9.3% in ER and cytosol, respectively) suggesting comparable sensor heterogeneity, and a small, but significant shift in the median FRET 1 ratio when localized to the ER (1.01 versus 0.92 in the ER and cytosol, respectively). The eCALWY-4 sensor showed similarly broad FRET 1 distributions in the ER and cytosol (22.8% and 26.5%, respectively), indicative of increased sensor heterogeneity in both locations compared to ZapCY1, and a significant shift in the median FRET ratio from 0.97 (ER) to 1.55 (cytosol). The eZinCh-2 sensor yielded the tightest FRET 1 distribution in the cytosol (RCV = 5.1%), indicating minimal heterogeneity, but the broadest distribution in the ER (RCV = 32.4%). For eZinCh-2 the FRET 1 median ratio shifted from 1.42 in the ER to 1.03 in the cytosol. Indeed, in all sensors there is a shift in FRET 1 in the direction of sensor response (shift high in ZapCY1 and eZinCh-2, shift low in eCALWY-4) when the sensor is moved from

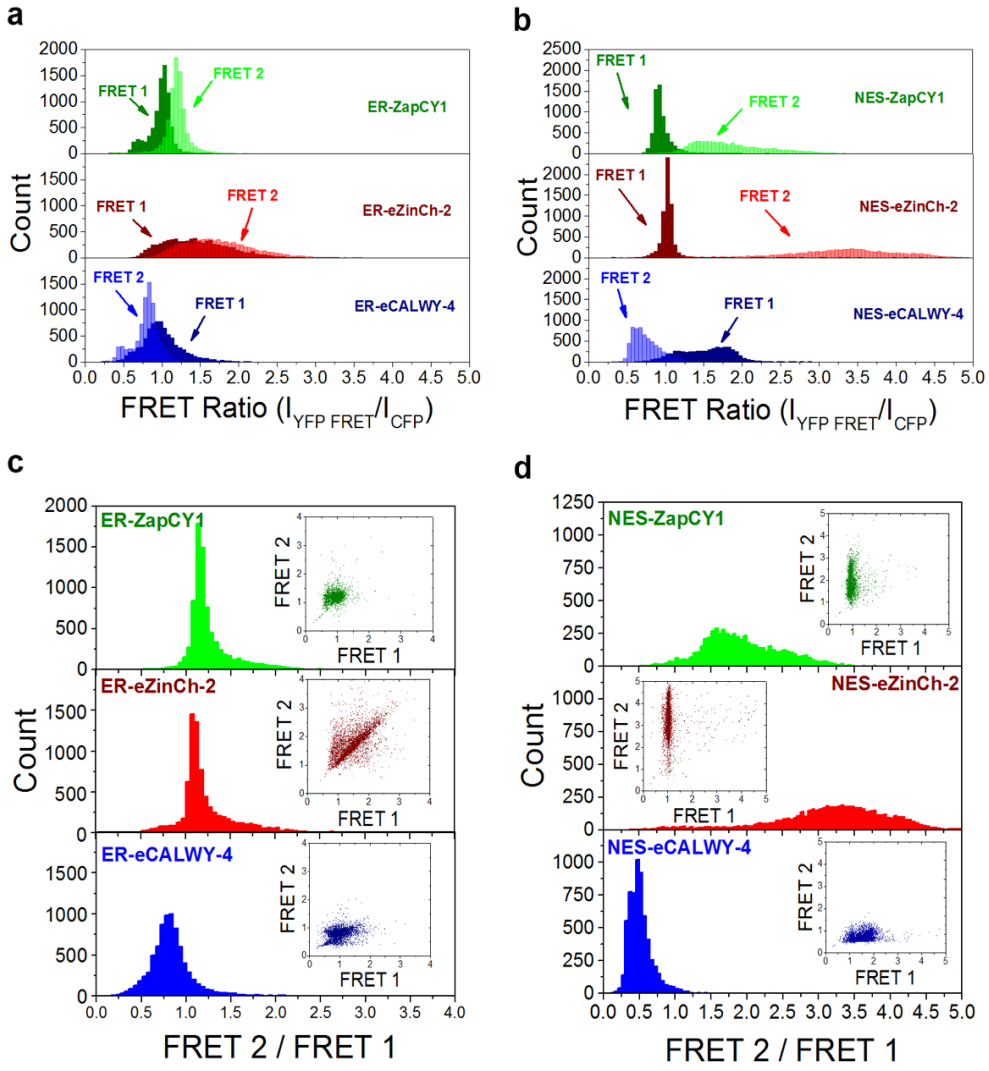


Figure 4.4. Microfluidic analysis of FRET sensor response. FRET ratio histograms for HeLa cells expressing ER (a) or cytosol (b) targeted sensors indicating FRET 1 and FRET 2 cell populations. Corresponding pairmatched FRET ratio histograms showing FRET response to pyrithione and Zn^{2+} for ER (c) and cytosol (d) targeted sensors. Inset scattergrams show FRET response on the single cell level. Time delay between FRET 1 and FRET 2 for all data shown is 7.5 seconds. Sample size for each plot is 6500 cells.

the cytosol. Collectively, these data reveal that localization to the ER can introduce significant heterogeneity into the apo state of a sensor, as well as modifying the baseline FRET state of the sensors.

	NES-		ER -	
	Median (x_c)	RCV	Median (x_c)	RCV
ZapCY1	0.92	9.3%	1.01 (0.77, 1.03)	11.1%
eCALWY-4	1.55 (1.21, 1.75)	26.5%	0.97	22.8%
eZinCh-2	1	5.1%	1.42	32.4%

Table 4.1. Median and robust coefficient of variation (RCV) statistics calculated from the FRET 1 distributions in Figures 4.4 and 4.5. ER-ZapCY1 and NES-eCALWY-4 were fit with two Gaussians due to the bimodal distribution observed. The center of each Gaussian was used to estimate the centers (x_c) of the apparent multiple peaks. For these sensors the median represents the weighted average of the centers of the two peaks.

It was demonstrated that sensor performance can be adversely impacted by the oxidizing environment of the ER which can lead to formation of protein oligomers and reduced dynamic range. Although all three sensor platforms showed some degree of perturbation in the ER, as suggested by formation of disulfide linked oligomers and reduced dynamic range, the platforms were differentially affected. See Figure 4.5e for a blot showing extensive oligomerization in the absence of a reducing agent. eZinCh-2 was the most strongly perturbed (dynamic range reduced from 2.06 to 1.47, increase in variability in FRET ratio as measured by RCV from 5.1% to 32.4%, and perturbation of ER morphology in 25% of cells), perhaps due to surface exposed cysteine residues. eCALWY-4 was also perturbed, but to a lesser extent (dynamic range reduced from 1.83 to 1.32, but no change in variability in FRET ratio as measured by RCV: 26.5% vs 22.8% in cytosol and ER, respectively). Finally, ZapCY1 was the least perturbed in the ER environment (dynamic range reduced from 2.62 to 2.55, variability in FRET ratio increased from

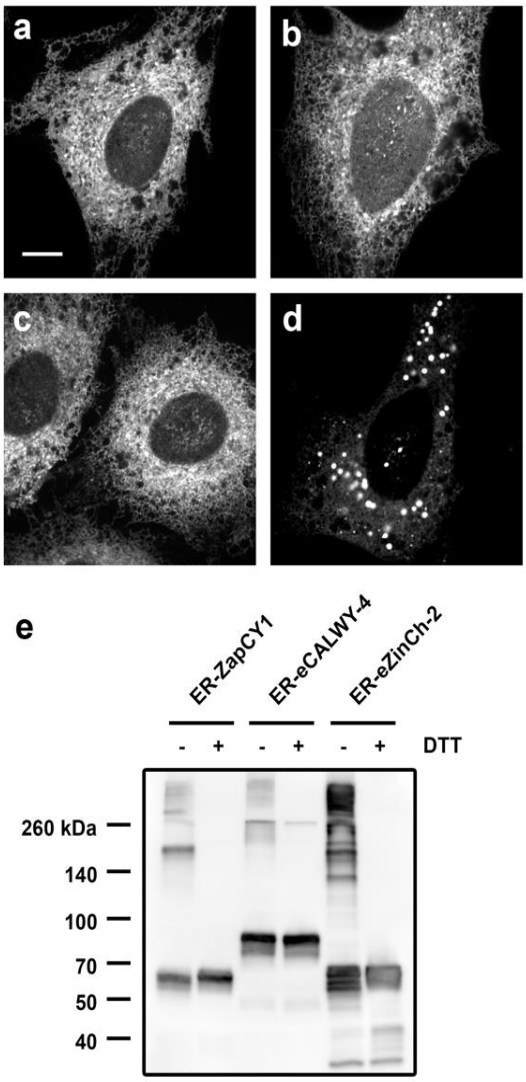


Figure 4.5. Measurement of localization to and aggregation in the ER. ER-ZapCY1 (a) and ER-eCALWY-4 (b) localize properly to the ER. Some cells expressing ER-eZinCH-2 have proper localization (c) but approximately 25% of cells exhibit bright puncta (d) regardless of signal sequence used (Figure S4). Western blot (e) of sensors in the ER under non-reducing and reducing conditions (denoted by – or + DTT) reveals that all sensors form DTT-sensitive oligomers. (credit: KPC)

9.3% to 11.1% in the cytosol versus ER, respectively). Despite some degree of perturbation in the ER environment, the estimated K_d values for each sensor closely matched *in vitro* measurements done alongside. Combined, these results suggest that eCALWY-4 and ZapCY1 are more suitable than eZinCh-2 to estimate relative amount of ER Zn^{2+}, and of the two sensor platforms ZapCY1 has a higher dynamic range (from Figure 4.2) and less evidence of perturbation.

4.5 Dynamic Response of ER and Cytosol Targeted Sensors and Sensor Variability

This platform also enabled measurement of sensor responses to added analyte in a short time window and identification of sub-populations of cells with sensors that are non-responsive sensor or that respond significantly differently than the average. Figure 4.4c and 4.4d show the pair-matched single cell response in the form of a histogram (FRET 2/ FRET 1), and the corresponding scattergram that illustrates the FRET change in individual cells (inset). All of the sensors gave rise to responsive populations, but the overall shape of the scattergrams varies from sensor to sensor and is not univariate as the binning of the histograms may suggest. This is most exaggerated in ER-eCALWY-4 (Figure 4.4c, bottom), in which the histogram appears broad and unimodal, but the scattergram shows additional sub-populations indicating variability in the kinetics of the response from cell to cell.

Comparison of scattergrams for ER-targeted versus cytosolic sensors revealed a greater degree of heterogeneity in responsiveness for all ER sensors. While some of this heterogeneity may derive from increased variability in the apo FRET state, some may also arise from variable Zn^{2+} uptake kinetics in different cells. It is clear the cytosolic sensors show a large response relative to the ER sensors. NES-eZinCh-2 is remarkable in the variability in the response, with a

tight apo population showing considerable kinetic variation across several FRET units in this time window. In contrast, ER-eZinCh-2 shows considerable FRET 1 variability, most of which responds in a similar magnitude. This is interesting as ER-eZinCh-2 cells showed a large increase in signal intensity relative to the ER versions of ZapCY1 and eCALWY-4 when under the same illumination conditions and transfection conditions. Plotting the signal intensity of each sensor in the donor and acceptor channel, ZinCh-2 shows a large intensity variation compared to the other two sensors. Figure 4.6a shows scattergrams of an independent screening of these sensors. These are plotted as a histogram, as shown in Figure 4.6b, and an arbitrary high threshold is set in the tail of the distribution at 2V. As shown in the histograms, both ER-ZapCY1 and ER-eCALWY-4 have ~18% of the cells acquired above this higher intensity gate. In contrast, ER-eZinCh-2 expands the entire range capable of detection using the current acquisition settings and 44% of cells acquired are above the high intensity gate. This is consistent with the higher intensity observed in the microscopy experiments and the bright puncta observed in a large percentage of cells of this sensor (visible in Figure 4.5d). The cytometer is insensitive to sensor localization and cannot differentiate between sensor that is properly localized in the ER, sensor that has not properly localized, and sensor that has aggregated to form bright puncta.

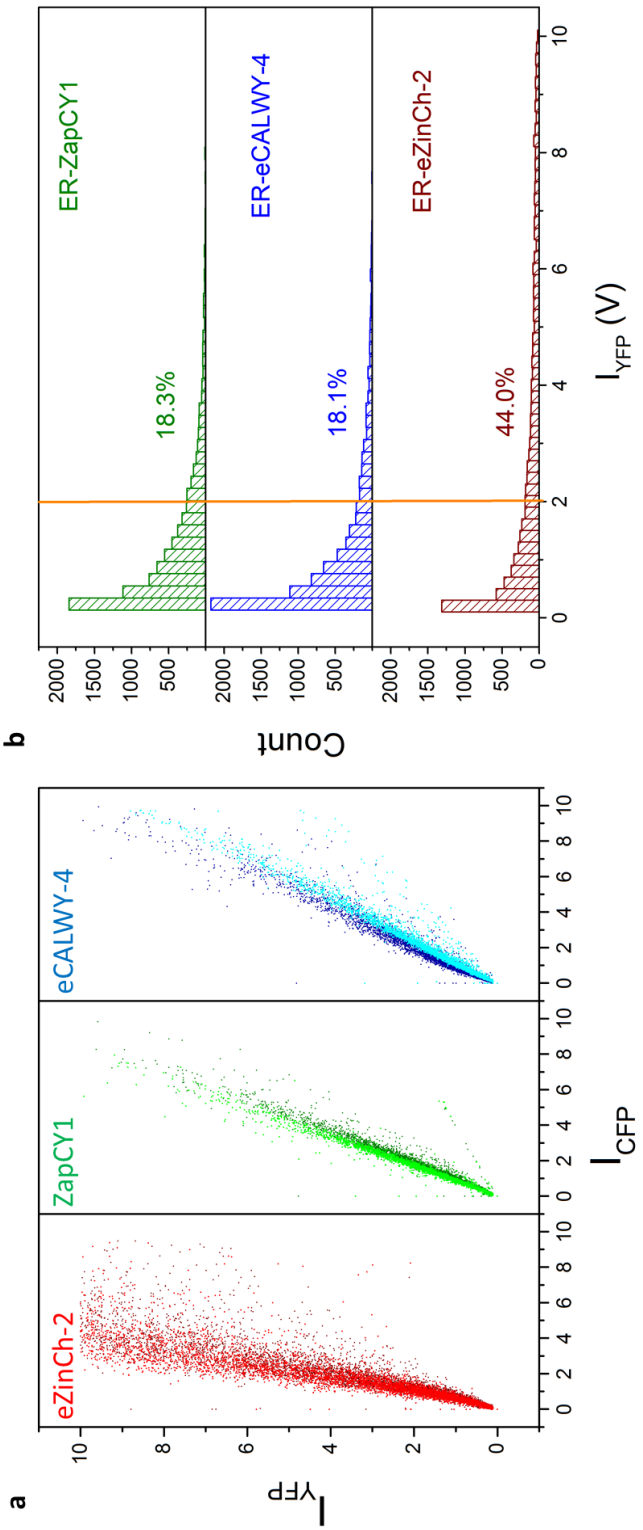


Figure 4.6. a) Intensity scatter plot for each sensor in the ER. b) Intensity histograms for the YFP channel showing the percentage of cells above 2 V. Data collected on the same day under identical illumination and gain settings. n = 7500 cells.

4.6 Generation of Linker Randomized Targeted Zn^{2+} Sensor Libraries

4.6.1 Library Rationale

Several issues were discovered in the sensors explored in the previous sections that complicated their use in the ER for free or labile Zn^{2+} quantification. First, there is a decrease in the dynamic range seen with the sensors when localized to the ER. Second, there is an increase in heterogeneity and a shift in the R_{min} of each sensor when move from the cytosol to the ER, potentially correlated to the decrease in dynamic range. Lastly, there is oxidation sensitivity in all three sensors investigated that decreases their reliability in the oxidative environment of the ER. It is increasingly clear that the generation of a large dynamic range cytosolic sensor does not guarantee large dynamic range within the ER, as is the case with eZinCh-2. Taking into account the need for an optimized ER sensor, methods to optimize these sensors for the complex environment of the ER will be discussed.

To address the issue of oxidation sensitivity, the sensors would need to be engineered to reduce the use of redox sensitive cysteine residues. Removal of the cysteine residues in each of the domains of the sensor, including the FPs used for FRET, needs consideration. Work has been done by the Snapp group to engineer redox insensitive variants of the FPs used frequently in the literature, in which outward facing cysteine residues in the beta-barrel of the FPs are mutated.[100] However, based on results from Western blot experiments done for the three sensors (Figure 4.5e), it does appear that the Zap family of sensors utilizing ECFP and mCitrine show signification aggregation due to barrel-barrel interactions in an oxidative environment. It is also likely that the decrease in dynamic range is due to the oxidation of the cysteines within the binding domain, both the metal coordination ligands and non-binding cysteines. Alteration of the

non-binding cysteines within the zinc-finger would likely have an effect on the folding of the zinc-finger structure and affect the dynamic range and binding affinity of the sensor. If the dynamic range is decreased, it would need to be restored by iteratively mutating out the cysteines for other residues or creating libraries in which those positions are randomized and sensor response is screened. Alternatively, molecular modeling using a program such as Rosetta could be done to optimize the folding of the zinc-finger at those positions held by cysteine residues.[101] The cysteines within the binding domain have been iteratively changed to histidines in several variants of the ZapCY sensors.[41] Each mutation that was done to change the wild-type Cys_2His_2 pocket (both fingers) led to a decrease in binding affinity and a decrease in dynamic range. Cysteine residues help maintain Zn^{2+} specificity and tight binding constants associated with the zinc finger.[102] This is an effective method for creating an array of sensors with varying binding constants, but makes it difficult to eliminate cysteine residues entirely without further optimization of the dynamic range.

Improving the dynamic range of the sensors requires an alteration of the R_{max} value, the R_{min} value, or both. The shift in R_{min} for the ZapCY1 sensor indicates that modification of the dynamic range of a sensor in the ER may be achieved by lowering the R_{min}. In order to modify the FRET values of either the bound or unbound state, the parameters that govern the RET efficiency need to be modified. Recalling Equation 1.1, the two parameters that are variable for a given FRET pair is the distance (R) and relative orientation (κ^2) of the donor and acceptor chromophores. Libraries in the FRET sensor field have been generated using a number of approaches to achieve increased dynamic range. One method for altering the orientation has been to circularly permute one or both of the FPs in the construct. Circular permutation is the changing of the positions of the N and C termini within the amino acid sequence of the protein.

Circular permutation has been successfully done for fluorescent proteins for the use in sensors and has generated improved variants due to the altered donor-acceptor orientation in the bound and unbound states.[103,5,104,32,10] Circularly permuted versions of the Zap sensors (with cpVenus at position 173) have been created, but have not yet been successfully expressed when localized to the ER.* This presents a desirable path for optimization, but will require further work to implement in all localizations.

Modification of the distance and orientation leading toward increased dynamic range has also been achieved by modifying the linker and binding domain within FRET sensors.[50,105–107] This strategy varies based on the structure of the binding domain and mechanism of sensor response. In the parallel field of Ca^{2+} binding biosensors, significant work has been done to yield high dynamic range by linker modification. One example is the optimization of TN-XXL, a Ca^{2+} FRET sensor developed by the Griesbeck group.[49] In this work, short linkers (1-4 residues) flanking both sides of the binding domain were fully randomized to alter the orientation in tandem with circular permutation of the acceptor, Citrine. This method is attractive for the Zap family Zn^{2+} sensors given the similarity between the constructs (CFP-metal binding domain-YFP). It is not apparent if modification of the orientation or the distance is more important to increase sensor response in the complex, potentially crowded environment of the ER. Therefore, it will be important to assess libraries that both increase the distance between the donor-acceptor pair, as well as libraries targeting an orientational change between donor and acceptor.

* Personal communication with Prof. Amy Palmer.

4.6.2 Library Design and Selection Process

Three libraries were devised to generate optimized Zn^{2+} sensors using the Zap platform. The libraries are designed with consideration of the cell-throughput restrictions imposed by the microfluidic sorter. Given a sorting rate of the 2-3 cells/s for mammalian cells, it is reasonable to sort on the order of ~10,000 cells per hour. The size of the library is then set by the desired coverage of the library. In the case that a single library member should be screened multiple times, then libraries must be kept to a size of several thousand (10^3-10^4). This corresponds to a randomization of 2-3 amino acids if all 20 amino acids are included. The libraries generated for this purpose consist of biased codons that decrease the variability in the amino acid pool. One codon was chosen to increase the rate of charged and hydrogen-bond forming amino acids in order to enhance amino acid interaction and increase linker rigidity. This is done by incorporating a VVC codon in the constructed primers which limit the possible nucleic acids at each position (V = A/G/C). This codon restriction limits the possible amino acids to Ala/Asp/Gly/His/Asn/Pro/Arg/Ser/Thr. Two libraries were created using this codon as a basis. The first contains a mixture of lengths in which 1 or 2 residues have been added on either side of the zinc binding domain for sensor constructs of the form ECFP-Linker-ZBD-Linker-Citrine. ECFP has been truncated 11 residues at the C-terminus to make the attachment point at a rigid portion of the FP as indicated by crystallographic structures.[108] This results in the possible combinations of 1+1, 1+2, 2+1 or 2+2. This library was named VVC1-2 and contains 7371 library members. This library could reach 3-5 fold coverage in a few hours. Another library was generated in which the VVC repeats were included in a 3+3 combination, resulting in a library (VVC3) with 531,441 members. This library cannot be fully covered by the microfluidic sorter, but is interesting in whether increasing the linker length has any effect on the sensor. A third

library was devised that incorporated the YCC codon, which limits the residues to only Pro/Ser. Proline is an amino acid with a rigid, cyclic side chain the locks the peptide into fixed angles. Chains of prolines form a very stable polyproline helix, (e.g. the secondary structure of collagen). This codon was implemented in a combinatorial fashion up to 4 amino acids, generating a library (named Pro/Ser) with 276 members.

The library workflow and selection process is shown in Figure 4.7. The steps were developed to accommodate the lack of cell viability upon Zn^{2+}/pyrithione exposure. No cell enrichment through post-sort growth is possible, therefore the workflow relies on genomic DNA (gDNA) extraction, amplification, and identification. The process begins with library design as laid out in the previous paragraph. Once cloning of the sensor library into a viral vector is completed resulting in a pool of library members incorporated in a viral vector, then plasmids are virally transduced to induce expression of the sensor library in the target cell line (HeLa-S3). Viral transduction was chosen to control the multiplicity of plasmids introduced to the cells, which follow Poisson statistics.[87] It is undesirable for a single cell to express multiple sensors, so only one plasmid should be incorporated in each cell. Chemical transfection techniques are inferior to viral techniques for control of plasmid multiplicity. Once an expressive population of cells has been selected (through antibiotic selection and/or FACS), the cells are simultaneously screened on the microscope for localization verification and screened on the microfluidic platform. If interesting variants are observed, the library is re-run on the microfluidic and sorted for high response. The collected cells are immediately processed to extract their gDNA, which is then PCR amplified and reintroduced into the viral vector for a second cycle. The process can repeat until one or more improved sensors are isolated. Sequencing can occur at any of these steps to ensure losses do not occur.

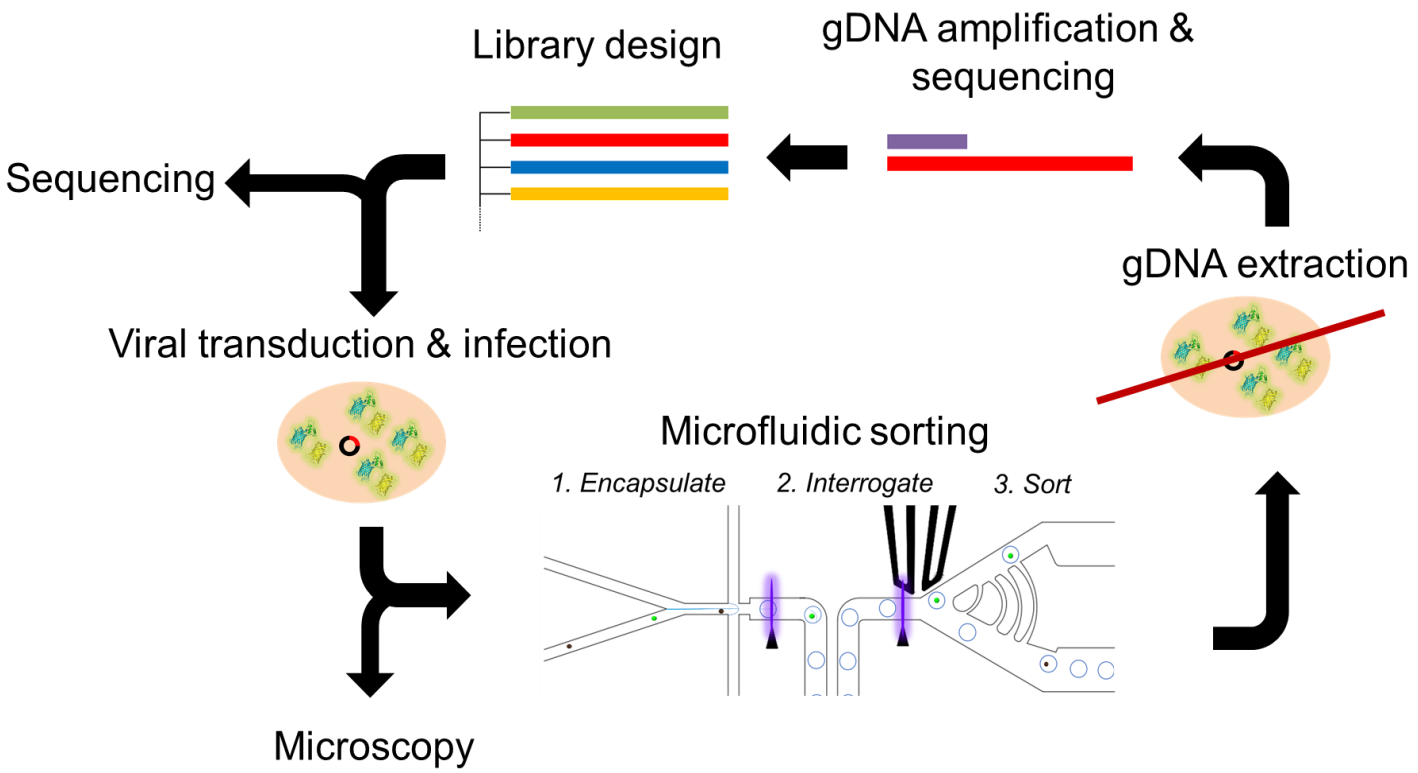


Figure 4.7. Workflow for library generation and optimization of a biosensor library based on gDNA amplification rather than cell enrichment. The process begins with library design, cloning, and verification before expression in cells. Each step of this cycle has points for troubleshooting.

4.6.2 Initial Library Screening and Platform Iteration

The parent of each of the three libraries was initially chosen to be ZapCY2, a Zap family Zn^{2+} sensor consisting of truncated ECFP and mCitrine with a modified Cys_1His_3 binding pocket with K_d = 100 nM. A looser binding sensor was chosen, as a tight binding sensor (ZapCY1, K_d = 4 pM) already exists for the ER. A lower affinity sensor with high dynamic range is greatly needed to help solve the controversy with respect to Zn^{2+} levels in the ER. Transient transfection (TransIT-LT1) of this sensor in the ER of HeLa-S3 cells was done and the resulting expressive cell population was screened in the microfluidic to verify contextual response. Figure 4.8 shows the resulting FRET 1 and 2 histograms after a time delay of 6.2 seconds. The response is small (~1.1), but a FRET population shift is resolved.

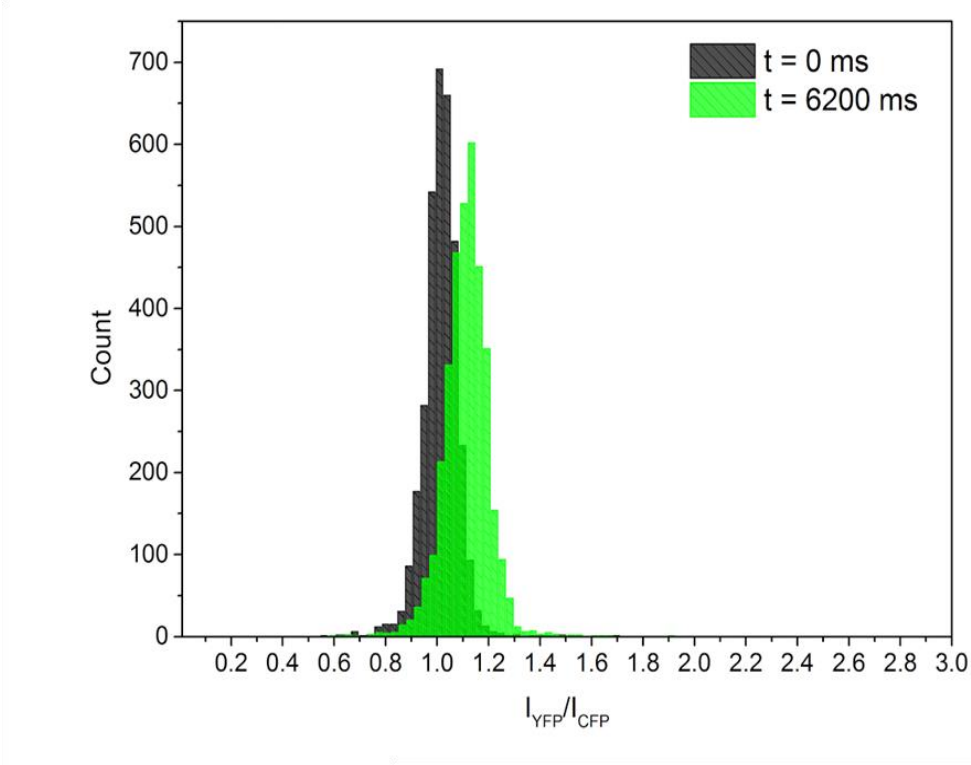


Figure 4.8. FRET histogram of ER-ZapCY2 expressing HeLa-S3 cells. Cells were transiently transfected using TransIT-LT1 in a PiggyBAC vector. Δt = 6.2 s. n = 3500 cells.

The parent sensor was initially cloned into the retroviral vector pCLNCX (Novus Bio) for viral transduction of HeLa-S3 cells. After antibiotic selection and recovery, the cells were again screened on the microfluidic. Figure 4.9 shows the FRET 1 histogram from this construct. It is clear a large amount of heterogeneity was introduced during the viral steps that was not present in the transient expression. A low FRET population appears that is consistent with the presence of multiple populations. These cells were run on a FACS to isolate cells with both CFP and YFP, however, this did not eliminate a majority population that was unresponsive to Zn^{2+}/pyrithione (data not shown). The cause of these extra populations is likely recombination during viral replication due to the high sequence similarity between ECFP and mCitrine. Figure 4.10 is a comparison of the aligned ECFP and Citrine sequences. Indeed, many FPs derived from GFP show sequence homology, which makes cloning difficult when multiple FPs are involved in a cloning step.

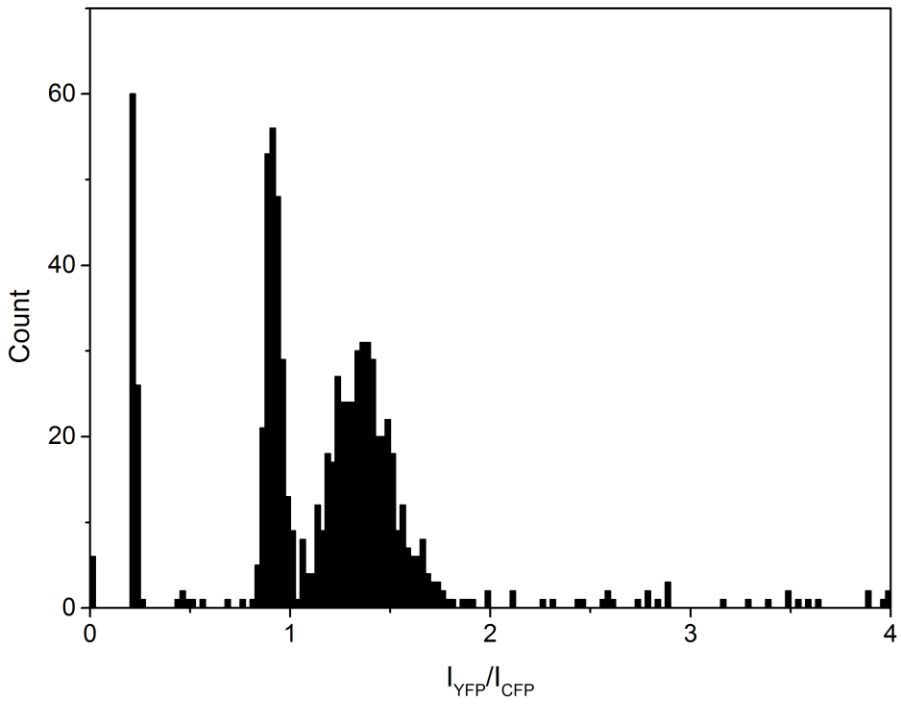


Figure 4.9. FRET Histogram of HeLa-S3 cells expressing ER-ZapCY2 in pCLNCX. Cells were virally transduced and selected using puromycin. n = 1050 cells.

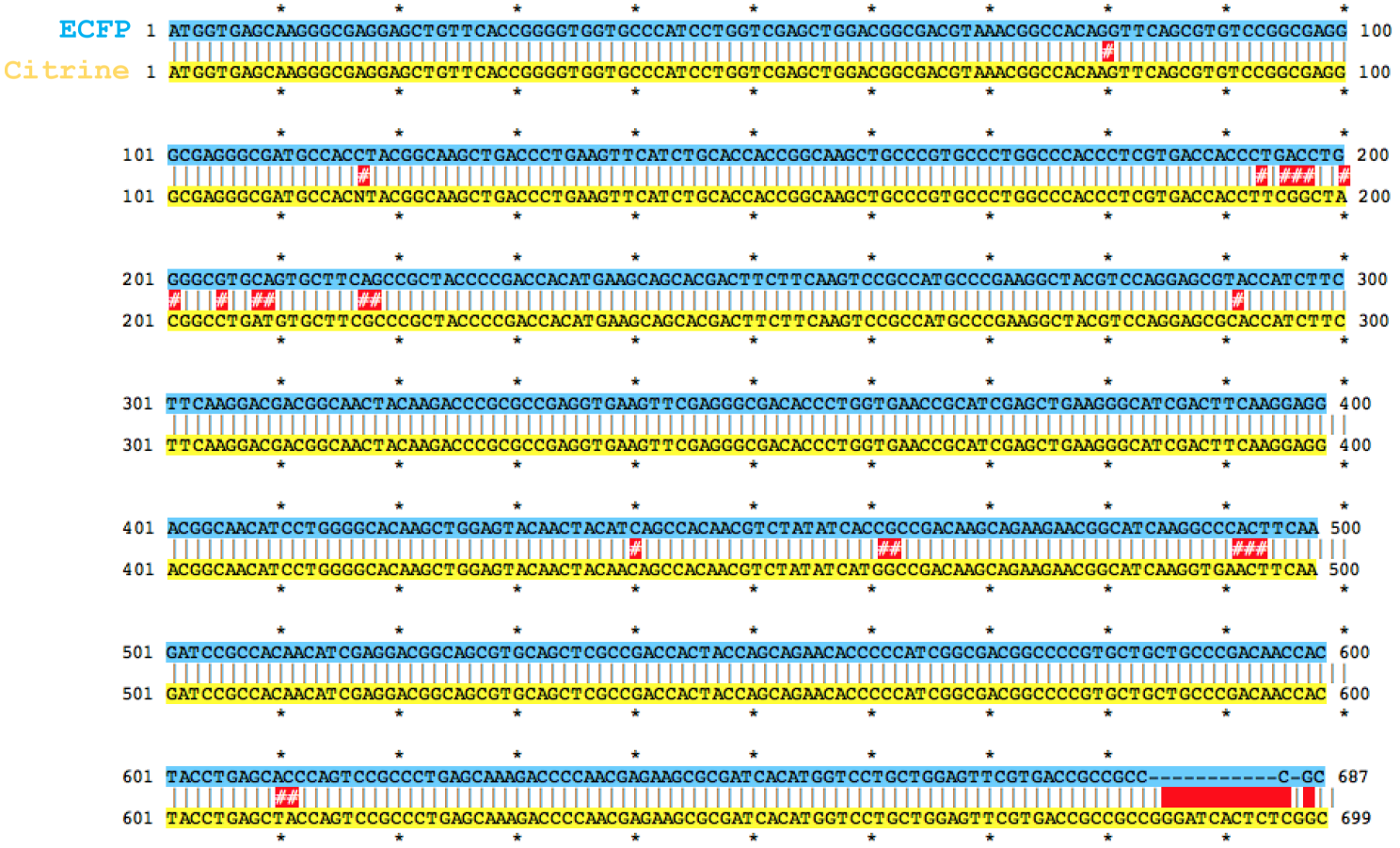


Figure 4.10. Nucleic acid sequence of ECFP aligned with Citrine. Red (#) denote disparities in the sequence. Differences are concentrated in the region around the chromophore. The region leading up to the C-terminus is nearly identical, with only 2 nucleic acids difference, leading to primer mismatch and recombination.

Reduction of the recombination was achieved by Molly Carpenter by codon diverging the two FPs. This resulted in a codon diverged ECFP, a codon diverged Citrine and a ZBD (Zap2) that was optimized to the most prevalent human codons for each amino acid. The resulting construct, coined OptiZap, is then $ECFP_{trunc,diverged}$-$Zap2_{optimized}$-$Citrine_{diverged}$. This construct was cloned into the lentiviral vector pLVX (Clontech). The change in viral vector was done to increase transduction efficiency. After antibiotic selection and recovery, the cells were screened on the microfluidic. As shown in the resulting data (Figure 4.11), this cell line shows a unimodal responsive population. All of the libraries discussed previously were recreated using OptiZap as the parent construct. Library creation was verified using commercial sequencing on ~10 samples and verifying the absence or low presence of the parent sequence in the ZBD.

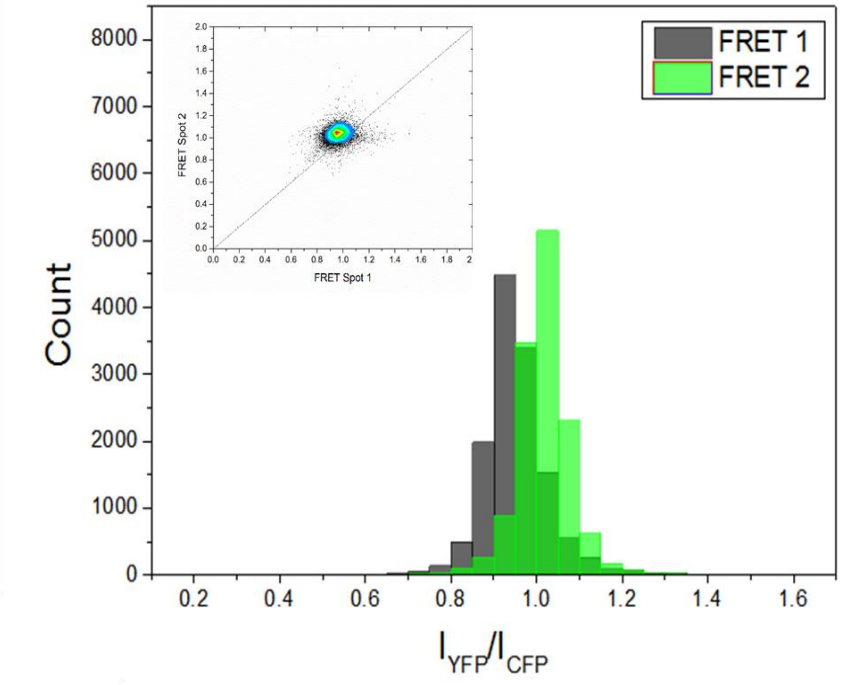


Figure 4.11. FRET histograms for ER-Optizap in pLVX. Cells were virally transduced and selected with puromycin. (Inset) Pairmatched scattergram. n =

4.7 Microfluidic Screening and Initial Sorting of Sensor Libraries

4.7.1 Pro/Ser Library

The pLVX|ER-OptiZap derived Pro/Ser library was the first screened for Zn^{2+} response. The results of this screen are shown in Figure 4.12. Statistics for this screen are compiled in Table 4.2. There is apparent heterogeneity in the scatterplot (Figure 4.12a), with very low FRET, unresponsive cells. There is no apparent shift relative to OptiZap in the large population dominating a ~1.1 fold response with 33,000 cells screen. The library created should be sampled over 10 times per clone, so it is possible the events outside of the main population are instrument noise or improved sensor variants.

4.7.2 VVC1-2 Library

The VVC1-2 library was screened in conjunction with OptiZap on the same day to make a direct comparison and assess if diversity was introduced in the library. The results of this screen are shown in Figure 4.13. Statistics for this screen are compiled in Table 4.2. It is evident based on the FRET change histogram (Figure 4.13c) that there is not an overall increase in response due to the linker modifications on the microfluidic platform. One interesting observation is found in the FRET histograms (Figure 4.13b). The median FRET 1 (R_{min}) distribution for VVC1-2 is decreased relative to OptiZap by 0.05 FRET units. The reduction in FRET 1 can possibly be explained by the lengthening of the linkers, consistent with an increase in distance, therefore lowering the FRET efficiency of the construct. However, it is not clear from the data that diversity has been introduced in this library that is resolvable by the microfluidic platform.

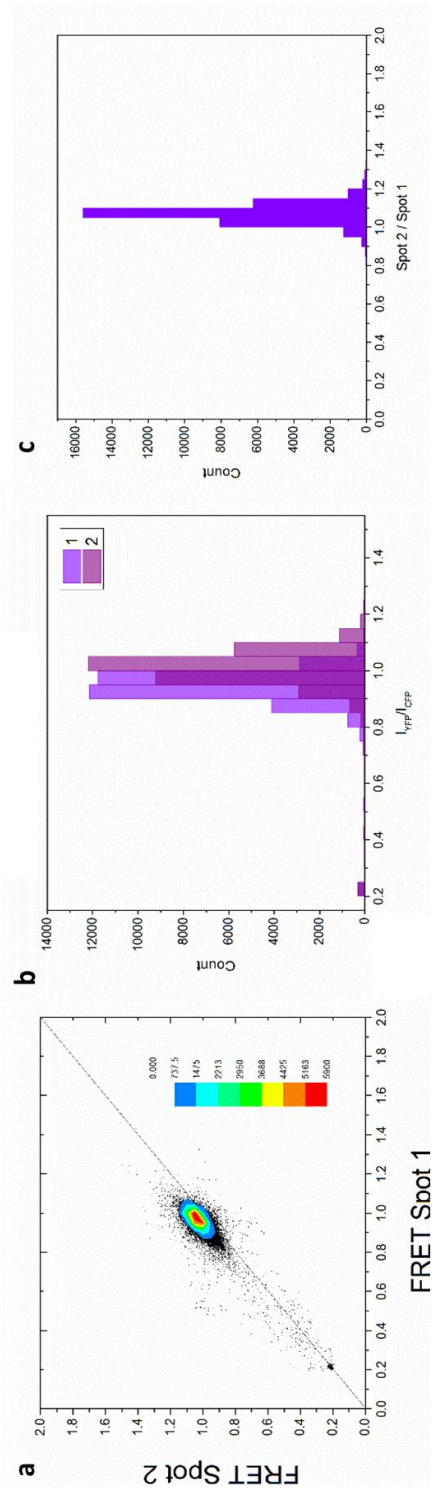


Figure 4.12. HeLa-S3 cells expressing Pro/Ser library. (a) Pairmatched scattergram. (b) FRET histograms corresponding to Spot 1 and Spot 2. (c) FRET Change histogram. $\Delta t = 8.1$ s. n = 33,000 cells.

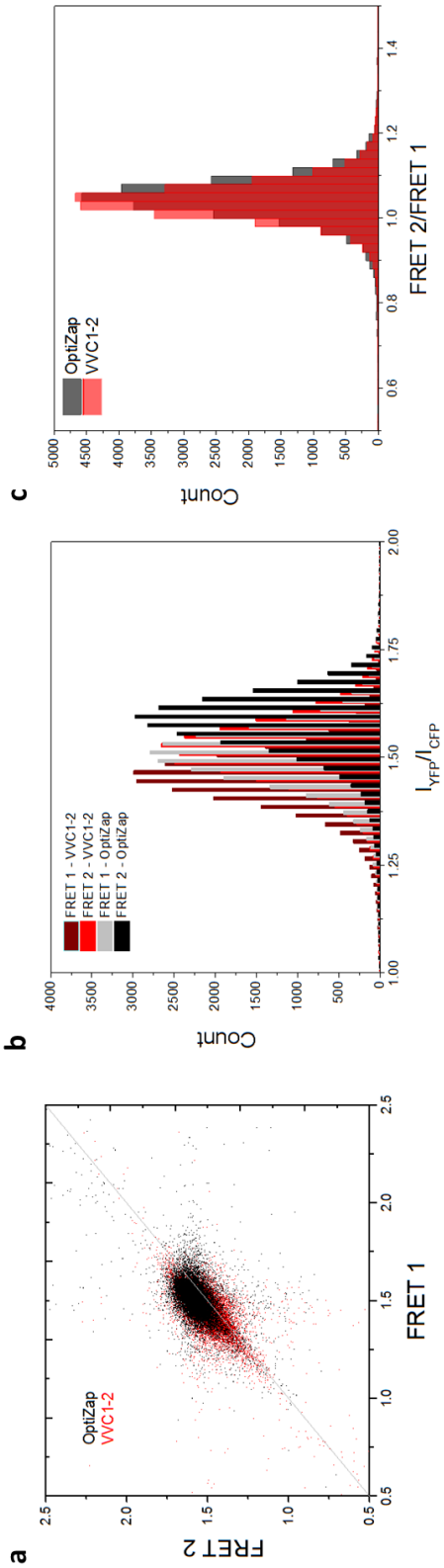


Figure 4.13. HeLa-S3 cells expressing VVC1-2 library. (a) Pairmatched scattergram. (b) FRET histograms corresponding to Spot 1 and Spot 2. Gaps included to increase visibility of overlap. (c) FRET Change histogram. $\Delta t = 9$ s. n = 29,000 cells.

4.7.3 VVC3 Library

The VVC3 library was also run on the same day as the parent, Optizap, in order to make a direct comparison. This library has a size much larger than the microfluidic platform is capable of covering in a reasonable timespan, but was generated to check for trends in the pool resulting from 6 additional amino acids in the linker. The results of this screen are shown in Figure 4.14. Statistics for this screen are compiled in Table 4.2. As seen in the scatter plot (Figure 4.14a), VVC3 contains extra events at low FRET, suggesting recombination is present in this library. No significant increase in FRET change is apparent. There is a reduction in the median FRET 1 (R_{min}) by 0.09. This is larger than the shift seen in VVC1-2, potentially consistent with the addition of 2 more residues in the linker, though it should be noted that the magnitude of the shift is small. While there are more spurious cell events in this library, there is also more recombination evident by the small low FRET population. Again, it is not clear from this data that resolvable diversity has been introduced, despite a small increase in the RCV of the individual FRET distributions relative to OptiZap.

4.7.4 VVC1-2 Sort and Troubleshooting

A sort on the VVC1-2 library (named VVC1-2R1) was conducted in order to step through the entire cycle of library processing shown in Figure 4.9. The sorting experiment scatter data is shown in Figure 4.15a with gates overlaid. Statistics for this distribution are found in Table 4.2. The FRET change gate was set to a 1.2 fold change and the individual FRET gates were opened up to include most cells. The 450 sorted cells were immediately lysed in gDNA extraction buffer and incubated with Proteinase K overnight. The resulting gDNA was PCR

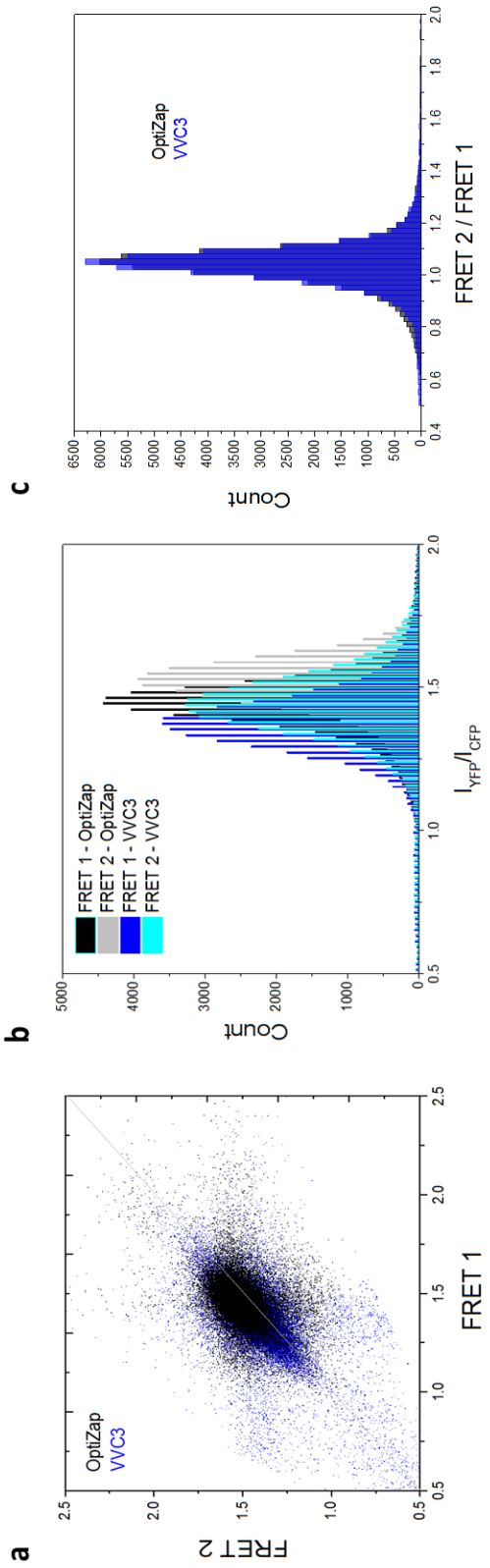


Figure 4.14. HeLa-S3 cells expressing VVC3 library. (a) Pairmatched scattergram. (b) FRET histograms corresponding to Spot 1 and Spot 2. Gaps included to increase visibility of overlap. (c) FRET Change histogram. $\Delta t = 10$ s. n = 45,000 cells.

Name	Mean	SD	CV	Median	IQR	RCV	RCV(%)
FRET 1 - Pro/Ser	0.93	0.098	0.105	0.94	0.061	0.048	4.8
FRET 2 - Pro/Ser	1.00	0.107	0.107	1.01	0.069	0.052	5.2
FRET 2 / FRET 1 - Pro/Ser	1.07	0.057	0.054	1.07	0.053	0.037	3.7
FRET 1 - OptiZap	1.51	0.135	0.090	1.51	0.095	0.047	4.7
FRET 2 - OptiZap	1.58	0.123	0.078	1.58	0.091	0.043	4.3
FRET 2 / FRET 1 - OptiZap	1.05	0.070	0.067	1.05	0.058	0.042	4.2
FRET 1 - VVC1-2	1.45	0.112	0.077	1.46	0.089	0.046	4.6
FRET 2 - VVC1-2	1.51	0.128	0.085	1.52	0.101	0.050	5.0
FRET 2 / FRET 1 - VVC1-2	1.04	0.080	0.077	1.04	0.054	0.039	3.9
FRET 1 - OptiZap	1.46	0.196	0.134	1.46	0.112	0.058	5.8
FRET 2 - OptiZap	1.51	0.187	0.124	1.52	0.128	0.063	6.3
FRET 2 / FRET 1 - OptiZap	1.04	0.096	0.092	1.04	0.085	0.061	6.1
FRET 1 - VVC3	1.35	0.220	0.163	1.37	0.140	0.077	7.7
FRET 2 - VVC3	1.40	0.226	0.161	1.43	0.153	0.080	8.0
FRET 2 / FRET 1 - VVC3	1.04	0.121	0.116	1.04	0.084	0.060	6.0
FRET 1 - VVC1-2R1	0.94	0.132	0.141	0.94	0.065	0.052	5.2
FRET 2 - VVC1-2R1	1.00	0.127	0.127	1.00	0.068	0.051	5.1
FRET 2 / FRET 1 - VVC1-2R1	1.07	0.066	0.061	1.06	0.057	0.040	4.0

Table 4.2. Compilation of population statistics from library screening experiments. SD = Standard Deviation. CV = Coefficient of Variation (SD/mean). IQR = Interquartile Range. RCV = Robust Coefficient of Variation (IQR/median).

amplified and reintroduced to the viral vector for transduction in a fresh plate of HeLa-S3 cells. After selection and recovery, the cells were re-screened on the microfluidic platform. A comparison of this sample and OptiZap are shown in Figure 4.15b. No shift in the FRET response of the population is evident. The explanations for the lack of shift in the responding population include a lack of coverage or diversity in the original library, the inability for the

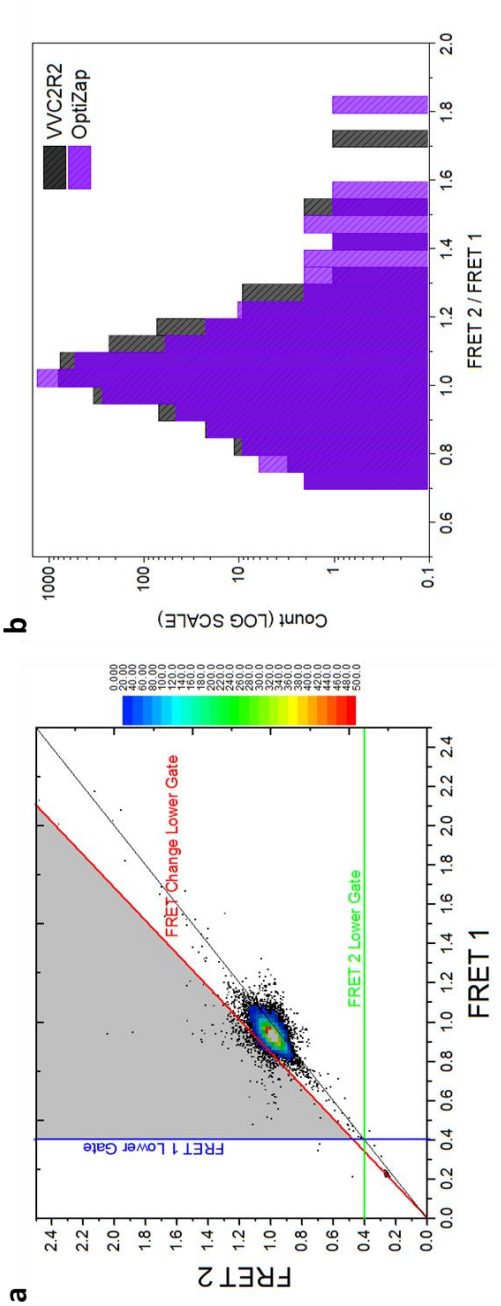


Figure 4.15. (a) Scattergram for VVC1-2R1 sort. Gates: F1 = 0.4, F2 = 0.4, F2/F1 = 1.2. Δt = 7.4 s. n = 17500 cells. Cells sorted = 450. (b) FRET change histogram on a log scale for the second round of VVC1-2 after sorting. Δt = 8.2 s. n = 2500 cells.

microfluidic to resolve the response of these targeted libraries, and the contamination/modification of the library during the gDNA workup and amplification.

Possible issues resulting from the amplification steps was explored through a control experiment on cells harvested directly from a plate. The gDNA extraction protocol was conducted on the parent (OptiZap), the Pro/Ser library, and the VVC1-2 library with decreasing cell numbers. The protocol was also conducted cell-free as a 'mock' experiment. The resulting products were split and half was subjected to PCR amplification of the ZBD. DNA was run on agarose gels, displayed in Figure 4.16 at two different contrast levels. Figure 4.16a shows the resulting gDNA bands with no bands visible in the mock. Figure 4.16b show the resulting bands after PCR amplification at the size expected for the ZBD. The mock experiment shows a band even in the absence of cells, suggesting possible contamination. Sequencing on this band showed the presence of the parent across several sequencing attempts. Figure 4.16c shows the ability of the PCR step to amplify DNA at a variety of cell counts. Bands are visible above 100 cells, but readily detected above 1000 cells.

Problems occurring due to the lack of library coverage are not readily apparent without the use of high throughput sequencing, but sequencing of > 10 samples suggests the linker modifications are present. It is difficult to decouple lack of diversity with the inability of the microfluidic to resolve the library response on this timescale for the ER sensors. This problem can be disentangled with the creation of a cytosol localized sensor library using the same linkers.

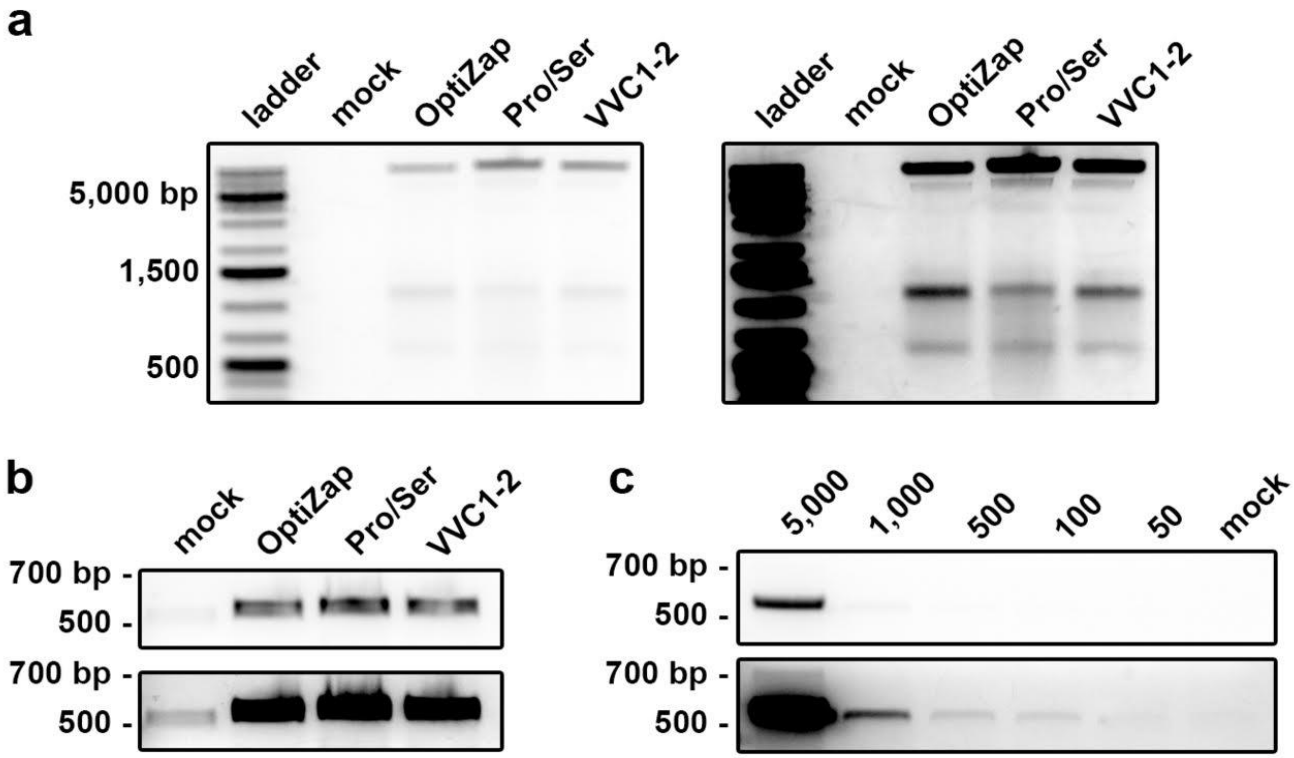


Figure 4.16. Genomic DNA extraction (**a**) and ZBD amplification (**b-c**) from OptiZap and library cell lines. Genomic DNA was extracted from virally-transduced HeLa S3 cells stably expressing the libraries and the linker-ZBD-linker regions were amplified by PCR. Genomic DNA from the cell lines (**a**) is a high-running band with several smaller bands and smears when incubated with a fluorescent DNA stain. Contrast is adjusted in the right panel to highlight the absence of signal in the mock (no cells) lane for the gDNA extraction. (**b**) PCR amplification of the linker-ZBD-linker region from mock, OptiZap, Pro/Ser, and VVC1-2 gDNA. Contrast is adjusted in the lower panel to highlight the contamination band present in the mock PCR. (**c**) PCR amplification of the linker-ZBD-linker region from a dilution of VVC1-2 cells. Bands from PCR products are readily detectable from reactions using gDNA from > 1,000 cells. Contrast is adjusted in the lower panel to highlight the bands from reactions using 100 and 500 cells as template, as well as the fainter bands from reactions using gDNA from 50 or zero cells as template. (credit: KPC)

4.8 Conclusions and Future Directions

In this chapter, the microfluidic platform was used to assess the population heterogeneity of three unique Zn^{2+} FRET sensors. It was determined that all three sensors were perturbed when localized in the ER relative to the cytosol. This resulted in a shift and sometimes spread in the minimum FRET state and a lowering of the dynamic range. Additionally, heterogeneity was observed in the response of these sensors, whether cytosol or ER targeted. All of these observations indicate a need for sensors that are tailored to the environment they are to be used.

The initial steps in creating an optimized sensor were laid out and 3 linker libraries were presented. Diversity in each of these libraries was not clearly identified using the microfluidic platform. The most beneficial experiments to be conducted next are those that relocate the library to the cytosol. This will bypass any kinetic limitation with respect to the microfluidic platform and assess if the linker libraries as devised are capable of producing diversity and, ideally, improved sensors. If diversity is established and the sorter is unable to kinetically resolve the response of the ER targeted library, it may be that a different library is required or the microfluidic platform will need to be modified to accommodate the timescales necessary for sensor response. However, this will require an overhaul of the microfluidic devices required and necessitate a decrease in throughput to reach these timescales.

Beyond the parameters required to resolve an ER sensor response, the microfluidic platform is already established to be useful in the measurement of cytosolic sensors. The instrument is readily adaptable to other optical windows. There is a great need for high dynamic range Zn^{2+} sensors that utilize a GFP-RFP FRET pair. Generation of higher dynamic range sensors in the cytosol could be accomplished with the current library designs if they are proven to modify the sensor response in the CFP/YFP sensor platform.

Chapter 5

Time-Resolved Photophysical Characterization of Zn^{2+} FRET Sensors

5.1 Time-Resolved Fluorescence of Genetically-Encoded Sensors

5.1.1 Fluorescence Lifetime Measurements

Time-resolved fluorescence spectroscopy provides a wealth of information unattainable through steady-state fluorescence measurements. It gives information on the excited state dynamics of a fluorophore, specifically the factors affecting the fluorescence lifetimes of the excited states. Factors range from the solvation dynamics of the excited chromophore to excited state reactions to energy transfer processes.

There are two methods for measuring fluorescence lifetimes, frequency-domain and the time-domain. Frequency-domain measurements are also sometimes referred to as phase-modulation measurements because they are performed by amplitude modulating an excitation source with an oscillation period on the order of the lifetime to be observed and measuring the phase delay resulting from the finite lag time of fluorescence after excitation. The tangent of that phase delay is proportional to the single exponential lifetime and modulation frequency of the excitation.[109] While simple in setup, frequency-domain measurements are difficult to analyze

when a fluorophore shows a multi-exponential decay: measurements at multiple frequencies are required to precisely determine the lifetime components.

Time-domain measurements, also referred to as pulse fluorometry, require a pulsed excitation source with pulse durations on a picosecond timescale. In the most common form of this method, excitation intensity and emission intensity are attenuated to ensure that less than one photon is detected per pulse. Detected photons are binned according to their arrival time relative to the excitation pulse. This method is called time-correlated single-photon counting (TCSPC). After sufficient photon counts, the resulting histogram of counts is fit to a model, generally exponential, and the fluorescence lifetime (τ_i) components are extracted. Measured intensity traces typically fit the form[110]:

$$I(t) = \sum_i \alpha_i \exp\left(-\frac{t}{\tau_i}\right) \otimes IRF \tag{5.1}$$

where α_i is the ith amplitude of the fitted exponential. The measurement time is generally longer compared to the frequency-domain method, since measurement time is limited by the low rate of photon arrival, but time-domain measurements are more robust in multi-exponential decay determination without the need for multiple measurements (i.e. multiple frequencies needed for frequency domain). Given the finite transit time for signals in the TCSPC, which is generally limited by the detector response, sub-nanosecond lifetime components are difficult to determine accurately in the absence of a measured instrument response function (IRF). The IRF is used to de-convolute the time response from the measured photon counts.[110]

5.1.2 Fluorescence Anisotropy

Isotropic emission lifetime measurements by TCSPC are generally taken with linearly polarized excitation and an emission polarizer set to 54.7° (the "magic angle") relative to the excitation polarization to avoid effects resulting from molecular rotation after photoselection, which would give rise to a decay more complex than from the fluorescence lifetimes alone. However, the polarization of the emission relative to excitation contains significantly more information when used in conjunction with the lifetime measurements. Fluorescence anisotropy, defined as:

$$r(t) = \frac{I_{VV}(t) - GI_{VH}(t)}{I_{VV}(t) + 2GI_{VH}(t)} \quad (5.2)$$

where I_{VV} is the emission intensity measured with (traditionally) vertically polarized excitation through an emission polarizer aligned with the excitation. I_{VH} is the intensity of emission measured with the polarizer set 90° off vertical. G is the G-factor which corrects for polarization bias in the detector.[110] Fluorescence anisotropy provides a concentration-independent measurement of any process that causes a rotation of the transition dipole moment vector during the time between the absorption of a photon and the subsequent emission of a photon. The probability of photon absorption is proportional to $\cos^2\psi$, where ψ is the angle from the axis defined by the linearly polarized excitation. The result is an angular distribution of excited fluorophores. This phenomenon is called photoselection and limits the theoretical maximum anisotropy value for a one-photon excitation to 0.4.

Time-resolved fluorescence anisotropy (TRFA) can be measured using a TCSPC setup by rotating the excitation and emission polarizers. In TRFA experiments, parallel and perpendicular components of the emission are measured. The intensities of these two components are given by:

$$I_{VV}(t) = \frac{1}{3}\sum_i \alpha_i \exp(-\frac{t}{\tau_i})\left[1 + 2\sum_j r(0)_j e^{-t/\varphi j}\right] \quad (5.3)$$

$$I_{VH}(t) = \frac{1}{3}\sum_i \alpha_i \exp(-\frac{t}{\tau_i})\left[1 - \sum_j r(0)_j e^{-t/\varphi j}\right] \quad (5.4)$$

where φ is the correlation time corresponding to the jth component of the fluorescence depolarization. The most common cause of depolarization is molecular motion, i.e. rotations that occur during the lifetime of a fluorophore. The timescale and amplitude of the anisotropy decay gives information on the environment of the molecule and the effect of that environment on the excited state of that molecule.

Another process which can result in fluorescence depolarization is FRET. For a suitable donor-acceptor pair (discussed in Chapter 1), radiationless energy transfer can occur between the excited singlet states of two molecules upon excitation of the donor. A Jablonski schematic of the possible processes following an absorption event is shown in Figure 5.1a. Contributions to the fluorescence depolarization of a system undergoing FRET include rotation of the donor, the rotation of the acceptor, and a change in acceptor emission polarization relative to the polarization used to excite the donor resulting from energy transfer. Given the initial orientation of the donor, emission from the acceptor will occur at a different angle after energy transfer occurs unless the donor and acceptor transition dipole moments are perfectly aligned. can provide information on the relative orientations of the two chromophores.[111,112] For a molecular picture of energy transfer, the relevant vectors and angles between the pair of chromophores are shown in Figure 5.1b. For a given FRET pair, the rate of energy transfer is proportional to the donor-acceptor distance and the relative orientation between their transition dipole moments. The orientation factor, κ^2, is defined relative to Fig. 5.1b in terms of the angles θ_T, θ_D, and θ_A such that

$$\kappa^2 = (\cos\theta_T - 3\cos\theta_D \cos\theta_A)^2 \quad (5.5)$$

Time-resolved fluorescence anisotropy can be used to determine the average transfer angle, $\theta_{T,,}$ and subsequently place limits on the value of κ^2, allowing a more precise calculation of R (distance between chromophores, equation 1.6).[113]

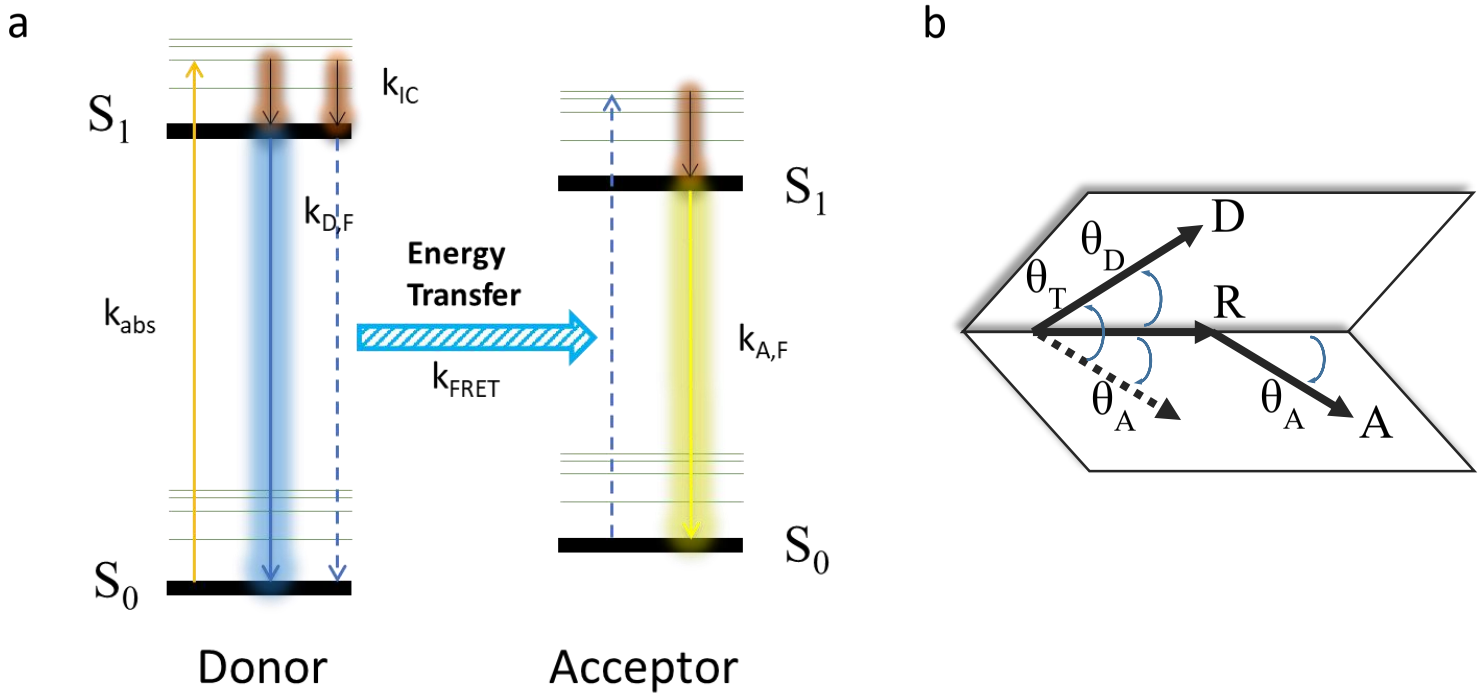


Figure 5.1. a) Jablonksi diagram for a donor-acceptor pair undergoing FRET between singlet excited states. The energy transfer process must be competitive with the fluorescence rate of the donor. k_{abs} is the rate of absorption ($1/k \approx$ attoseconds), k_{IC} is the rate of internal conversion (fs-ps), $k_{D,F}$ is the rate of donor fluorescence (ns), k_{FRET} is the rate of energy transfer (ps-ns), $k_{A,F}$ is the rate of acceptor fluorescence (ns). b) Schematic representation of the angles used in the determination of κ^2. D and A are the transition dipole moments (TDM) of the donor and acceptor, respectively. R is the distance between the TDMs. θ_T, θ_D, and θ_A are the angles between A and D, D and R, and A and R, respectively.

5.1.3 Fluorescent Proteins as Anisotropy Probes

Fluorescent proteins are uniquely suited as probes using anisotropy. The chromophore in a fluorescent protein is rigidly fixed within the barrel of the protein and thus rotates with the protein as a whole. The ~27 kDa (for GFP) protein rotates much slower than small molecule fluorophores. The rotational correlation times in low viscosity buffers for FPs are in the range of 15-20 ns, which is much longer than their lifetime (1-4 ns).[112,114] For example, mVenus has a fluorescence lifetime of ~3 ns, and has a steady-state anisotropy of ~0.33 across its emission bandwidth (470 nm excitation).[115] Fluorescein dianion has a lifetime of ~4 ns and a steady-state anisotropy of ~0 due to molecular rotations on the order of several picoseconds.[116] Given the slow depolarization that occurs due to molecular rotation during the fluorescence lifetime, anisotropy measurements on FPs can illuminate other processes that lead to depolarization such as energy transfer.

5.1.4 Time-resolved FRET

Measurement of FRET efficiency and molecular separation is typically estimated with steady-state FP FRET measurements. However, FPs, hence show broad excitation and emission spectra, can contaminate the FRET emission channel with cross-talk. The FRET efficiency is defined as the fraction of photons absorbed by the donor transferred to the acceptor. Donor lifetime measurements are more accurate in the determination of FRET efficiency (E) due to fewer contributions to signal in the donor emission channel. FRET efficiency can be calculated through the formula[110]:

$$E = 1 - \frac{\tau_{DA}}{\tau_{D}} \tag{5.6}$$

where τ_{DA} is the lifetime of the donor in the presence of the acceptor and τ_D is the lifetime of the donor alone. It should be noted that in many systems, the donor lifetime is artificially inflated due to the presence of free donors that are not interacting with acceptors, which are not accounted for in this equation. The determination of R using E requires knowledge of κ^2, which in the case of FPs in unlikely to be the dynamically-averaged value of 2/3. This is due to the aforementioned slow rotation during their fluorescence lifetime. An alternative formulation for determined R from E has been proposed for FRET pairs within the static random isotropic orientational regime by Vogel *et al*.[117] This regime accounts for the slow rotation of an FP (approximately static over the fluorescence lifetime), but an isotropic distributions of dipole orientations. Table 1 of reference 7 presents values for the determination of R from E based on experimentally derived values.

One alternative method for the determination of the FRET efficiency is the measurement of the rise of acceptor fluorescence in the FRET channel.[118,119] Since only active FRET donors will lead to acceptor emission in the absence of significant donor bleedthrough, the rise time is a reporter on the rate of transfer between donor and acceptor. However, this method excels only when there is minimal bleed-through of the donor emission into the FRET channel, because this contamination causes an artificial shortening of the rise time.[120,121]

Utilization of time-resolved anisotropy to measure FRET has been sparse, however a few examples exist in the literature.[121–123] Steady-state imaging anisotropy is more readily used in microscopy as an alternative to sensitized emission and fluorescence lifetime imaging microscopy.[124–127] One notable example with close parallels to the sensor in use for Zn^{2+}, is a study of the Ca^{2+} ECFP-calmodulin-cpVenus FRET sensor, YC3.60 by Borst *et al*.[120] In this study, the researchers utilized, among other techniques, time-resolved fluorescence anisotropy to

determine the energy transfer angle, FRET rate, and flexibility of the construct in the ligand free and bound states. YC3.60 was suggested to become more flexible in its Ca^{2+} free state, as determined by an increase in the rotational correlation time of the acceptor. This study suggested that the large dynamic range of YC3.60 was due primarily to the distance change, rather than an orientational change through the use of TRFA and fluorescence correlation spectroscopy, which measures diffusion rates of molecules by means of fluorescence emission.

Presently, there is little information on the molecular dynamics of the genetically-encoded Zn^{2+} sensors discussed in this thesis. Steps have been taken to understand how they perform *in vivo* (Chapter 4). This chapter makes progress on understanding the sensors in more molecular detail by assessment of their photophysics using time-resolved fluorescence (TRF) and anisotropy. Calculations are done to assess the effect of crosstalk and active FRET populations have on the measurements. The sensors used in this study (introduced in Chapter 4) are: ZapCY1, eCALWY-4, and eZinCh-2. Additionally, two sensors with circular permutation of the acceptor FP were purified to investigate the how changes in the relative orientation of the donor and acceptor ion the affect. These sensors, named ZifCV1.173 and ZifCV1.157 (ECFP(trunc)-Zif1-cpVenus), use a single zinc-finger ZBD (Zif1) and the last three-digit number indicates the position in mVenus to which the N-terminus was relocated. cpVenus173 relocates the fusion site to a position on the opposite end of the barrel. cpVenus157 retains the N-terminus on the same side of the barrel as the parent, but placed within a turn of the beta-sheet instead of the original N-terminal helix.[40] These sensors were purified and initial measurements made on their donor and acceptor lifetime and anisotropy in ligand free and saturated conditions.

5.2 Experimental Setup

5.2.1 Sample Preparation

All sensors and fluorescent proteins were cloned into pBAD between the BamHI and EcoRI restriction sites and expressed in Top-10 *Escherichia coli* with the addition of 0.2% m/v arabinose. Unless otherwise stated, proteins were purified using Ni^{2+} ion affinity chromatography and the His tag was removed with TEV protease (Promega) in 1 mM DTT, 20mM Tris, 100 mM NaCl, pH 8 buffer at 30ºC for 6 hours and 4ºC overnight with a sensor to TEV protease ratio of 10:1. The sample was again run on a Ni^{2+} ion affinity column to separate cleaved protein from uncleaved protein and cleaved His tag. Purified constructs were concentrated with an Amicon-Ultra centrifugal filter (EMD Millipore) to 20-80 µM as determined by the absorbance at a specific wavelength governed by the isolated FP or acceptor FP and the corresponding absorption coefficient listed in Table 5.1 obtained from the literature.[5]

Fluorescent Protein	λ (nm)	ε ($M^{-1}cm^{-1}$)
ECFP	433	32500
mCerulean	433	43000
mVenus	515	94500
mCitrine	516	77000

Table 5.1. Fluorescent protein absorption coefficients at specified wavelengths used to determine protein concentrations during protein purification.

Purified sensor was subjected two conditions: saturating Zn^{2+} and Zn^{2+} chelating conditions. A saturating Zn^{2+} condition was achieved by creation of a buffered Zn^{2+} solution (3:7 Zn/Ca/EGTA:Ca/EGTA), made at pH 7.4 using a pH titration method described previously.[128] The concentration of accessible Zn^{2+} in the buffer was 12 µM. 100 µM EDTA (prepared from 25 mM EDTA, pH 8.0) was used as the Zn^{2+} chelating condition with no added Zn^{2+}. Experiments

were performed in HEPES buffer (150 mM HEPES, 100 mM NaCl, pH 7.4 made with chelexed water) with 500 nM sensor protein, treated for 5 minutes prior to Zn^{2+} or EDTA addition with 1 mM TCEP. TCEP is included to reduce cysteine residues that are present in all sensors studied. All samples were 0.2 μM filtered prior to the experiment.

5.2.2 Instrumentation

Steady state polarization measurements were made on a QM-6 fluorimeter (Photon Technology International) with a T-configured PMT detector scheme for simultaneous detection of the parallel and perpendicular fluorescence emission signal. Calibration was checked using Erythrosin B in water,[129] which has an anisotropy of 0.235 measured at 525 nm excitation and 549 nm emission wavelengths. All slit widths (excitation and emission) were set to 6 nm. Emission was scanned from 460-560 nm with 444 nm excitation.

Time-resolved measurements were made on a FluoTime 100 fluorescence lifetime spectrometer (PicoQuant) equipped with a TimeHarp 260 PICO TCSPC module and photomultiplier detector assembly (PMA 182). Plane polarized excitation (further denoted as vertically polarized) is provided by a 440 nm pulsed diode laser at a frequency of 10 MHz and power adjusted to ~ 1 $\mu W/cm^2$. The IRF (typically 200 ps FWHM) was measured using a dilute Ludox suspension. Donor and FRET emission were collected through 483/32 nm and 542/27 nm bandpass filters (Semrock), respectively. Figure 5.2 shows the detection window overlaid with ECFP and mCitrine absorption and emission spectra. Vertically polarized emission was collected at 1.1×10^5 counts/sec (adjusted by an iris in front of the emission filter) for 600 s. Data were collected, without touching the iris, in the following order for each sample: FRET channel: VV, VH, VM; Donor channel: VV, VH, VM. VM is vertically polarized excitation and emission collected with the polarizer angle set to 54.7^o (magic angle). The G-Factor for the instrument,

which corrects for polarization bias, was assumed to be 1 for all fits and confirmed by multiple measurements of HV and HH emission in initial experiments. Iterative reconvolution and global analysis of the data was performed using the provided FluoFit software (PicoQuant). Error analysis for individual decay curves was conducted at the 67% confidence level for lifetimes and rotational correlation times. Traces are offset from zero by 21500 ps. All results shown in this chapter are single replicate values. Therefore, error analysis across multiple experiments was not conducted.

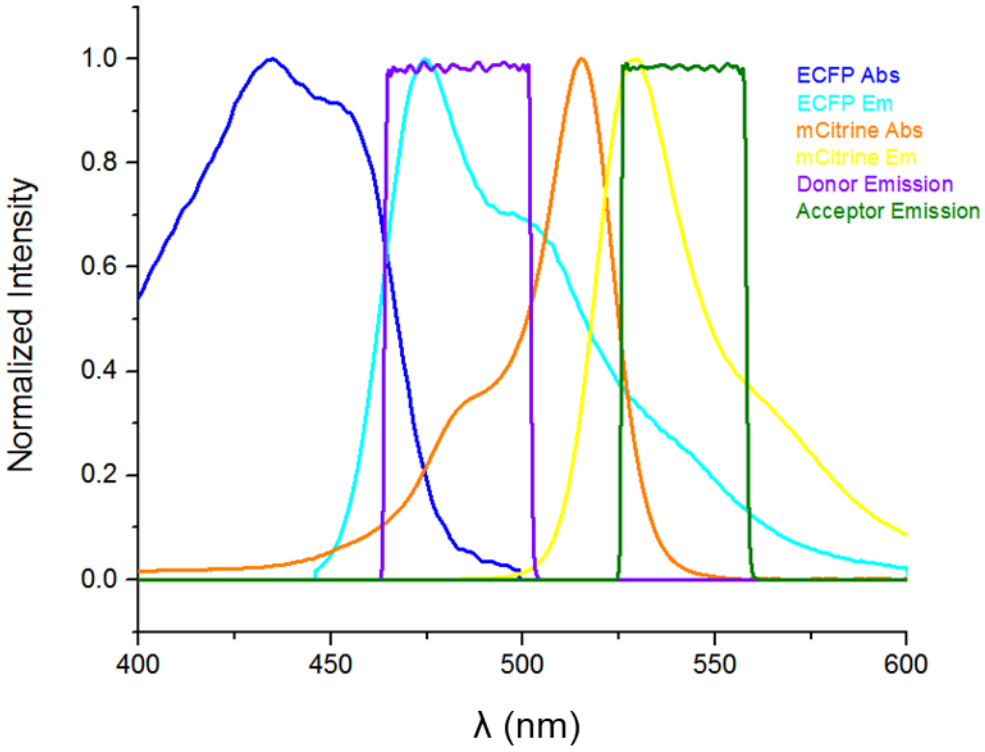


Figure 5.2. Detection windows overlaid on amplitude normalized ECFP and mCitrine absorption/emission spectrum. Considerable donor emission can be found in the acceptor emission window.

5.3 Fluorescence Anisotropy Calculations

To estimate the effect of the parameters that convolute the signal in the FRET channel, calculations were performed to simulate behavior of the FRET anisotropy as a function of transfer angle (i.e. angle between donor and acceptor transition dipole moments, Fig. 5.1b). It is assumed here that the rotation of the TDMs themselves relative to the separation vector are fixed. For the constructs under study, it would be beneficial to understand the effect of non-interacting fractions of donor emission and donor bleed-through on the FRET anisotropy measurements. For measurements on FPs, the FRET channel contains contributions from multiple sources: acceptor lifetime, FRET transfer (acceptor rise), quenched donor emission (bleed-through), FRET inactive or unquenched donor emission, and direct acceptor excitation. Calculations of the time-dependent polarized emission signals were adapted from Masters *et al* for a one photon process and can be found in Appendix B.[122] Assuming equal ground state populations (N_{gs}), the populations of interacting and non-interacting donors and acceptors ($N_{I,D}$,$N_{I,A}$, $N_{NI,D}$, and $N_{NI,A)}$ are:

$$
\begin{aligned}
N_{I,D}(t) &= T_D N_{gs} F_I \exp(-(k_{fret}+k_{di,f})t) \\
N_{I,A}(t) &= T_D N_{gs} F_I X[\exp(-(k_{fret}+k_{di,f})t)-\exp(-k_{ai,f}t)] \\
N_{NI,D}(t) &= T_D N_{gs}(1-F_I)\exp(-k_{dni,f}t) \\
N_{NI,A}(t) &= T_A N_{gs}\exp(-k_{ani,f}t)
\end{aligned}
\qquad (5.7)
$$

where $X = k_{FRET}/(k_{FRET} + k_{di,f}-k_{ai,f})$. T_D and T_A are the one-photon excitation probabilities for the donor and acceptor. F_I is the interaction fraction from 0 to 1 (1 indicating that all molecules undergo FRET). $k_{di,f}$, $k_{ai,f}$, $k_{dni,f}$ and $k_{ani,f}$ are the inverse of the fluorescence lifetimes for interacting and non-interacting ECFP and mCitrine. After a short pulsed excitation, the intensity of each of these components is proportional to the fraction of emission in the detection window

and the radiative rate of that component. Application of these intensities to Equations 5.3 and 5.4 yields the total intensity in the parallel and perpendicular channels. These components can be applied to Equation 5.2 and summed over their weighted components to derive the total anisotropy in the FRET channel. This yields the following equation, dependent on the transfer angle, θ_{da}:

$$r(t,\theta_{da}) = \left(\frac{2}{5}\right)\left(\frac{\begin{array}{c}(F_I(1-(BX)/2)(3(\cos[\theta_{da}]^2)-1)\exp[-(k_{FRET}+k_{af})t]\exp[-k_{rot}t])\\ +(0.5)F_I BX\exp[-k_{af}t]((3(\cos[\theta_{da}]^2)-1)\exp[-k_{rot}t])\\ +(1-F_I)\exp[-k_{df}t]\exp[-k_{rot}t]\\ +B\delta\exp[-k_{rot}t]\exp[-k_{af}t]\end{array}}{\begin{array}{c}F_I(1-BX)\exp[-(k_{FRET}+k_{af})t])+F_I BX\exp[-k_{af}t]\\ +(1-F_I)\mathrm{Exp}[-k_{df}t]+B\delta\exp[-k_{af}t]\end{array}}\right) \quad (5.8)$$

where B is the ratio of acceptor to donor emission in the detection window and δ is the ratio of acceptor absorption to donor absorption at the excitation wavelength. For simplicity, the orientational relaxation of the donor and acceptor have assumed to be equivalent to the rotation of the entire FRET sensor ($1/k_{rot}$ = 30 ns for these calculations). This assumption has the potential to introduce inaccuracies as shown in the study of YC3.60, if there is a difference in flexibility for the donor and acceptor domains. The value of k_{FRET} is determined at fixed $R = R_o$ (Forster distance for ECFP and mCitrine = 4.9 nm). δ is assumed ~ 1%, which is reasonable given the low absorption probability of the mVenus and mCitrine at 440 nm. B is calculated using commercially available spectra for filters and fluorophores. B was calculated for three pairs of fluorophores in our system using the following equation:

$$B = \frac{\frac{Integrated\ transmission\ acceptor}{Integrated\ emission\ acceptor} * Radiative\ rate\ acceptor}{\frac{Integrated\ transmission\ donor}{Integrated\ emission\ donor} * Radiative\ rate\ donor} \quad (5.9)$$

The values for B for ECFP/Citrine, ECFP/Venus, and Cerulean/Citrine are 5.89, 5.41, and 3.54 respectively. The decreasing values of B indicate the higher proportion of donor emission in the acceptor channel. For comparison, in a EGFP/mCherry filter set for the two fluorophores, B =

19.9.[130] The small value of B is a result of the broad emission spectrum of ECFP, which also makes it a good FRET donor for the YFPs, leading to a large value of the spectral overlap integral. Cerulean, derived from ECFP, has a higher quantum yield, while retaining the broad emission leading to higher bleed-through into the FRET channel.

The results of the calculations are shown in Figure 5.3. Figure 5.3a shows the results in the initial 10 ns window. The B and F_I parameters are varied at numerical extremes. A value of B with little donor emission was chosen (30) and compared to a value corresponding to the ECFP/mCitrine (5.89) for 100% interacting molecules. Then, the effect of decreasing the fraction of donors interacting with acceptors is shown for 100% vs. 10%. A number of qualitative trends are observed. The first observation is that an increase in transfer angle, θ_{da}, correlates with a decrease in the magnitude of r at all times and that large transfer angles can result in a negative anisotropy value that begins to rise as molecular rotation, t_{rot}, becomes dominant. Decreasing values of B result in an increase in the measure anisotropy due to the large presence of donor emission. Decrease in the interacting fraction also leads to a more modest increase in the measured anisotropy at in the first 2 nanoseconds. Figure 5.3b expands the timescale to highlight the eventual convergence of the anisotropy values to 0 due to the isotropic reorientation of the whole molecule. However, it is unlikely this will be observed outside of the fluorescence lifetime of the fluorophore at which time the signal to noise will be limiting.

The measured anisotropy curves will be affected by bleed-through effects in these CFP/YFP sensors due to a low B value in the range of 3-6. Any measured curve will exhibit higher anisotropy values than would be calculated in the absence of donor emission in the FRET channel. However, initial experiments should give a qualitative picture of the magnitude of reorientation due to the binding of ligand in these sensors. This information may provide insight

into what factors drive the FRET changed observed upon ligand binding and whether the FRET change is dominated by reorientation or distance changes between the two fluorescent proteins. Future calculations that correspond to the fitted data will need to include parameters obtained from the measurements including treating the two FPs separately with respect to their reorientation. Additionally, noise and orientational/distance population distributions (based on Gaussian distributions)[110] could be included to more accurately reflect the measured data and obtain quantitative results.

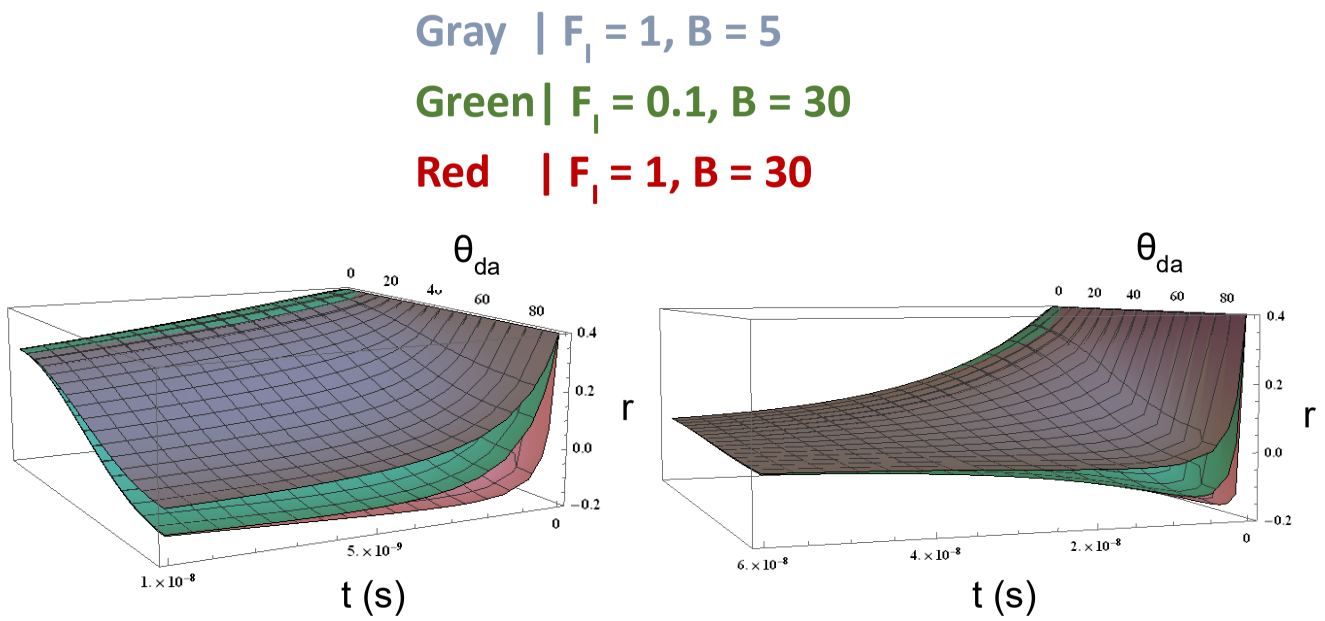


Figure 5.3. Left: First 10 ns of anisotropy decay (r) following vertically polarized excitation. Increase in transfer angle (θ_{da}) results in a decrease in the amplitude of the slow anisotropy component (anisotropy past the first few nanosecond). Right: Time window opened to 60 ns to display the convergence of the anisotropy to zero after molecules have rotated sufficiently to achieve an isotropic distribution. Parameters shown above (in order of amplitude in r) with corresponding colors.

5.4 Time-resolved Fluorescence Results

5.4.1 TRF of a Small Molecule Dye

Fluorescein dianion (H_2O, pH 11) was measured at 500 nM to validate the ability of the instrument to accurately reflect the magnitude of fluorescence anisotropy, as well as picosecond rotational correlation times (φ). The results of this experiment are shown in Figure 5.4 with parameters obtained from exponential reconvolution in Table 5.2. The average lifetime is in agreement with the 4 ns lifetime reported in the literature. The vertical and horizontal components are displayed in Fig. 5.4a, while the anisotropy trace (convoluted with the IRF) is shown in Fig. 5.4b. The rotational correlation time is on the same order as similarly sized dyes in water.[114] The value of r(0) matches closely with the literature value of 0.38. The estimated anisotropy at steady-state is approximately 0, as is expected for a small molecule with a long fluorescence lifetime. The molecule can sufficiently reach an isotropic distribution of orientations on a timescale much faster than the fluorescence lifetime.

<t> (ns)	β	φ (ps)	r(0)	r(ss), est	χ^2, red
3.9	0.39 (±0.015)	120 (± 4)	0.39	0.01	1.055

Table 5.2. Parameters for exponential reconvolution fits for Fluorescein traces in Figure

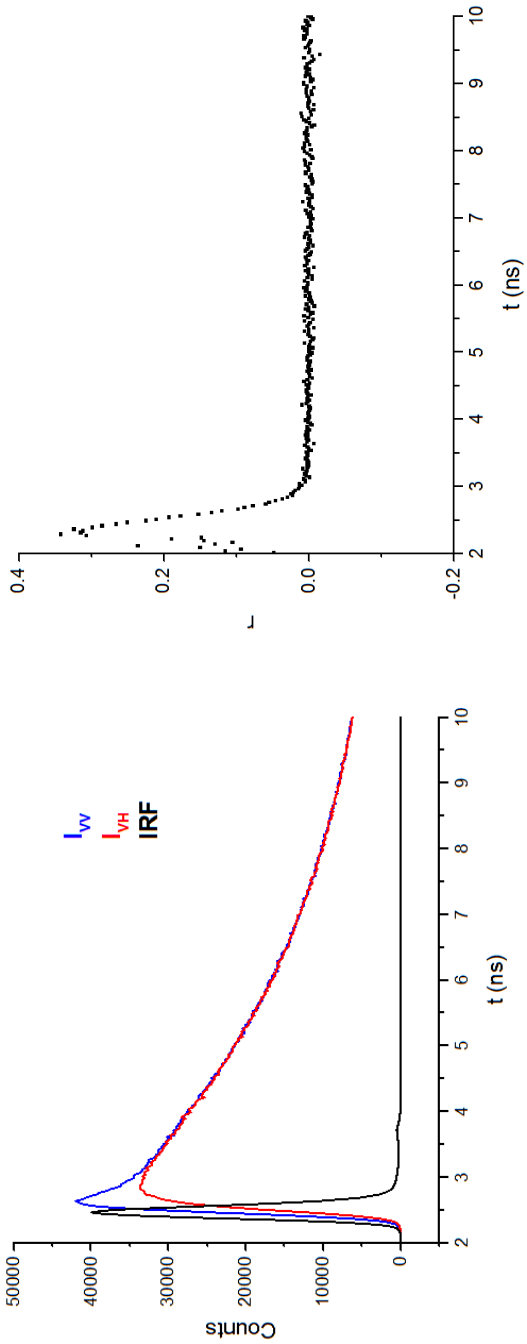


Figure 5.4. a) Intensity component traces and IRF for fluorescein in H_2O (pH 11). B) Raw anisotropy trace that quickly approaches zero due to the rapid reorientation of the small molecule dye during the comparatively long fluorescence lifetime.

5.4.2 Effect of His-tag on ECFP Zn^{2+} Response using TRF

Steady-state measurements on the Zif sensors and ECFP were conducted to verify response of the sensors following Zn^{2+} addition and probe the system for an anisotropy change (Figure 5.5). Upon 100 μM Zn^{2+} addition, both sensors showed a slight increase in the anisotropy in the donor region corresponding to the decrease in lifetime of ECFP. ZifCV1.173 showed an increase in anisotropy in the acceptor region, while ZifCV1.157 showed a decrease. The relative positioning of the anisotropy curves suggests a greater orientation difference in ZifCV1.173 between donor and acceptor, however time-resolved measurements are required to confirm this interpretation. Notably, truncated ECFP also showed a response to added Zn^{2+}, suggesting modification of the fluorescence lifetime. For these proteins, the 6xHis-tag was not removed after purification and concentration and the change in lifetime could result from Zn^{2+} binding tp the His tag, particularly given the high concentration of Zn^{2+} included.

To investigate the effects of the His-tag on the ECFP lifetime, time-resolved fluorescence was measured for truncated ECFP with and without the His-tag in the presence and absence of Zn^{2+}. Figure 5.6 shows the TCSPC traces and fitted parameters are in Table 5.3. Visual inspection of the traces shows a clear shift in the lifetime for the tagged ECFP in the presence of Zn^{2+}. The average lifetime (amplitude weighted) decreases by 18% relative to the cleaved protein in EDTA. Cleaved protein also shows a 6% decrease, either indicative of a sensitivity

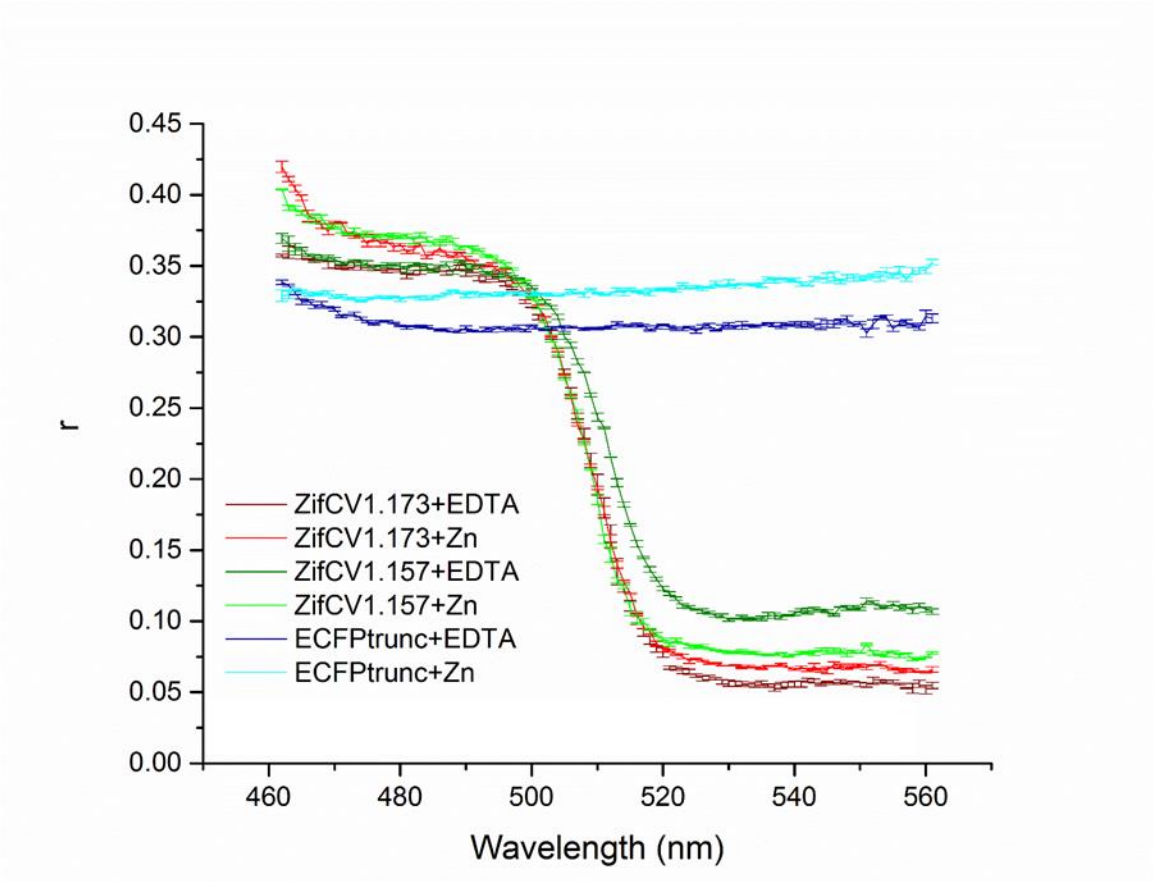


Figure 5.5. Emission scan steady-state anisotropy for two zinc sensors with ECFP as a donor protein, but different acceptor proteins (cpVenus157 or cpVenus173). Proteins were treated with either 100 μM Zn^{2+} or 100 μM EDTA. Excitation was set to 444 nm.

of ECFP or incomplete cleavage of the tag. The decrease in lifetime comes from the decrease in amplitude of the long lifetime component. As mentioned previously, ECFP has shown sensitivity of the His148 and Tyr145 positions to changes in the environment. Molecules or ions can interact with these residues and alter the conformation of the chromophore. A TRF study shows an increase in lifetime of ECFP due to interaction with ATP.[22] His-tags have been shown to bind Zn^{2+} and are the basis of a reported Zn^{2+} sensor.[131] This result shows the impact modification of the FP can have and requirement of controls to guarantee tags and other fusions do not modify response. All subsequent measurements are made after treatment with TEV protease to remove the His-tag and additional column purification to remove uncleaved protein from the sample.

		α_1	τ_1 (ns)*	α_2	τ_2 (ns)	α_3	τ_3 (ns)	<t>, ns
ECFP(trunc)	EDTA	0.39	3.64	0.33	1.79	0.28	0.51	**2.15**
ECFP(trunc)	Zn	0.34	3.64	0.35	1.82	0.31	0.5	**2.02**
6xHis-ECFP(trunc)	EDTA	0.38	3.64	0.34	1.8	0.27	0.54	**2.16**
6xHis-ECFP(trunc)	Zn	0.17	3.64	0.50	1.93	0.32	0.56	**1.78**

Table 5.3. Parameters for exponential reconvolution fits for ECFP traces in Figure 5.6. * indicates this parameter was globally fit across data sets.

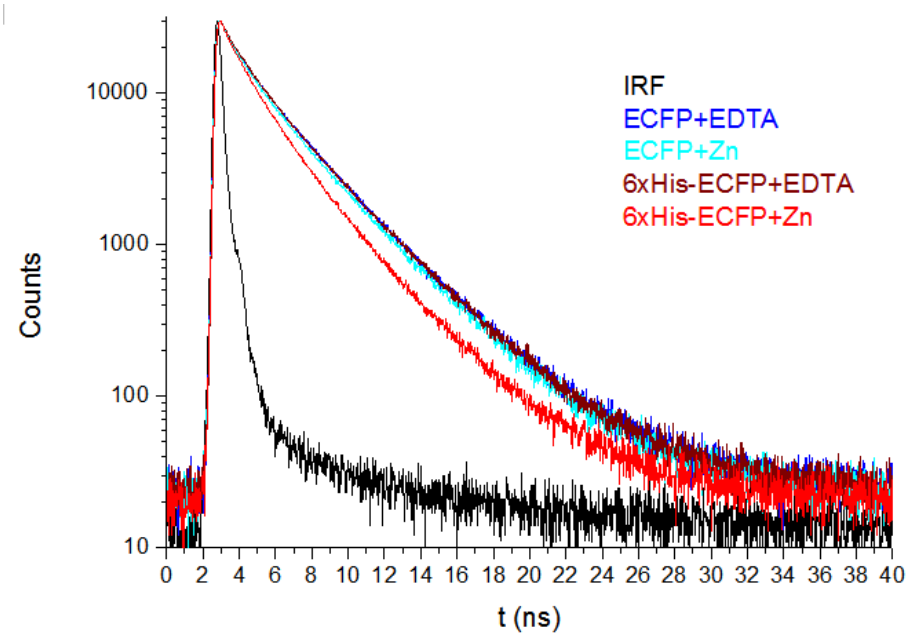


Figure 5.6. TCSPC traces for the ECFP treated with and without TEV protease for removal of an N-terminal His-tag in the presence and absence of 100 μM Zn^{2+} or 100 μM EDTA.

5.4.3 Time-resolved Fluorescence Measurements on Zinc Sensors

Time-resolved measurements of ZapCY1, eCALWY-4 and eZinCh-2 are shown in Figures 5.7, 5.8 and 5.9, respectively. Parameters for the reconvolution fits are included in Tables 5.4, 5.5 and 5.6, respectively. ECFP and Cerulean are included as reference traces for corresponding sensors. For each sensor, the amplitude-weighted lifetime in the donor channel is calculated and a corresponding efficiency (E_{FRET}) is calculated (Equation 5.6). As discussed earlier in this chapter, this lifetime is likely influenced by any inactive FRET donors which would render the FRET efficiency artificially low. R_{DA}, the distance between donor and acceptor TDMs, is calculated using the empirically derived separations for static random isotropic orientational relaxation found in the publication by Vogel *et al* mentioned earlier.[117] The rise time (negative amplitude in the fit) is determined for each sensor in the FRET channel and a corresponding FRET efficiency is calculated using this as the FRET rate ($E_{FRET, rise}$).

ZapCY1 shows a 13% decrease in donor lifetime upon Zn^{2+} binding. This change in lifetime suggests a lower FRET efficiency. Acceptor rise times are in the nanosecond range, with a decrease in rise time upon binding, consistent with a higher FRET efficiency. The efficiency calculated using acceptor rise time is higher than that using the donor lifetimes. This is consistent with the results observed in YC3.60. eCALWY-4 shows a 30% increase in donor lifetime, consistent with the mode of FRET sensing for this platform, in which binding of Zn^{2+} leads to a separation of the donor and acceptor. Smaller separations are calculated for eCALWY-4 in the high FRET state compared to ZapCY1. Rise times for eCALWY-4 likewise show higher FRET efficiencies. eZinCh-2 shows the largest change in donor lifetime (53%), corresponding to the largest change in FRET efficiency, and therefore largest change in R_{DA}. However, the acceptor rise times for eZinch-2 are on the order of the width of the IRF in this system and do not show

significant change. Either the transfer occurs on a timescale faster than we can resolve, or confounding factors are contributing to the fast rise. As shown previously, the overlap factor (B) is higher for the Cerulean variants which greatly affects the measured rise time.[132] Additionally, eZinCh-2 has been shown to readily form aggregates *in vivo* and *in vitro* (Chapter 4). These larger aggregates could enhance scattered light, artificially increasing amplitudes of shorter lifetimes. Future replicates of these data should utilize a non-denaturing gel to check for the presence of aggregates and/or size-exclusion chromatography should be run to isolate monomers. ZifCV1.173 and ZifCV1.157 were excluded from this measurement due to low dynamic range and irreproducible lifetime changes.

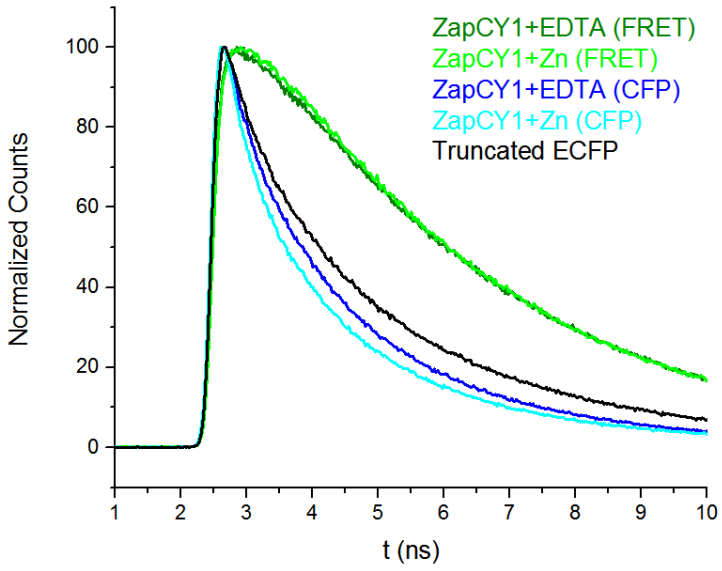


Figure 5.7. Amplitude normalized magic angle intensity traces for ZapCY1. Sensors are treated with 100 μM EDTA or 12 μM buffered Zn^{2+} - Ca^{2+}/EGTA. 1 mM TCEP is present in all samples.

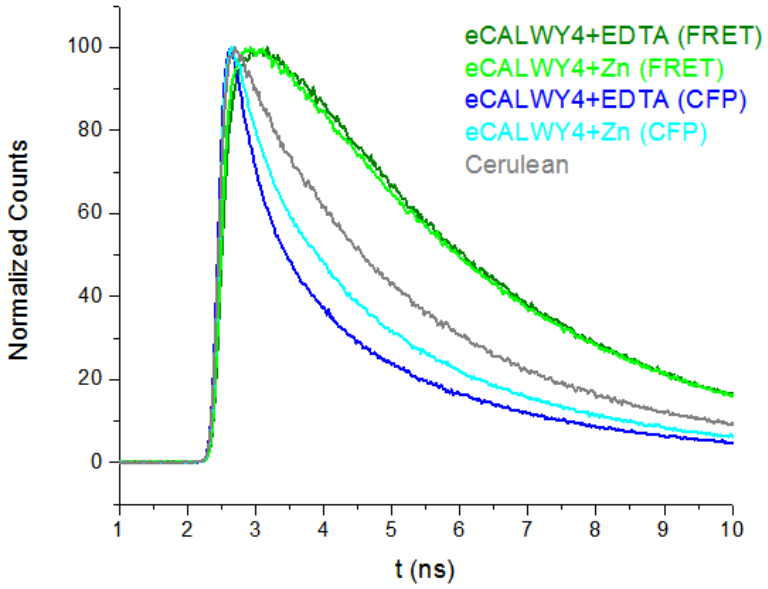


Figure 5.8. Ampliude normalized magic angle intensity traces for eCALWY-4. . Sensors are treated with 100 µM EDTA or 12 µM buffered Zn^{2+} - Ca^{2+}/EGTA. 1 mM TCEP is present in all samples.

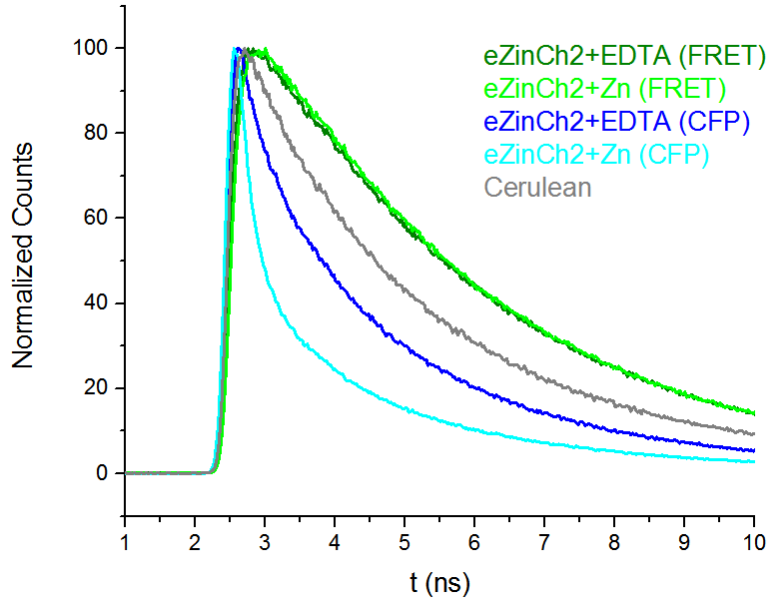


Figure 5.9. Amplitude normalized magic angle intensity traces for eZinCh-2. Sensors are treated with 100 µM EDTA or 12 µM buffered Zn^{2+} - Ca^{2+}/EGTA. 1 mM TCEP is present in all samples.

ZapCY1	$<t_{CFP}>$ (ns)	E_{FRET}	R_{DA} (nm)	t_{rise}, FRET (ns)	$E_{FRET, rise}$
EDTA	1.59	0.23	5.62	1.025 ± 0.029	0.50
Zn^{2+}	1.38	0.33	5.04	0.742 ± 0.090	0.64

Table 5.4. Parameters for exponential reconvolution fits for ZapCY1 traces in Figure 5.7.

eCALWY-4	$<t_{CFP}>$ (ns)	E_{FRET}	R_{DA} (nm)	t_{rise}, FRET (ns)	$E_{FRET, rise}$
EDTA	1.38	0.50	4.54	0.416 ± 0.025	0.85
Zn^{2+}	1.80	0.34	5.30	0.519 ± 0.043	0.81

Table 5.5. Parameters for exponential reconvolution fits for eCALWY-4 traces in Figure 5.8.

eZinCh-2	$<t_{CFP}>$ (ns)	E_{FRET}	R_{DA} (nm)	t_{rise}, FRET (ns)	$E_{FRET, rise}$
EDTA	1.50	0.46	4.74	0.286 ± 0.127	0.89
Zn^{2+}	0.70	0.75	3.37	0.149 ± 0.022	0.94

Table 5.6. Parameters for exponential reconvolution fits for eZinCh-2 traces in Figure 5.9.

5.4.4 Time-resolved Fluorescence Anisotropy Results for Zinc Sensors

A combined plot of FRET anisotropy traces for all sensors is shown in Figure 5.10 for the purpose of a qualitative comparison of the sensors. Recalling the results of the steady-state measurements on ZifCV1.173/157, the same ordering of relative FRET anisotropy is observed. Compared to all sensors, ZifCV1.173 has the lowest anisotropy value past 4 ns, even extending into the negatives. This is notable as this sensor is the only one to have the acceptor attached at the opposite end of the protein. The CV family uses Venus, however, Citrine is a related FP with a difference of only a few residues within the barrel without significant change of the TDM vector.[23,133] A second observation is that there is an increase in anisotropy upon Zn^{2+} binding for

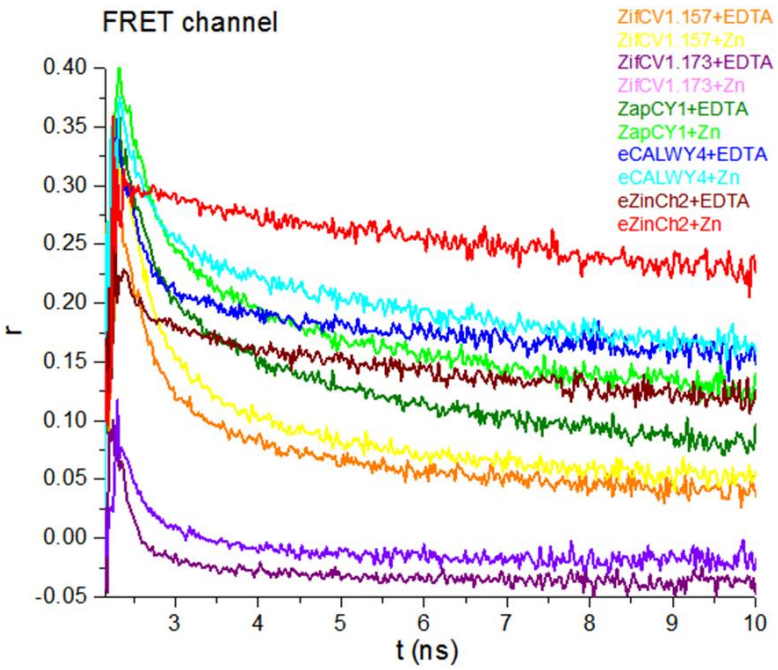


Figure 5.10. Raw FRET anisotropy traces for all sensors showing a qualitatively diverse landscape of acceptor orientations. Data are convoluted with the IRF, making r_0 impossible to visualize. ZifCV1.173 (purple) shows a negative amplitude for the slow anisotropy component. Sensors treated with 100 μM EDTA or 12 μM buffered Zn^{2+} - Ca^{2+}/EGTA. 1 mM TCEP is present in all samples.

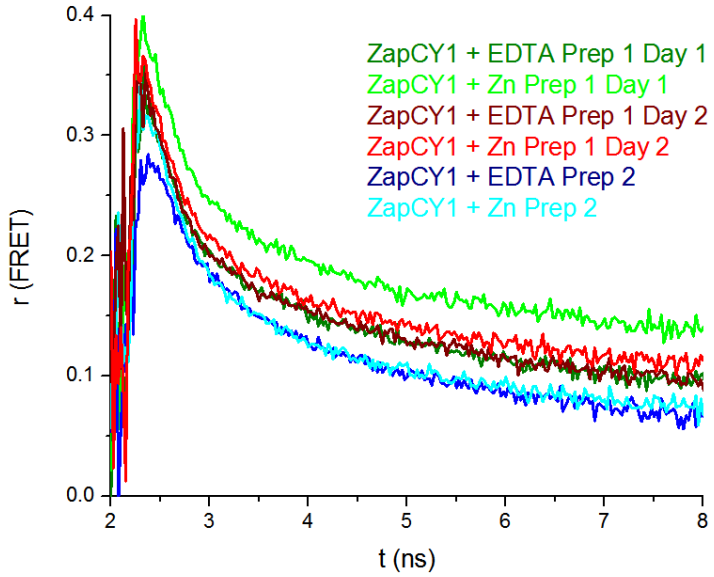
all sensors, which could correspond to an increased alignment of the donor/acceptor TDMs as a mechanism of sensor response.

Analysis of the anisotropy traces for three replications of ZapCY1 show considerable variability for different protein preparations and over time for the same protein preparation. Figure 5.11 and 5.12 shows the FRET channel and donor channel data, respectively. Fit parameters are listed in Tables 5.7 and 5.8 for FRET and donor channel, respectively. It is remarkable that across these experiments, the donor anisotropy and lifetime shows consistent results, however, the acceptor anisotropy change and relative amplitude changes more drastically. FRET channel lifetimes also remain consistent across the data set. Preliminary data suggests that all sensors under study show decreased dynamic range in oxidizing conditions.[†] The variation in FRET channel anisotropy and comparative consistency of the donor channel anisotropy may provide structural evidence for the loss of sensor response in which angular change is restricted for the acceptor. Figure 5.11 also displays the calculated transfer angle for each data set. This is calculated similar to Borst *et al* for YC3.60 using the amplitude of the rotational correlation time corresponding to the rotation of the molecule as a whole, which has the lowest error (see β_3 in Figure 5.10). θ_T is calculated using:

$$\beta \cong r_0 \frac{3\langle cos^2\theta_T\rangle}{2} \tag{5.10}$$

[†] Unpublished work from *in vitro* sensor study by Molly Carpenter in Chapter 4.

Since r_0 for Citrine is undetermined using this instrument, lacking the necessary excitation wavelength, it is assumed to be 0.37 in accordance with the limiting anisotropy measured for ECFP (less than 0.4 due to instrument limitations).[112] As time increases past protein purification, ZapCY1 shows a decrease in the change of transfer angle ($41^o \rightarrow 37^o$ vs. $41^o \rightarrow 40^o$). ZapCY1 is unique in that it required 3 rotational exponentials to fit the FRET data with minimal reduced χ^2. It is also notable that there is a fast depolarization in the first nanosecond in the donor channel for ZapCY1, despite an



$\theta_{T,1} = 41^{o} \rightarrow 37^{o}$

$\theta_{T,2} = 41^{o} \rightarrow 40^{o}$

$\theta_{T,3} = 44^{o} \rightarrow 43^{o}$

Figure 5.11. (Top left) Raw FRET anisotropy traces for three data sets of ZapCY1 on different days or different preps. (Top right) Calculated transfer angles based on the amplitude of the slow rotational correlation time (β_3) Sensors are treated with 100 μM EDTA or 12 μM buffered Zn^{2+} - Ca^{2+}/EGTA. 1 mM TCEP is present in all samples.

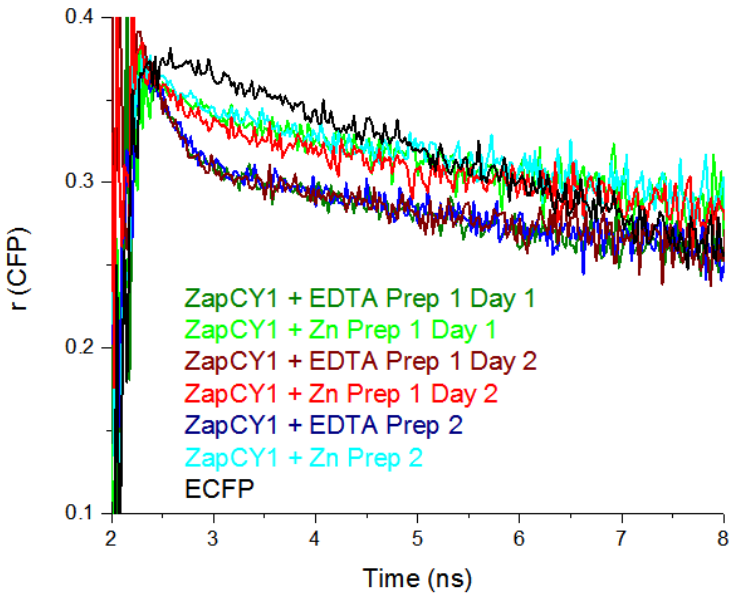


Figure 5.12. Raw donor anisotropy traces for three data sets of ZapCY1 on different days or different preps. Sensors are treated with 100 µM EDTA or 12 µM buffered Zn^{2+} - Ca^{2+}/EGTA. 1 mM TCEP is present in all samples.

ZapCY1		α_1	τ_1 (ns)[a]	α_2	τ_2 (ns)[b]	β_1	φ_1 (ns)	β_2	φ_2 (ns)	β_3	φ_3 (ns)	Red χ^2	r(0) est	r(ss) est	
EDTA	FRET	0.83	3.567 ± 0.004	0.17	1.025 ± 0.029	0.105 ± 0.013	1.214 ± 0.312	0.067 ± 0.023	0.187 ± 0.179	0.127 ± 0.0061	14.68 ± 2.80	1.086	0.299	0.127	Prep 1 Day 1
Zn	FRET	0.82	3.567 ± 0.004	0.18	0.742 ± 0.090	0.123 ± 0.015	1.048 ± 0.329	0.071 ± 0.046	0.154 ± 0.128	0.173 ± 0.0060	25.15 ± 6.42	1.081	0.367	0.177	
EDTA	FRET	0.83	3.567 ± 0.004	0.17	0.974 ± 0.090	0.099 ± 0.012	1.382 ± 0.263	0.082 ± 0.039	0.223 ± 0.113	0.131 ± 0.0005	16.65 ± 3.34	1.073	0.312	0.135	Prep 1 Day 2
Zn	FRET	0.82	3.567 ± 0.004	0.18	0.694 ± 0.078	0.057 ± 0.012	1.915 ± 0.368	0.102 ± 0.019	0.517 ± 0.211	0.141 ± 0.0056	19.85 ± 3.80	1.119	0.3	0.148	
EDTA	FRET	0.82	3.567 ± 0.004	0.18	1.027 ± 0.087	0.114 ± 0.014	1.273 ± 0.247	0.092 ± 0.047	0.135 ± 0.070	0.103 ± 0.0056	18.86 ± 6.05	1.102	0.309	0.115	Prep 2
Zn	FRET	0.80	3.567 ± 0.004	0.20	0.819 ± 0.063	0.102 ± 0.012	1.367 ± 0.325	0.090 ± 0.012	0.295 ± 0.128	0.111 ± 0.0053	20.81 ± 4.63	1.126	0.303	0.126	

a. globally fit across data sets., b. negative amplitude corresponding to fluorescence rise.

Table 5.7. Compiled fitted parameters for three data sets of ZapCY1 in the FRET channel with associated errors. α is the amplitude of the corresponding fluorescence decay (τ). β is the amplitude of the corresponding rotational correlation time (φ). r(0) and r(ss) are calculated by FluoFit during the fitting process.

ZapCY 1		α_1	τ_1 (ns)*	α_2	τ_2 (ns)	α_3	τ_3 (ns)	β_1	φ_1 (ns)	β_2	φ_2 (ns)	Red χ^2	r(0) est	r(ss) est	
EDTA	CFP	0.24	3.246 ± 0.015	0.44	1.612 ± 0.027	0.32	0.396 ± 0.036	0.034 ± 0.019	0.576 ± 0.550	0.305 ± 0.007	31.52 ± 8.15	1.03	0.339	0.288	Prep 1 Day 1
Zn	CFP	0.21	3.246 ± 0.015	0.40	1.370 ± 0.027	0.39	0.336 ± 0.027	0.024 ± 0.020	0.562 ± 0.541	0.340 ± 0.008	34.97 ± 9.68	1.02	0.365	0.318	
EDTA	CFP	0.24	3.246 ± 0.015	0.45	1.606 ± 0.027	0.32	0.400 ± 0.036	0.049 ± 0.023	0.382 ± 0.287	0.302 ± 0.007	37.30 ± 11.60	1.00	0.351	0.287	Prep 1 Day 2
Zn	CFP	0.22	3.246 ± 0.015	0.41	1.408 ± 0.028	0.37	0.370 ± 0.027	0.022 ± 0.019	0.620 ± 0.590	0.348 ± 0.008	33.41 ± 9.40	1.01	0.360	0.315	
EDTA	CFP	0.24	3.246 ± 0.015	0.42	1.52 ± 0.029	0.35	0.344 ± 0.031	0.061 ± 0.039	0.178 ± 0.147	0.317 ± 0.007	29.02 ± 4.71	1.05	0.379	0.299	Prep 2
Zn	CFP	0.20	3.246 ± 0.015	0.40	1.37 ± 0.026	0.39	0.336 ± 0.024	0.023 ± 0.019	0.583 ± 0.522	0.342 ± 0.008	38.7 ± 11.4	1.04	0.365	0.326	

a. globally fit across data sets.

Table 5.8. Compiled fitted parameters for three data sets of ZapCY1 in the CFP channel with associated errors. α is the amplitude of the corresponding fluorescence decay (τ). β is the amplitude of the corresponding rotational correlation time (φ). r(0) and r(ss) are calculated by FluoFit during the fitting process. ECFP fit: (r_0 = 0.377, φ = 15.0 ± 0.7 ns, r_{ss} = 0.312)

overall increase in steady-state anisotropy upon Zn^{2+} binding. This fast depolarization is present in all sensors containing ECFP (data not shown). The cause is presently undetermined, but likely related to the complex dynamics characteristic of the ECFP, such as a conformational change of the chromophore.

FRET anisotropy traces for the Cerulean sensors, eCALWY-4 and eZinCh-2, are found in Figure 5.13 and fit data in Table 5.9. Donor traces are found in Figure 5.14 and fit data in Table 5.10. There is no evidence of the fast depolarization in the Cerulean sensors that is present in the ECFP sensors. This may be attributed to the stabilization of the chromophore through mutation of His148.[134] eZinCh-2 has the largest change in transfer angle ($39^o \rightarrow 25^o$). As reported in the literature, knowledge of θ_T permits limits to be placed on the value of κ^2. However, without knowledge of θ_D and θ_A, Equation 5.5 shows κ^2 values still span almost the entire range of possible values for $\theta_T = 41^o$.[120] It is possible that θ_D and θ_A may be determined in analog constructs in which the coinciding FRET partner is dark.[111]

The rotational correlation times for all sensors are > 20 ns, as measured by donor anisotropy. These times are associated with large uncertainties due to the magnitude of the decay relative to the fluorescence lifetime. The long correlation times fit in the FRET anisotropy data are unreliable without direct measurement of the YFP anisotropy. While correlation times from the fits do change between ligand conditions and across data sets, the large errors complicate drawing precise conclusions about the flexibility of either the CFP or YFP domains. To corroborate these data, fluorescence correlation spectroscopy (FCS) could be done on the sensors to determine diffusion constants and rotational times. There needs to be rigorous characterization of the protein samples that are subject to such measurements.

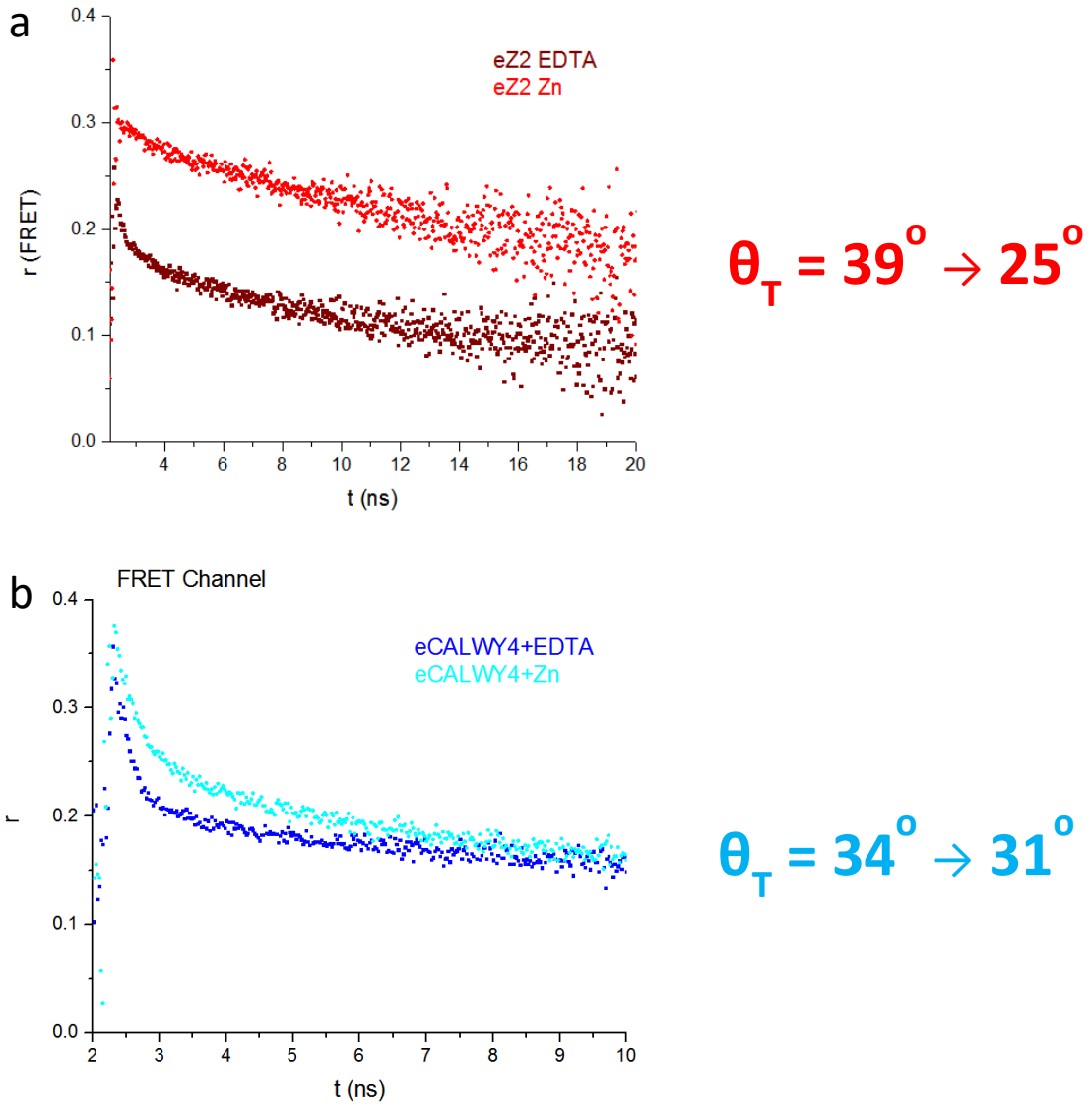


Figure 5.13. (a) Raw FRET anisotropy traces for ZinCh-2 and calculated transfer angles based on the amplitude of the slow rotational correlation time (β_1). (b) Raw anisotropy traces for eCALWY-4 and calculated transfer angles based on the amplitude of the slow rotational correlation time (β_1). EDTA = 100 μM. Zn^{2+} = 12 μ M buffered (Ca/EGTA). 1 mM TCEP present in all samples.

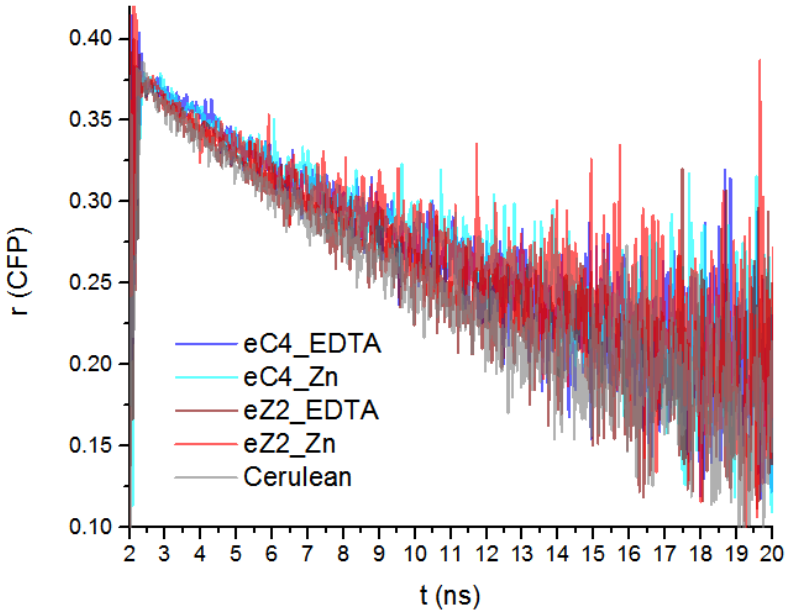


Figure 5.14. Raw donor anisotropy traces for eZinCh-2 and eCALWY-4. Sensors are treated with 100 µM EDTA or 12 µM buffered Zn^{2+} - Ca^{2+}/EGTA. 1 mM TCEP is present in all samples.

			α_1	τ_1 (ns)*	α_2	τ_2 (ns)#	β_1	θ_1 (ns)	β_2	θ_2 (ns)	Red χ^2	r(0) est	r(ss) est
eZinCh-2	EDTA	FRET	0.92	3.460 ± 0.008	0.08	0.286 ± 0.127	0.151 ± 0.005	32.12 ± 8.43	0.043 ± 0.010	1.725 ± 0.715	1.04	0.193	0.148
	Zn	FRET	0.72	3.460 ± 0.008	0.28	0.149 ± 0.022	0.273 ± 0.005	38.7 ± 11.6	0.024 ± 0.008	2.54 ± 1.83	1.06	0.296	0.256
eCALWY-4	EDTA	FRET	0.74	3.546 ± 0.007	0.26	0.416 ± 0.025	0.194 ± 0.003	35.94 ± 4.85	0.053 ± 0.013	0.515 ± 0.173	1.01	0.248	0.180
	Zn	FRET	0.82	3.546 ± 0.007	0.18	0.519 ± 0.043	0.218 ± 0.003	27.44 ± 2.85	0.086 ± 0.010	0.796 ± 0.139	1.05	0.303	0.203

*globally fit across data sets., #negative amplitude corresponding to fluorescence rise.

Table 5.9. Compiled fitted parameters for eZinCh-2 and eCALWY-4 traces in the FRET channel with associated errors. α is the amplitude of the corresponding fluorescence decay (τ). β is the amplitude of the corresponding rotational correlation time (φ). r(0) and r(ss) are calculated by FluoFit during the fitting process.

			α_1	τ_1 (ns)*	α_2	τ_2 (ns)	α_3	τ_3 (ns)	β_1	θ_1 (ns)	Red χ^2	r(0) est	r(ss) est
eCALWY-4	EDTA	CFP	0.25	3.595 ± 0.013	0.22	1.31 ± 0.027	0.53	0.360 ± 0.010	0.374 ± 0.004	23.92 ± 2.18	1.03	0.374	0.332
	Zn	CFP	0.33	3.595 ± 0.013	0.29	1.57 ± 0.028	0.38	0.394 ± 0.017	0.373 ± 0.004	26.04 ± 2.41	1.036	0.372	0.332
eZinCH-2	EDTA	CFP	0.27	3.473 ± 0.016	0.33	1.43 ± 0.024	0.40	0.202 ± 0.014	0.368 ± 0.005	21.01 ± 2.15	1.09	0.368	0.322
	Zn	CFP	0.11	3.473 ± 0.016	0.16	1.19 ± 0.022	0.73	0.171 ± 0.004	0.370 ± 0.006	25.45 ± 3.27	1.17	0.370	0.335

*globally fit across data sets.

Table 5.10. Compiled fitted parameters for eZinCh-2 and eCALWY-4 traces in the CFP channel with associated errors. α is the amplitude of the corresponding fluorescence decay (τ). β is the amplitude of the corresponding rotational correlation time (φ). r(0) and r(ss) are calculated by FluoFit during the fitting process.

5.5 Conclusions and Future Directions

This chapter presents initial results on the characterization of a panel of genetically encoded Zn^{2+} sensors using time-resolved fluorescence techniques. The instrument is validated using a control fluorophore. The effect of His-tag fusion on ECFP during Zn^{2+} studies is determined, indicating that cleavage of the affinity tag is required to more accurately reflect *in vivo* response. There is clear variability in the response of the sensors over time and across protein preparations. This is the primary path for future experiments prior to refinement of the data analysis. The purification process for oxidation sensitive proteins should be optimized, either by the addition of reducing agents throughout the process or using anaerobic techniques. Unpublished work by Molly Carpenter has determined sensor responsiveness varies across colonies from a single transformation experiment, suggesting variation in bacterial translation of a sensor from the obtained plasmid. As mentioned previously, more rigorous characterization or isolation of the purified sensor should be done by non-denaturing gels and/or size-exclusion chromatography. Measurements of a sensor's response to zinc and confirmation of the binding constant, K_D, should also be performed. There are likely problems associated with the length of time it takes to cleave the His-tag (several hours to overnight), which increase the duration the protein is exposed to ambient conditions before measurement. Pulsed laser excitation at ~ 500 nm should be implemented to directly measure acceptor anisotropy. FCS can be done to corroborate the correlation times measured for the protein rotation. Lastly, time studies should also be performed for eZinCh-2 and eCALWY-4 to determine if they show similar FRET anisotropy variability as observed for ZapCY1. When optimized, this technique should prove crucial in investigating the effects of oxidation, crowding and other environmental effects on the sensors.

Bibliography

1. Tsien, R. Y. The Green Fluorescent Protein. *Annu. Rev. Biochem.* **67,** 509–544 (1998).
2. Shaner, N. C., Steinbach, P. A. & Tsien, R. Y. A guide to choosing fluorescent proteins. *Nat. Methods* **2,** 905–9 (2005).
3. Niwa, H. *et al.* Chemical nature of the light emitter of the Aequorea green fluorescent protein (imidazolone excited state phenolate anion low-temperature f luorescence photoisomerization). *Biochem. Commun. by Martin D. Kamen* **93,** 13617–13622 (1996).
4. VanEngelenburg, S. B. & Palmer, A. E. Fluorescent biosensors of protein function. *Curr. Opin. Chem. Biol.* **12,** 60–65 (2008).
5. Day, R. N. & Davidson, M. W. The fluorescent protein palette: tools for cellular imaging. *Chem. Soc. Rev.* **38,** 2887 (2009).
6. Newman, R. H., Fosbrink, M. D. & Zhang, J. Genetically Encodable Fluorescent Biosensors for Tracking Signaling Dynamics in Living Cells. *Chem. Rev.* **111,** 3614–3666 (2011).
7. Carter, K. P., Young, A. M. & Palmer, A. E. Fluorescent Sensors for Measuring Metal

Ions in Living Systems. *Chem. Rev.* **114,** 4564–4601 (2014).

8. Tamura, T. & Hamachi, I. Recent Progress in Design of Protein-Based Fluorescent Biosensors and Their Cellular Applications. *ACS Chem. Biol.* (2014). doi:10.1021/cb500661v

9. Lindenburg, L. & Merkx, M. Engineering genetically encoded FRET sensors. *Sensors (Basel).* **14,** 11691–713 (2014).

10. Frommer, W. B., Davidson, M. W. & Campbell, R. E. Genetically encoded biosensors based on engineered fluorescent proteins. *Chem. Soc. Rev.* **38,** 2833 (2009).

11. Sample, V., Mehta, S. & Zhang, J. Genetically encoded molecular probes to visualize and perturb signaling dynamics in living biological systems. *J. Cell Sci.* **127,** 1151–1160 (2014).

12. Palmer, A. E., Qin, Y., Park, J. G. & McCombs, J. E. Design and application of genetically encoded biosensors. *Trends Biotechnol.* **29,** 144–52 (2011).

13. Matsu-ura, T. *et al.* Cytosolic inositol 1,4,5-trisphosphate dynamics during intracellular calcium oscillations in living cells. *J. Cell Biol.* **173,** 755–765 (2006).

14. Nausch, L. W. M., Ledoux, J., Bonev, A. D., Nelson, M. T. & Dostmann, W. R. Differential patterning of cGMP in vascular smooth muscle cells revealed by single GFP-linked biosensors. *Proc. Natl. Acad. Sci. U. S. A.* **105,** 365–370 (2008).

15. Russwurm, M. *et al.* Design of fluorescence resonance energy transfer (FRET)-based cGMP indicators: a systematic approach. *Biochem. J.* **407,** 69–77 (2007).

16. Cano Abad, M. F. *et al.* Mitochondrial pH Monitored by a New Engineered Green Fluorescent Protein Mutant. *J. Biol. Chem.* **279,** 11521–11529 (2004).

17. Wang, W. *et al.* Superoxide Flashes in Single Mitochondria. *Cell* **134,** 279–290 (2008).

18. Chen, T.-W. *et al.* Ultrasensitive fluorescent proteins for imaging neuronal activity. *Nature* **499,** 295–300 (2013).

19. Abdelfattah, A. S. *et al.* A Bright and Fast Red Fluorescent Protein Voltage Indicator That Reports Neuronal Activity in Organotypic Brain Slices. *J. Neurosci.* **36,** 2458–2472 (2016).

20. Taslimi, A. *et al.* An optimized optogenetic clustering tool for probing protein interaction and function. *Nat. Commun.* **5,** 4925 (2014).

21. Taslimi, A. *et al.* Optimized second-generation CRY2–CIB dimerizers and photoactivatable Cre recombinase. *Nat. Chem. Biol.* **12,** 425–430 (2016).

22. Borst, J. W. *et al.* ATP changes the fluorescence lifetime of cyan fluorescent protein via an interaction with His148. *PLoS One* **5,** 1–7 (2010).

23. Nagai, T. *et al.* A variant of yellow fluorescent protein with fast and efficient maturation for cell-biological applications. *Nat. Biotechnol.* **20,** 87–90 (2002).

24. Blindauer, C. a. Advances in the molecular understanding of biological zinc transport. *Chem. Commun.* (2015). doi:10.1039/C4CC10174J

25. Grewer, C. & Gameiro, A. How do glutamate transporters function as transporters and ion channels? *Biophys. J.* **107,** 546–7 (2014).

26. Frederickson, C. J. *et al.* Concentrations of extracellular free zinc (pZn)e in the central nervous system during simple anesthetization, ischemia and reperfusion. *Exp. Neurol.* **198,** 285–93 (2006).

27. Duncan, F. E. *et al.* The zinc spark is an inorganic signature of human egg activation. *Sci. Rep.* **6,** 24737 (2016).

28. Que, E. L. *et al.* Quantitative mapping of zinc fluxes in the mammalian egg reveals the

origin of fertilization-induced zinc sparks. *Nat. Chem.* (2014). doi:10.1038/nchem.2133

29. Dean, K. M., Qin, Y. & Palmer, A. E. Visualizing metal ions in cells: an overview of analytical techniques, approaches, and probes. *Biochim. Biophys. Acta* **1823,** 1406–15 (2012).

30. Qin, Y. *et al.* Direct comparison of a genetically encoded sensor and small molecule indicator: Implications for quantification of cytosolic Zn2+. *ACS Chem. Biol.* **8,** 2366–2371 (2013).

31. Sensi, S. L., Ton-That, D., Weiss, J. H., Rothe, A. & Gee, K. R. A new mitochondrial fluorescent zinc sensor. *Cell Calcium* **34,** 281–284 (2003).

32. Campbell, R. E. Fluorescent-protein-based biosensors: Modulation of energy transfer as a design principle. *Anal. Chem.* **81,** 5972–5979 (2009).

33. Dittmer, P. J., Miranda, J. G., Gorski, J. a & Palmer, A. E. Genetically encoded sensors to elucidate spatial distribution of cellular zinc. *J. Biol. Chem.* **284,** 16289–97 (2009).

34. Vinkenborg, J. L. *et al.* Genetically encoded FRET sensors to monitor intracellular Zn2+ homeostasis. *Nat. Methods* **6,** 737–40 (2009).

35. Hessels, A. M. *et al.* eZinCh-2: A Versatile, Genetically Encoded FRET Sensor for Cytosolic and Intraorganelle Zn 2+ Imaging. *ACS Chem. Biol.* **10,** 2126–2134 (2015).

36. Wang, D., Hurst, T. K., Thompson, R. B. & Fierke, C. a. Genetically encoded ratiometric biosensors to measure intracellular exchangeable zinc in Escherichia coli. *J. Biomed. Opt.* **16,** 87011 (2011).

37. Qin, Y., Sammond, D. W., Braselmann, E., Carpenter, M. C. & Palmer, A. E. Development of an Optical Zn2+ Probe Based on a Single Fluorescent Protein. *ACS Chem. Biol.* **11,** 2744–2751 (2016).

38. Aper, S. J. A., Dierickx, P. & Merkx, M. Dual readout BRET/FRET-sensors for measuring intracellular zinc. *ACS Chem. Biol.* acschembio.6b00453 (2016). doi:10.1021/acschembio.6b00453

39. Wang, Z. *et al.* Solution structure of a Zap1 zinc-responsive domain provides insights into metalloregulatory transcriptional repression in Saccharomyces cerevisiae. *J. Mol. Biol.* **357,** 1167–83 (2006).

40. Park, J. G., Qin, Y., Galati, D. F. & Palmer, A. E. New Sensors for Quantitative Measurement of Mitochondrial Zn 2+. *ACS Chem. Biol.* **7,** 1636–1640 (2012).

41. Qin, Y., Dittmer, P. J., Park, J. G., Jansen, K. B. & Palmer, A. E. Measuring steady-state and dynamic endoplasmic reticulum and Golgi Zn2+ with genetically encoded sensors. *Proc. Natl. Acad. Sci. U. S. A.* **108,** 7351–6 (2011).

42. Chabosseau, P. *et al.* Mitochondrial and ER-Targeted eCALWY Probes Reveal High Levels of Free Zn(2+). *ACS Chem. Biol.* **9,** 2111–20 (2014).

43. McCombs, J. E. & Palmer, A. E. Measuring calcium dynamics in living cells with genetically encodable calcium indicators. *Methods* **46,** 152–9 (2008).

44. Shapiro, H. M. *Practical Flow Cytometry*. (John Wiley & Sons, Inc., 2003). doi:10.1002/0471722731

45. Beumer, T., Lenssinck, H., Pennings, A. & Haanen, C. An easy-to-build-timer for kinetic measurements in flow cytometry. *Cytometry* **5,** 648–51 (1984).

46. Scampavia, L. D., Blankenstein, G., Ruzicka, J. & Christian, G. D. A coaxial jet mixer for rapid kinetic analysis in flow injection and flow injection cytometry. *Anal. Chem.* **67,** 2743–9 (1995).

47. Blankenstein, G., Scampavia, L. D., Ruzicka, J. & Christian, G. D. Coaxial flow mixer for

real-time monitoring of cellular responses in flow injection cytometry. *Cytometry* **25,** 200–204 (1996).

48. Nolan, J. P., Posner, R. G., Martin, J. C., Habbersett, R. & Sklar, L. A. A rapid mix flow cytometer with subsecond kinetic resolution. *Cytometry* **21,** 223–9 (1995).

49. Litzlbauer, J. *et al.* Large Scale Bacterial Colony Screening of Diversified FRET Biosensors. *PLoS One* **10,** e0119860 (2015).

50. Ibraheem, A., Yap, H., Ding, Y. & Campbell, R. E. A bacteria colony-based screen for optimal linker combinations in genetically encoded biosensors. *BMC Biotechnol.* **11,** 105 (2011).

51. Belal, A. S. F., Sell, B. R., Hoi, H., Davidson, M. W. & Campbell, R. E. Optimization of a genetically encoded biosensor for cyclin B1-cyclin dependent kinase 1. *Mol. Biosyst.* **10,** 191–5 (2014).

52. Zhao, Y. Y. *et al.* Microfluidic cell sorter-aided directed evolution of a protein-based calcium ion indicator with an inverted fluorescent response. *Integr. Biol.* **6,** 714 (2014).

53. Teh, S.-Y., Lin, R., Hung, L.-H. & Lee, A. P. Droplet microfluidics. *Lab Chip* **8,** 198 (2008).

54. Mazutis, L. *et al.* Single-cell analysis and sorting using droplet-based microfluidics. *Nat. Protoc.* **8,** 870–891 (2013).

55. Clausell-Tormos, J. *et al.* Droplet-based microfluidic platforms for the encapsulation and screening of Mammalian cells and multicellular organisms. *Chem. Biol.* **15,** 427–37 (2008).

56. Agresti, J. J. *et al.* Ultrahigh-throughput screening in drop-based microfluidics for directed evolution. *Proc. Natl. Acad. Sci.* **107,** 4004–4009 (2010).

57. Baret, J.-C. *et al.* Fluorescence-activated droplet sorting (FADS): efficient microfluidic cell sorting based on enzymatic activity. *Lab Chip* **9,** 1850–8 (2009).

58. Clausell-Tormos, J., Griffiths, A. D. & Merten, C. a. An automated two-phase microfluidic system for kinetic analyses and the screening of compound libraries. *Lab Chip* **10,** 1302–1307 (2010).

59. Frenz, L., Blank, K., Brouzes, E. & Griffiths, A. D. Reliable microfluidic on-chip incubation of droplets in delay-lines. *Lab Chip* **9,** 1344–1348 (2009).

60. Huebner, A. *et al.* Development of quantitative cell-based enzyme assays in microdroplets. *Anal. Chem.* **80,** 3890–6 (2008).

61. Huebner, A. *et al.* Quantitative detection of protein expression in single cells using droplet microfluidics. *Chem. Commun. (Camb).* **2,** 1218–20 (2007).

62. Stone, H. A. in *CMOS Biotechnology* 5–30 (2007). doi:10.1007/978-0-387-68913-5_2

63. Brody, J. P., Yager, P., Goldstein, R. E. & Austin, R. H. Biotechnology at low Reynolds numbers. *Biophys. J.* **71,** 3430–41 (1996).

64. Borle, A. B. Kinetic Analyses of Calcium Movements in HeLa Cell Cultures: I. Calcium influx. *J. Gen. Physiol.* **53,** 43–56 (1969).

65. Berthier, J. & Silberzan, P. *Microfluidics for Biotechnology*. (Artech House, 2010).

66. Collins, D. J., Neild, A., DeMello, A., Liu, A.-Q. & Ai, Y. The Poisson distribution and beyond: methods for microfluidic droplet production and single cell encapsulation. *Lab Chip* **15,** 3439–3459 (2015).

67. Abate, a. *et al.* Impact of inlet channel geometry on microfluidic drop formation. *Phys. Rev. E* **80,** 26310 (2009).

68. Collins, D. J., Alan, T., Helmerson, K. & Neild, A. Surface acoustic waves for on-demand

production of picoliter droplets and particle encapsulation. *Lab Chip* **13,** 3225 (2013).

69. Wu, T.-H. *et al.* Pulsed laser triggered high speed microfluidic fluorescence activated cell sorter. *Lab Chip* **12,** 1378 (2012).

70. Abate, A. R., Romanowsky, M. B., Agresti, J. J. & Weitz, D. a. Valve-based flow focusing for drop formation. *Appl. Phys. Lett.* **94,** 23503 (2009).

71. Lee, C.-H., Hsiung, S.-K. & Lee, G.-B. A tunable microflow focusing device utilizing controllable moving walls and its applications for formation of micro-droplets in liquids. *J. Micromechanics Microengineering* **17,** 1121–1129 (2007).

72. Baret, J.-C. Surfactants in droplet-based microfluidics. *Lab Chip* **12,** 422–33 (2012).

73. Holtze, C. *et al.* Biocompatible surfactants for water-in-fluorocarbon emulsions. *Lab Chip* **8,** 1632 (2008).

74. Holt, D. J., Payne, R. J., Chow, W. Y. & Abell, C. Fluorosurfactants for microdroplets: interfacial tension analysis. *J. Colloid Interface Sci.* **350,** 205–11 (2010).

75. Datta, S. & Ghosal, S. Characterizing dispersion in microfluidic channels. *Lab Chip* **9,** 2537 (2009).

76. Ma, S., Sherwood, J. M., Huck, W. T. S. & Balabani, S. On the flow topology inside droplets moving in rectangular microchannels. *Lab Chip* **14,** 3611–20 (2014).

77. Wyatt Shields IV, C., Reyes, C. D. & López, G. P. Microfluidic cell sorting: a review of the advances in the separation of cells from debulking to rare cell isolation. *Lab Chip* **15,** 1230–1249 (2015).

78. Cristobal, G., Benoit, J.-P., Joanicot, M. & Ajdari, A. Microfluidic bypass for efficient passive regulation of droplet traffic at a junction. *Appl. Phys. Lett.* **89,** 34104 (2006).

79. Guo, M. T., Rotem, A., Heyman, J. a & Weitz, D. a. Droplet microfluidics for high-

throughput biological assays. *Lab Chip* **12,** 2146–55 (2012).

80. Lubbeck, J. L., Dean, K. M., Ma, H., Palmer, A. E. & Jimenez, R. Microfluidic flow cytometer for quantifying photobleaching of fluorescent proteins in cells. *Anal. Chem.* **84,** 3929–37 (2012).

81. Puck, T. T., Marcus, P. I. & Cieciura, S. J. Clonal Growth of Mammalian Cells In Vitro. *J Exp Med* **103,** 273–284 (1956).

82. Ma, H., Gibson, E. A., Dittmer, P. J., Jimenez, R. & Palmer, A. E. High-throughput examination of fluorescence resonance energy transfer-detected metal-ion response in mammalian cells. *J. Am. Chem. Soc.* **134,** 2488–2491 (2012).

83. Miranda, J. G. *et al.* New alternately colored FRET sensors for simultaneous monitoring of Zn^{2+} in multiple cellular locations. *PLoS One* **7,** e49371 (2012).

84. Pomorski, A., Kochańczyk, T., Miłoch, A., Krężel, A. & Kręzel, A. Method for accurate determination of dissociation constants of optical ratiometric systems: Chemical probes, genetically encoded sensors, and interacting molecules. *Anal. Chem.* **85,** 11479–11486 (2013).

85. Abate, A. R. *et al.* Correction for Agresti et al., Ultrahigh-throughput screening in drop-based microfluidics for directed evolution. *Proc. Natl. Acad. Sci.* **107,** 6550–6550 (2010).

86. McDonald, J. C. *et al.* Fabrication of microfluidic systems in poly(dimethylsiloxane). *Electrophoresis* **21,** 27–40 (2000).

87. Dean, K. M. *et al.* High-speed multiparameter photophysical analyses of fluorophore libraries. *Anal. Chem.* **87,** 5026–5030 (2015).

88. Matochko, W. L. *et al.* Deep sequencing analysis of phage libraries using Illumina platform. *Methods* **58,** 47–55 (2012).

89. Glanville, J. *et al.* Deep sequencing in library selection projects: What insight does it bring? *Curr. Opin. Struct. Biol.* **33,** 146–160 (2015).

90. Sung Hwan Cho, Chen, C. H., Tsai, F. S. & Yu-Hwa Lo. Micro-fabricated fluorescence-activated cell sorter. in *2009 Annual International Conference of the IEEE Engineering in Medicine and Biology Society* 1075–1078 (IEEE, 2009). doi:10.1109/IEMBS.2009.5334976

91. Davis, L. M., Lubbeck, J. L., Dean, K. M., Palmer, A. E. & Jimenez, R. Microfluidic cell sorter for use in developing red fluorescent proteins with improved photostability. *Lab Chip* **13,** 2320–2327 (2013).

92. Fu, A. Y., Spence, C., Scherer, A., Arnold, F. H. & Quake, S. R. A microfabricated fluorescence-activated cell sorter. *Nat. Biotechnol.* **17,** 1109–11 (1999).

93. Wolff, A. *et al.* Integrating advanced functionality in a microfabricated high-throughput fluorescent-activated cell sorter. *Lab Chip* **3,** 22–7 (2003).

94. Wang, M. M. *et al.* Microfluidic sorting of mammalian cells by optical force switching. *Nat. Biotechnol.* **23,** 83–87 (2005).

95. Dittrich, P. S. & Schwille, P. An Integrated Microfluidic System for Reaction, High-Sensitivity Detection, and Sorting of Fluorescent Cells and Particles. *Anal. Chem.* **75,** 5767–5774 (2003).

96. Dolega, M. E. *et al.* Iterative operations on microdroplets and continuous monitoring of processes within them; determination of solubility diagrams of proteins. *Lab Chip* **12,** 4022 (2012).

97. Fu, A. Y., Chou, H. P., Spence, C., Arnold, F. H. & Quake, S. R. An integrated microfabricated cell sorter. *Anal. Chem.* **74,** 2451–2457 (2002).

98. Park, J. G., Qin, Y., Galati, D. F. & Palmer, A. E. New Sensors for Quantitative Measurement of Mitochondrial Zn2+. *ACS Chem. Biol.* **7,** 1636–1640 (2012).

99. Hessels, A. M. & Merkx, M. Simple Method for Proper Analysis of FRET Sensor Titration Data and Intracellular Imaging Experiments Based on Isosbestic Points. *ACS Sensors* **1,** 498–502 (2016).

100. Costantini, L. M. *et al.* A palette of fluorescent proteins optimized for diverse cellular environments. *Nat. Commun.* **6,** 7670 (2015).

101. Bender, B. J. *et al.* Protocols for Molecular Modeling with Rosetta3 and RosettaScripts. *Biochemistry* **55,** 4748–4763 (2016).

102. Maret, W. & Li, Y. Coordination dynamics of zinc in proteins. *Chem. Rev.* **109,** 4682–707 (2009).

103. Baird, G. S., Zacharias, D. A. & Tsien, R. Y. Circular permutation and receptor insertion within green fluorescent proteins. *Proc. Natl. Acad. Sci.* **96,** 11241–11246 (1999).

104. Chalfie, M., Tu, Y., Euskirchen, G., Ward, W. W. & Prasher, D. C. Green fluorescent protein as a marker for gene expression. *Science (80-.).* **263,** 802–805 (1994).

105. Hires, S. A., Zhu, Y. & Tsien, R. Y. Optical measurement of synaptic glutamate spillover and reuptake by linker optimized glutamate-sensitive fluorescent reporters. *Proc. Natl. Acad. Sci.* **105,** 4411–4416 (2008).

106. Komatsu, N. *et al.* Development of an optimized backbone of FRET biosensors for kinases and GTPases. *Mol. Biol. Cell* **22,** 4647–4656 (2011).

107. Mank, M. *et al.* A FRET-Based Calcium Biosensor with Fast Signal Kinetics and High Fluorescence Change. *Biophys. J.* **90,** 1790–1796 (2006).

108. Lelimousin, M. *et al.* Intrinsic dynamics in ECFP and cerulean control fluorescence

quantum yield. *Biochemistry* **48,** 10038–10046 (2009).

109. Szmacinski, H. & Lakowicz, J. R. Frequency-domain lifetime measurements and sensing in highly scattering media. *Sensors Actuators B Chem.* **30,** 207–215 (1996).

110. Lakowicz, J. R. *Principles of Fluorescence Spectroscopy*. (Springer US, 2006). doi:10.1007/978-0-387-46312-4

111. Dale, R. E., Eisinger, J. & Blumberg, W. E. The orientational freedom of molecular probes. The orientation factor in intramolecular energy transfer. *Biophys. J.* **26,** 161–193 (1979).

112. Borst, J. W., Hink, M. A., Van Hoek, A. & Visser, A. J. W. G. Effects of refractive index and viscosity on fluorescence and anisotropy decays of enhanced cyan and yellow fluorescent proteins. *J. Fluoresc.* **15,** 153–160 (2005).

113. Van Der Meer, B. W. Kappa-squared: From nuisance to new sense. *Rev. Mol. Biotechnol.* **82,** 181–196 (2002).

114. Ameloot, M., VandeVen, M., Acuña, A. & Valeur, B. Fluorescence anisotropy measurements in solution: Methods and reference materials (IUPAC Technical Report). *Pure Appl. …* **85,** 589–608 (2013).

115. Sarkar, P., Koushik, S. V., Vogel, S. S., Gryczynski, I. & Gryczynski, Z. Photophysical Properties of Cerulean and Venus Fluorescent Proteins. *J. Biomed. Opt.* **14,** 34047 (2009).

116. Boens, N. *et al.* Fluorescence lifetime standards for time and frequency domain fluorescence spectroscopy. *Anal. Chem.* **79,** 2137–49 (2007).

117. Vogel, S. S., Van der Meer, B. W. & Blank, P. S. Estimating the distance separating fluorescent protein FRET pairs. *Methods* **66,** 131–138 (2014).

118. Lindhoud, S., Westphal, A. H., Van Mierlo, C. P. M., Visser, A. J. W. G. & Borst, J. W.

Rise-time of FRET-acceptor fluorescence tracks protein folding. *Int. J. Mol. Sci.* **15,** 23836–23850 (2014).

119. Laptenok, S. P. *et al.* Global analysis of Förster resonance energy transfer in live cells measured by fluorescence lifetime imaging microscopy exploiting the rise time of acceptor fluorescence. *Phys. Chem. Chem. Phys.* **12,** 7593–602 (2010).

120. Borst, J. W. *et al.* Structural Changes of Yellow Cameleon Domains Observed by Quantitative FRET Analysis and Polarized Fluorescence Correlation Spectroscopy. *Biophys. J.* **95,** 5399–5411 (2008).

121. Blacker, T. S. *et al.* Investigating State Restriction in Fluorescent Protein FRET Using Time-Resolved Fluorescence and Anisotropy. *J. Phys. Chem. C* **Submitted,** acs.jpcc.6b11235 (2016).

122. Masters, T. A. *et al.* Restricted State Selection in Fluorescent Protein Förster Resonance Energy Transfer. *J. Am. Chem. Soc.* **135,** 7883–7890 (2013).

123. Visser, N. V., Borst, J. W., Hink, M. A., Van Hoek, A. & Visser, A. J. W. G. Direct observation of resonance tryptophan-to-chromophore energy transfer in visible fluorescent proteins. *Biophys. Chem.* **116,** 207–212 (2005).

124. Ishikawa-Ankerhold, H. C., Ankerhold, R. & Drummen, G. P. C. Advanced fluorescence microscopy techniques--FRAP, FLIP, FLAP, FRET and FLIM. *Molecules* **17,** 4047–132 (2012).

125. Devauges, V. *et al.* Steady-state acceptor fluorescence anisotropy imaging under evanescent excitation for visualisation of FRET at the plasma membrane. *PLoS One* **9,** (2014).

126. Gautier, I. *et al.* Homo-FRET microscopy in living cells to measure monomer-dimer

transition of GFP-tagged proteins. *Biophys. J.* **80,** 3000–3008 (2001).

127. Matthews, D. R. *et al.* Time-lapse FRET microscopy using fluorescence anisotropy. *J. Microsc.* **237,** 51–62 (2010).

128. Tsien, R. & Pozzan, T. in *Biomembranes Part S* (ed. Enzymology, B. T.-M. in) **Volume 172,** 230–262 (Academic Press, 1989).

129. Thompson, R. B., Gryczynski, I. & Malicka, J. Fluorescence polarization standards for high-throughput screening and imaging. *Biotechniques* **32,** 34,37-38,40,42 (2002).

130. Blacker, T. S., Duchen, M. R. & Bain, A. J. Heterogeneity and restricted state selection in FRET with fluorescent proteins. in (eds. Enderlein, J., Gregor, I., Gryczynski, Z. K., Erdmann, R. & Koberling, F.) **9714,** 971401 (2016).

131. Evers, T. H., Appelhof, M. A. M., Meijer, E. W. & Merkx, M. His-tags as Zn(II) binding motifs in a protein-based fluorescent sensor. *Protein Eng. Des. Sel.* **21,** 529–536 (2008).

132. Blacker, T. S. *et al.* Investigating State Restriction in Fluorescent Protein FRET Using Time-Resolved Fluorescence and Anisotropy - Supporting Information. *J. Phys. Chem. C* **121,** (2017).

133. Ansbacher, T. *et al.* Calculation of transition dipole moment in fluorescent proteins--towards efficient energy transfer. *Phys. Chem. Chem. Phys.* **14,** 4109–17 (2012).

134. Goedhart, J. *et al.* Structure-guided evolution of cyan fluorescent proteins towards a quantum yield of 93%. *Nat. Commun.* **3,** 751 (2012).

Appendix A - Protocols

A.1 PDMS Device Manufacturing Protocol

Master | CLEAN ROOM

Cleaning Si substrate (typically 3' wafer):

- Use Piranha (do NOT leave heated Pirahna alone, ~95^{o}C, NO higher, keep all organics away) or NanoStrip at elevated temperature to remove old photoresist.
    - Rinse with Water -> IPA -> Dry with N_2.
- Ash in Reactive Ion Etcher (RIE) with O_2/CF_4 (look up required power and time).
    - Make sure surface is clean or new photoresist may not adhere properly.
- Dry on hotplate at 200 ^{o}C for ~10 min or until certain all water has evaporated.

Making the master: Negative photoresist

- See specific SU-8 3000 instructions for spincoater speeds, exposure times, development times, and bake times (provided by MicroChem, found on website)
- Notes:
    - When using acetate masks, make sure you have a square of glass to substitute the normal glass mask that goes into the Karl Suss MJB3/MJB4 exposure tool.
    - Place the acetate mask with the acetate bubbles facing up (away from the wafer).
    - Exposure time will usually be around 35 seconds, but may change depending on how the lamp is performing and SU8 thickness.
        - ****Lamp has been replaced – Results in drastically lower times. Check lamp power and calculate proper exposure time****
        - ~18 seconds as of June 2017.
    - OPTIONAL: After the master has been made, place in a vacuum chamber with a few drops of (tridecafluoro-1,1,2,2-tetrahydrooctyl)-1-trichlorosilane for 3+ hours. Make sure the master is facing away from the vacuum flow.

Device Fabrication | WET LAB

- Place the master in a petri-dish, tape down both sides.
- Mix a **10:1** weight ratio of pre-polymer and curing agent (Sylgard 184 – Dow Corning) in a weighing dish according to the dimensions of the petri-dish and desired device height (usually 50-60 mm works well to prevent tubing from slipping out). Use 1 g/cm^3 in calculations.
- Degas in vacuum chamber until all bubbles have been removed (~30 min)

- Pour into petri-dish with master. Degas again until all bubbles have been removed (~20-30 min). You can leave the lid to the petri dish on to keep out dust.
- Cover and place in an oven (75 ^{o}C) for at least 1 hr 15 min (can be left overnight @ 65 if the day is ending).

CLEAN ROOM

- Using an exactoknife, carefully cut around the devices, shallowly the first time, then fully the second time to avoid cracking the master with too much force.
- Cut and separate each device.
- Use the 1.2 mm biopsy punch to punch inlets, 1.5 mm biopsy punch for outlets. Do this with the channels facing up. Wipe off the punch with a clean room cloth between devices to clean off PDMS debris.
- Apply frosted scotch tape to both sides of the device. Remove, carefully, the patterned side to remove excess PDMS pieces and dust.

- Rinse the devices with IPA and blow dry with nitrogen. Let them sit on a hotplate set to ~70 ^{o}C for ~10 min.
- At the same time, rinse cover slips for each device in Acetone followed by IPA and let them dry similarly to the devices.

- Place devices and cover slips in a Reactive Ion Etcher (RIE) with the side you wish to bond facing up. Run under O_2 plasma for 15 seconds at 50 W and 50 sccm O_2 pressure..

- Press together on a flat surface, using flat ended tweezers to push out any bubbles (using your fingers will likely cause it to crack, also you want to avoid all contact with your (gloved) hands when possible.
- Let the bonded devices sit for at least 10 minutes on a 70-75 ^{o}C hotplate.

- Prepare a solution of HFE 7500 with 3-4 drops of trichlorosilane compound per mL. Flush through the oil channel of each device and blow dry with a syringe through one of the outlets (HFE 7500 easily wets out of most plastic and glass dispensers, so be gentle and slow). IF MAKING DROPLET DEVICES THIS STEP IS MANDATORY.

- OPTIONAL: If placing electrodes within a few hours, this is not necessary. Within 15 minutes of pressing together, flow some **0.1 M** 3-mercaptopropyltrimethoxysilane in acetonitrile through the electrode channels and allow it to sit under a hood until it has evaporated (~1 hr). The compound is very pungent and should not leave a chemical hood under any circumstance..

- One at a time, set the device on a hotplate set between 160-180 ^{o}C. The device has a tendency to bend with the thinner cover slips; press the middle of the device down the flat ended tweezers with just enough force to keep it flat and no more.
- Cut a few small pieces (2-3 mm) of solder wire (Typically used: 52 In 48 Sn), and using tweezers, press into the electrode inlet. If the channels have been properly coated, it should shoot through quickly and uniformly. If not, add a little more to the other end of the channel (Adding the wire often adds enough pressure to fill parts you missed).

- Using small, equal sections of 1000 V wire (violet), strip 3-4 mm on each end and place into the electrode channels, making sure it reaches the bottom and makes proper contact with the solder. It often helps to twist the ends of the wire to prevent the small pieces from penetrating the PDMS and becoming stuck.
- At this point you should check to make sure the connection has been made using a multimeter.
- If the connection has been made, mix up a small amount of 2-part epoxy and coat around the wire/PDMS contacts. Make sure to spread some up a small length of the wire to prevent liquid from getting in.
- If the connection has not been made, add more solder or apply some pressure to the holes to get it to flow through more uniformly.
- Once the adhesive has been applied, check the connections. Allow it to fully dry per the instructions. After it has dried, check the connections again.

Additional notes:

Wear gloves for all parts.

Blow off any visible dust with N_2.

Clean anything that comes into contact with the PDMS with IPA.

Training required:

UV Exposure tool/Mask Aligner (Karl Suss MJB3,4)

PlasmaStar RIE (O_2)

Laurel Spin coater

Pirahna etching, Nanostrip

Clean room procedures

A.2 Microfluidic Operation Protocol

ALL SOLUTIONS 0.2 UM FILTERED (unless small quantities).

Solutions:

1. Buffer: 0.1-1% BSA, 16-18% Optiprep in HHBSS (no metals, no phenol red).
    a. Keep in fridge.
2. Oil: FC40 or HFE7500 with appropriate concentration of fluorosurfactant (RAN Biotechnologies).

Equipment:

1. Turn on laser: Turn key.

a. Press ‘Output’ on TEC: Wait until settled to 25 ºC.

b. Press ‘Output’ on LASER. (No higher than 500mA, ~180-240 mA has generally resulted in the right power depending on beam size adjustments.).

2. Turn on Oscilloscope (hooked up to HV supply)
3. Turn on function generator and recall sort parameters.
4. Turn on PMT power box (gains are pre-adjusted to get equivalent signal from PMT 1 & 3 and 2 & 4, do this with beads or dye in droplets).

Device:

1. Run IPA/EtOH through oil tubing to waste, DI (or chelex) water, buffer through micro-tubing to waste, dry 2 minutes high pressure. Use syringe to run IPA/EtOH through waste tubing and dry.
2. BSA treatment (optional)
3. Blow dry ~10 min (5 PSI+).
4. CAREFULLY - Insert all tubing: Cell inlet > reagent inlet > oil inlet. Do not inset Keep outlet and waste outlet until timing has been roughly established. Make sure that outlet tubing is only gently placed inside (Do not jam into the coverslip).
5. Connect power to electrodes (1 = Ground (positive), 2 = Negative). Do not turn on HV supply until ready to start sorting.
6. Secure device to platform with magnets.

Microcontroller/Software:

1. Turn on DAQ32 program (DAQ32_PC_Interface.exe).
2. Turn on Labview Data acquisition program.
3. Turn on camera software.
4. Plug in microcontroller microUSB (power).
5. Click ‘Open port’ on DAQ32 interface for COM that microcontroller is on.
6. Click ‘Show’ next to scope A, B (show relevant channels, only 3 channels per scope).
    1. Channel 5 is the TTL signal.
7. Set parameters.
8. Click ‘Write Settings’. This starts the program.

. If the program glitches (happens when it gets too high of a signal):

1. Close Port
2. Unplug/Replug USB cable
3. Open port
4. Write Settings

Running the Experiment:

1. Align device with knobs until within view of camera (if not done already).

a. Pan around and check for clogs.

2. Get laser spots into position by moving platform/adjusting device position.
3. Set sort parameters on function generator.

. TREK HV amp multiplies voltage by ~100.

4. ORDER IS IMPORTANT HERE: Turn on oil pressure (higher than you plan to use it. Easier to start fast and slow down than to start slow for high resistance devices). Turn on reagent pressure and cell pressure higher than the oil pressure (wait for it to reach the device). Try to do this so they arrive nearly simulataneously. Work on getting even flow for your reagent and cell channels. Once droplet generation is achieved, adjust oil pressure to desired speed and attempt to correct droplet size/spacing by decreasing Cell and Reagent pressures (alternate small turns for both to maintain focus). Check timing using timing histogram until you get where you want.
5. Insert outlet tubing and check speed.

6. Watch for fluctuations in timing and correct.
7. When ready to start sorting, turn on sorting signal and adjust voltage until you see sorting and use those parameters going forward.

Ending experiment:

1. Allow experiment to run for a few minutes past the end to allow droplets to reach the reservoirs.
2. Add recovery media to the top of the cells (or gDNA extraction buffer)
3. Add emulsion breaking chemical (SIGMA H1604)
    1. Sit for a few minutes
4. Spin @ 50g for 1-2 min to separate phases
5. Carefully pull off supernatant (aqueous).
6. If gDNA extraction, add proteinase K and incubate overnight @ 37^{o}C.
    1. gDNA extraction and PCR amplification protocols in Kyle Carter's thesis.
7. Discard μfluidic chip in bio-waste (feel free to try to reuse if not two phase)
8. Run EtOH/IPA through tubing first (H_2O or bleach may cause cells to burst). Then H_2O or Bleach -> H_2O and dry.

Appendix B - Code

B.1 Microcontroller code

```
#include "mbed.h"
#include "adc.h"
#include "main.h"
#include "filtering.h"
#include "USBSerial.h"

//settings - set to default values
float FRET_threshold=0;            //FRET threshold , a non zero number turns on fret sorting
float FRET_thresholdUpper = 10;
float threshold = 200;             //threshold in adc counts - ranges from 0 to 4092
uint32_t sorting_delay_us=40;      //sorting delay - time to turn on sorting signal after a peak is detected
uint32_t sorting_delay_off_us=70;  //sorting delay off - time to turn off the sorting signal after a peak is detected
float sorting_delay=0.04;          //sorting delay in seconds
float sorting_delay_off=0.07;      //sorting delay in seconds must be greater thant sorting_delay
uint32_t sample_delay_us=200;      //time between adc samples in us
float sample_delay_seconds=((float)sample_delay_us)/((float)1000000);  //time between adc samples in s. equal to 1/sampling rate
bool sortOnChannel3=true;
int pwmPeriod_us = 100;
int pwmPulseWidth_us = 50;
bool sendPeakData = false;

int pwmStirrerMotorPulseWidth_us = 50;
```

```
bool useMedianFilter;


bool computerConnected;
bool computerConnected2;



//Timer
Timer t;

//PWM - defines the sorting signal
PwmOut myPwmOut(p21);

//Stirrer Motor
PwmOut myStirrerMotor(p22);

DigitalOut TTL_sortingSignal(p20);

//MODSERIAL pc(USBTX,USBRX);

USBSerial serial;


//booleans to control program flow
bool data;            //used to signal that there is new data from the ADC to process - true when there is new data
bool in_peak1=false;    //used to signal that we are currently "in a peak" on adc 1 - true when we are in a peak
bool in_peak2=false;    //used to signal that we are currently "in a peak" on adc 2 - true when we are in a peak
bool in_peak3=false;    //used to signal that we are currently "in a peak" on adc 3 - true when we are in a peak
bool in_peak4=false;    //used to signal that we are currently "in a peak" on adc 4 - true when we are in a peak

bool peakDetected1 = false;
bool peakDetected2 = false;
bool peakDetected3 = false;
bool peakDetected4 = false;

int peak_index_counter1;
int peak_index_counter2;
int peak_index_counter3;
int peak_index_counter4;
```

```
int peak_array_index_ch1=0;
int peak_array_index_ch2=0;
int peak_array_index_ch3=0;
int peak_array_index_ch4=0;

Peak peak_array_ch1[20];
Peak peak_array_ch2[20];
Peak peak_array_ch3[20];
Peak peak_array_ch4[20];

uint16_t peakDataBuffer1[500];
uint16_t peakDataBuffer2[500];
uint16_t peakDataBuffer3[500];
uint16_t peakDataBuffer4[500];


const int firstSpotFRETbufferSize=100;
float firstSpotFRETbuffer[100];
int firstSpotFRETbufferIndex;
int firstSpotFRETbufferIndexMatching;

//peak pair matching
uint16_t second_peak_min_delay_ms=40;
uint16_t second_peak_max_delay_ms=70;
float second_peak_min_delay=0.04;
float second_peak_max_delay=0.07;
Timeout secondSpotMinDelayTime[100];
Timeout secondSpotMaxDelayTime[100];


volatile int searchForSecondSpot=0;

int dataPointsBuffered=0;
bool dataBufferLock;
volatile ISRdata ISRdata_point[100];         //stores the data of the current ADC result
volatile int numBufferedDataPoints=0;

bool isrBufferLock=false;
ISRdata *ISRdata_point_pointer; //used to pass the data of the current ADC results to other data
processing functions

uint16_t filter_Buffer_1[3];    //used to store the adc data for the median filter for adc 1
uint16_t filter_Buffer_2[3];    //used to store the adc data for the median filter for adc 2
uint16_t filter_Buffer_3[3];    //used to store the adc data for the median filter for adc 3
uint16_t filter_Buffer_4[3];    //used to store the adc data for the median filter for adc 4
```

```
Ticker adcTicker;              //used to trigger ADC read events at a specific time interval
Timeout sortingSignalOn1[10];   //An array of Timeout objects used to start and stop the sorting signal
Timeout sortingSignalOff1[10];


Ticker signalGeneratorTest;

bool sendReportFilpper;

int peak_packet_data_marker=1;

bool peakDataReadyToSend = false;


Timeout peakPairMatcher;
int peakMatchTime = 1500; //time in us allowed for a peak on ch1 and ch2 or on ch3 and ch4 to be matched


uint16_t sorting_signal_indicator=0;    //used to keep track of when the sorting signal is on or off, when the sorting signal is on =1 and when its off ==0
int lastSortIndex;
int sorting_signal_index1=0;

int f_data_index=0;                             //an index variable to keep track of where we are in the filtered data buffer
ISRdata f_data_buffer[1000];                        // a data buffer to store filtered data and use within the main loop for data processing (ie peak detection, FRET ratios.....), holds the last 1000 data points

void ADCTimerInterrupt()
{

   if(computerConnected2) {


       dataBufferLock=true;
       ISRdata_point[dataPointsBuffered].adc_value1=data_of_pin(p16);  //read the ADC value off of pin 16
       ISRdata_point[dataPointsBuffered].adc_value2=data_of_pin(p17);  //read the ADC value off of pin 17
       ISRdata_point[dataPointsBuffered].adc_value3=data_of_pin(p18);  //read the ADC value off of pin 16
       ISRdata_point[dataPointsBuffered].adc_value4=data_of_pin(p19);  //read the ADC value off of pin 17
```

```
        //ISRdata_point_pointer=&ISRdata_point;       //create a pointer to this data so we can
access it from other functions
        dataPointsBuffered++;
        //data=true;                          //turn on the signal to indicate that there is new data to read
in the main function loop
        dataBufferLock=false;

    }

}


int main()
{

    serial.attach(&packetRecieved);
    wait(0.5);

    searchForSecondSpot=0;

    //setup PWM
    myPwmOut.period_us(100);    //set pwm period
    myStirrerMotor.period_us(100);

    //setup the ADC in burst mode and attach a tiker to sample at a predefined rate
    init_ADC(180000, 1);                                //initialize the ADC
    setupADC(p16,1);                                    //setup the ADC on pin 16
    setupADC(p17,1);                                    //setup the ADC on pin 17
    setupADC(p18,1);                                    //setup the ADC on pin 18
    setupADC(p19,1);                                    //setup the ADC on pin 19

    LPC_ADC->ADCR |= (1 << 16);                         //enable burst mode, so the ADC on the
microcontroller is constantly generating new results as fast as possible that we can read at any
time
    wait(0.5);                                  //found we need to add this pause for some reason -
not sure why?

    uint16_t packet_size=64;                            //the number of bytes in the outgoing data
packet to be sent to the computer
    uint8_t send_report[packet_size];
    uint8_t send_report2[packet_size];
    uint8_t peak_data_send_report[packet_size];

    int testCounter=1;
```

```
    //sorting_delay=((float)sorting_delay_ms)/1000;             //in seconds
    //sorting_delay_off=((float)sorting_delay_off_ms)/1000;     //in seconds must be greater thant
sorting_delay
    int mycount = 0;
    numBufferedDataPoints=0;

    //signalGeneratorTest.attach_us(&sort,300000);
    //wait(0.5);


    adcTicker.attach_us(&ADCTimerInterrupt,sample_delay_us);    //attatch a function to be
called to read the ADC at a specified interval - effectively setting the sampling rate
    wait(0.5);



    while(1) {

        if(computerConnected)
            computerConnected2=true;
        if(dataPointsBuffered>0) {
            while(dataBufferLock);
            //dataBufferLock=true;
            dataPointsBuffered--;
            if(useMedianFilter==true)
            {
                getFilteredData();
            }
            else
            {
                getRawData();
            }

            //dataBufferLock=false;


            if((f_data_buffer[f_data_index].adc_value1>threshold)&&(!in_peak1)) {       //if we are
just entering a peak on adc 1

                in_peak1=true;


                peak_index_counter1=0;
                peakDataBuffer1[peak_index_counter1] = f_data_buffer[f_data_index].adc_value1;
            }
```

```
        if(in_peak1) {                                          //if we are in peak 1
            peak_index_counter1++;
            peakDataBuffer1[peak_index_counter1] = f_data_buffer[f_data_index].adc_value1;
        }
        if(in_peak1 && (f_data_buffer[f_data_index].adc_value1<threshold)) {        //if we are
leaving a peak 1
            in_peak1=false;

            peak_array_ch1[peak_array_index_ch1].width = peak_index_counter1;
            peak_array_ch1[peak_array_index_ch1].height =
max_array(peakDataBuffer1,peak_index_counter1);

            if(peak_array_index_ch1==9||peak_array_index_ch1==19) {
                peakDataReadyToSend=true;
            }
            if(peak_array_index_ch1==19) {
                peak_array_index_ch1=0;
            } else {
                peak_array_index_ch1++;
            }
            if(!sortOnChannel3) {
                peakDetected1 = true;
                peakPairMatcher.attach_us(&matchFRETpeaksExpiration, peakMatchTime);
            }
        }
        if((f_data_buffer[f_data_index].adc_value2>threshold)&&(!in_peak2)) {       //if we are
just entering a peak on adc 2
            in_peak2=true;

            peak_index_counter2=0;
            peakDataBuffer2[peak_index_counter2] = f_data_buffer[f_data_index].adc_value2;
        }
        if(in_peak2) {                                          //if we are in peak 2
            peak_index_counter2++;
            peakDataBuffer2[peak_index_counter2] = f_data_buffer[f_data_index].adc_value2;
        }
        if(in_peak2 && (f_data_buffer[f_data_index].adc_value2<threshold)) {        //if we are
leaving a peak on adc 2
            in_peak2=false;
            peak_array_ch2[peak_array_index_ch2].width = peak_index_counter2;
            peak_array_ch2[peak_array_index_ch2].height =
max_array(peakDataBuffer2,peak_index_counter2);

            if(peak_array_index_ch2==19) {
                peak_array_index_ch2=0;
```

```
            } else {
               peak_array_index_ch2++;
            }
            if(!sortOnChannel3) {
               peakDetected2 = true;
               peakPairMatcher.attach_us(&matchFRETpeaksExpiration, peakMatchTime);
            }

         }

         if((!sortOnChannel3) && peakDetected1 && peakDetected2) {
            int lastIndex1=peak_array_index_ch1-1;
            if(lastIndex1<0)
               lastIndex1=19;
            int lastIndex2=peak_array_index_ch2-1;
            if(lastIndex2<0)
               lastIndex2=19;

            float FRET_spot1 =
((float)peak_array_ch1[lastIndex1].height/(float)peak_array_ch2[lastIndex2].height);
            firstSpotFRETbuffer[firstSpotFRETbufferIndex]=FRET_spot1;


secondSpotMinDelayTime[firstSpotFRETbufferIndex].attach(&secondSpotStartSearch,second_
peak_min_delay);

secondSpotMaxDelayTime[firstSpotFRETbufferIndex].attach(&secondSpotEndSearch,second_p
eak_max_delay);


            if(firstSpotFRETbufferIndex==99) {
               firstSpotFRETbufferIndex=0;
            } else {
               firstSpotFRETbufferIndex++;
            }


            //if(FRET_ratio>FRET_threshold && FRET_ratio<FRET_thresholdUpper)
            //{
            //   sort();
            //}
            peakDetected1 = false;
            peakDetected2 = false;
            peakPairMatcher.detach();
         }
```

```
        if((searchForSecondSpot > 0) || sortOnChannel3)  {


            if((f_data_buffer[f_data_index].adc_value3>threshold)&&(!in_peak3)) {       //if we
are just entering a peak on adc 3

               in_peak3=true;


               peak_index_counter3=0;
               peakDataBuffer3[peak_index_counter3] = f_data_buffer[f_data_index].adc_value3;
            }

            if(in_peak3) {                                          //if we are in peak 3
               peak_index_counter3++;
               peakDataBuffer3[peak_index_counter3] = f_data_buffer[f_data_index].adc_value3;
            }
            if(in_peak3 && (f_data_buffer[f_data_index].adc_value3<threshold)) {       //if we are
leaving a peak 3
               in_peak3=false;

               peak_array_ch3[peak_array_index_ch3].width = peak_index_counter3;
               peak_array_ch3[peak_array_index_ch3].height =
max_array(peakDataBuffer3,peak_index_counter3);

               if(peak_array_index_ch3==9||peak_array_index_ch3==19) {
                  peakDataReadyToSend=true;
               }
               if(peak_array_index_ch3==19) {
                  peak_array_index_ch3=0;
               } else {
                  peak_array_index_ch3++;
               }
               if(sortOnChannel3) {
                  sort();
               }
               if(!sortOnChannel3) {
                  peakDetected3 = true;
                  peakPairMatcher.attach_us(&matchFRETpeaksExpiration2, peakMatchTime);
               }

            }

            if((f_data_buffer[f_data_index].adc_value4>threshold)&&(!in_peak4)) {       //if we
are just entering a peak on adc 4
```

```
            in_peak4=true;

            peak_index_counter4=0;
            peakDataBuffer4[peak_index_counter4] = f_data_buffer[f_data_index].adc_value4;
          }
          if(in_peak4) {                                    //if we are in peak 4
            peak_index_counter4++;
            peakDataBuffer4[peak_index_counter4] = f_data_buffer[f_data_index].adc_value4;
          }
          if(in_peak4 && (f_data_buffer[f_data_index].adc_value4<threshold)) {       //if we are
leaving a peak on adc 4
            in_peak4=false;
            peak_array_ch4[peak_array_index_ch4].width = peak_index_counter4;
            peak_array_ch4[peak_array_index_ch4].height =
max_array(peakDataBuffer4,peak_index_counter4);

            if(peak_array_index_ch4==19) {
              peak_array_index_ch4=0;
            } else {
              peak_array_index_ch4++;
            }
            if(!sortOnChannel3) {
              peakDetected4 = true;
              peakPairMatcher.attach_us(&matchFRETpeaksExpiration2, peakMatchTime);
            }

          }

          if((!sortOnChannel3) && peakDetected3 && peakDetected4) {

            int lastIndex3=peak_array_index_ch3-1;
            if(lastIndex3<0)
              lastIndex3=19;
            int lastIndex4=peak_array_index_ch4-1;
            if(lastIndex4<0)
              lastIndex4=19;

            float FRET_spot2 =
((float)peak_array_ch3[lastIndex3].height/(float)peak_array_ch4[lastIndex4].height);

            float FRET_RATIO=
FRET_spot2/firstSpotFRETbuffer[firstSpotFRETbufferIndexMatching];

            secondSpotMaxDelayTime[firstSpotFRETbufferIndexMatching].detach();
             secondSpotEndSearch();
```

```
            if(FRET_RATIO>FRET_threshold && FRET_RATIO<FRET_thresholdUpper) {
               sort();
            }


            peakDetected3 = false;
            peakDetected4 = false;

         }

      }
```

```
send_report[0+(8*mycount)]=(uint8_t)(((f_data_buffer[f_data_index].adc_value1>>7))&0x1F)|0
x80;

send_report[1+(8*mycount)]=(uint8_t)((f_data_buffer[f_data_index].adc_value1)&0x7F);

send_report[2+(8*mycount)]=(uint8_t)(((f_data_buffer[f_data_index].adc_value2>>7)&0x1F)|((
(uint8_t)sorting_signal_indicator)<<5));

send_report[3+(8*mycount)]=(uint8_t)((f_data_buffer[f_data_index].adc_value2)&0x7F);

send_report[4+(8*mycount)]=(uint8_t)(((f_data_buffer[f_data_index].adc_value3>>7))&0x1F);

send_report[5+(8*mycount)]=(uint8_t)((f_data_buffer[f_data_index].adc_value3)&0x7F);

send_report[6+(8*mycount)]=(uint8_t)(((f_data_buffer[f_data_index].adc_value4>>7))&0x1F);

send_report[7+(8*mycount)]=(uint8_t)((f_data_buffer[f_data_index].adc_value4)&0x7F);


      mycount++;


      if(mycount == 8) {
         //send_report[0]|= 0x80;


         serial.writeBlock(&send_report[0], 64);
```

```
            mycount = 0;

            //testCounter=1;

         }

         if(((mycount==8) && peakDataReadyToSend) && sendPeakData) {
            for(int j=0; j<10; j++) {
               int l;
               if(peak_array_index_ch1<9) {
                  l=10;
               } else {
                  l=0;
               }
               peak_data_send_report[4+(6*j)]=  peak_array_ch1[l+j].width;
               peak_data_send_report[5+(6*j)]= (peak_array_ch1[l+j].height>>8)&0x0F;
               peak_data_send_report[6+(6*j)]= (peak_array_ch1[l+j].height)&0xFF;
               peak_data_send_report[7+(6*j)]=  peak_array_ch2[l+j].width;
               peak_data_send_report[8+(6*j)]= (peak_array_ch2[l+j].height>>8)&0x0F;
               peak_data_send_report[9+(6*j)]= (peak_array_ch2[l+j].height)&0xFF;
            }
            peak_data_send_report[0] = 128;
            peak_data_send_report[1] = 128;
            peak_data_send_report[2] = 0;
            peak_data_send_report[3] = 0;
            serial.writeBlock(&peak_data_send_report[0], 64);
            peakDataReadyToSend=false;
         }

         endDataTasks();

      }

   }

}

void getFilteredData()
{
   //f_data_buffer[f_data_index].adc_value1 = medianFilter(filter_Buffer_1,
ISRdata_point_pointer->adc_value1);
   //f_data_buffer[f_data_index].adc_value2 = medianFilter(filter_Buffer_2,
ISRdata_point_pointer->adc_value2);
   f_data_buffer[f_data_index].adc_value1 = medianFilter(filter_Buffer_1,
ISRdata_point[dataPointsBuffered].adc_value1);
```

```
   f_data_buffer[f_data_index].adc_value2 = medianFilter(filter_Buffer_2,
ISRdata_point[dataPointsBuffered].adc_value2);
   f_data_buffer[f_data_index].adc_value3 = medianFilter(filter_Buffer_3,
ISRdata_point[dataPointsBuffered].adc_value3);
   f_data_buffer[f_data_index].adc_value4 = medianFilter(filter_Buffer_4,
ISRdata_point[dataPointsBuffered].adc_value4);
}

void getRawData()
{
   f_data_buffer[f_data_index].adc_value1 = ISRdata_point[dataPointsBuffered].adc_value1;
   f_data_buffer[f_data_index].adc_value2 = ISRdata_point[dataPointsBuffered].adc_value2;
   f_data_buffer[f_data_index].adc_value3 = ISRdata_point[dataPointsBuffered].adc_value3;
   f_data_buffer[f_data_index].adc_value4 = ISRdata_point[dataPointsBuffered].adc_value4;

}

void endDataTasks()
{
   data=false;
   f_data_index++;

   if(f_data_index>999) {
      f_data_index=0;
   }
}

void sortingSignalOn()
{
   if(sorting_signal_indicator==1) {
      sortingSignalOff1[lastSortIndex].detach();
   }
   sorting_signal_indicator=1;
   myPwmOut.pulsewidth_us(pwmPulseWidth_us);   //turn on pwm  sorting signal
   TTL_sortingSignal=1;                        //make TTL signal on p20 high


}

void sortingSignalOff()
{
   sorting_signal_indicator=0;
   myPwmOut.pulsewidth_us(0);    //turn off pwm sorting signal

   TTL_sortingSignal=0;          //make TTL signal on p20 low
}
```

```
void packetRecieved()
{
   computerConnected2=false;
   computerConnected=false;
   uint8_t float_bytes[4];
   float_bytes[0] = serial._getc();
   float_bytes[1] = serial._getc();
   float_bytes[2] = serial._getc();
   float_bytes[3] = serial._getc();

   FRET_threshold=*(float *)float_bytes;

   float_bytes[0] = serial._getc();
   float_bytes[1] = serial._getc();
   float_bytes[2] = serial._getc();
   float_bytes[3] = serial._getc();

   FRET_thresholdUpper=*(float *)float_bytes;

   threshold = serial._getc()|(serial._getc()<<8);
   sample_delay_us=serial._getc()|(serial._getc()<<8);

   sorting_delay_us=serial._getc()|(serial._getc()<<8);
   sorting_delay_off_us=serial._getc()|(serial._getc()<<8);



   second_peak_min_delay_ms=serial._getc()|(serial._getc()<<8);
   second_peak_max_delay_ms=serial._getc()|(serial._getc()<<8);

   second_peak_min_delay=((float)second_peak_min_delay_ms)/1000; //in seconds
   second_peak_max_delay=((float)second_peak_max_delay_ms)/1000; //in seconds

   pwmPulseWidth_us = serial._getc()|(serial._getc()<<8);
   pwmPeriod_us = serial._getc()|(serial._getc()<<8);

   pwmStirrerMotorPulseWidth_us = serial._getc()|(serial._getc()<<8);

   if((pwmStirrerMotorPulseWidth_us>100)||(pwmStirrerMotorPulseWidth_us<0))
   {
      pwmStirrerMotorPulseWidth_us=0;

   }
```

```
    char sortOnFRET = serial._getc();
    char sendPData =  serial._getc();
    char useFilter = serial._getc();

    if (sortOnFRET == 100) {
        sortOnChannel3 = false;
    } else {
        sortOnChannel3 = true;
    }

    if (sendPData == 100) {
        sendPeakData = true;
    } else {
        sendPeakData = false;
    }

    if (useFilter == 100) {
        useMedianFilter = true;
    } else {
        useMedianFilter = false;
    }



    myStirrerMotor.write(((float)pwmStirrerMotorPulseWidth_us)/100);

    adcTicker.detach();

    sample_delay_seconds=sample_delay_us/1000000;
    adcTicker.attach_us(&ADCTimerInterrupt,sample_delay_us);
    wait(0.5);

    //sorting_delay=((float)sorting_delay_us)/1000; //in seconds
    //sorting_delay_off=((float)sorting_delay_off_us)/1000; //in seconds must be greater thant
sorting_delay




    myPwmOut.period_us(pwmPeriod_us);    //set pwm period

    computerConnected=true;
}

int max_array(uint16_t a[], int num_elements)
{
```

```
    int i, max=0;
    for (i=0; i<=num_elements; i++) {
        if (a[i]>max) {
            max=a[i];
        }
    }
    return(max);
}

void sort()
{

    if (sorting_signal_index1 == 9) {
        sorting_signal_index1 = 0;
        lastSortIndex = 9;
    } else {
        lastSortIndex = sorting_signal_index1;
        sorting_signal_index1++;
    }

    sortingSignalOn1[sorting_signal_index1].attach_us(sortingSignalOn,
            sorting_delay_us);
    sortingSignalOff1[sorting_signal_index1].attach_us(sortingSignalOff,
            sorting_delay_off_us);
}

void secondSpotStartSearch()
{
    searchForSecondSpot=searchForSecondSpot+1;

}
void secondSpotEndSearch()
{

    searchForSecondSpot=searchForSecondSpot-1;

    if(firstSpotFRETbufferIndexMatching==(firstSpotFRETbufferSize-1)) {
        firstSpotFRETbufferIndexMatching=0;
    } else {
        firstSpotFRETbufferIndexMatching++;
    }

}

void matchFRETpeaksExpiration()
{
```

```
    if(peakDetected1 && peakDetected2) {
        peakDetected1 = false;
        peakDetected2 = false;
    }

}

void matchFRETpeaksExpiration2()
{
    if(peakDetected3 && peakDetected4) {
        peakDetected3 = false;
        peakDetected4 = false;
    }

}
```

B.2 Mathematica Code for Anisotropy Calculations

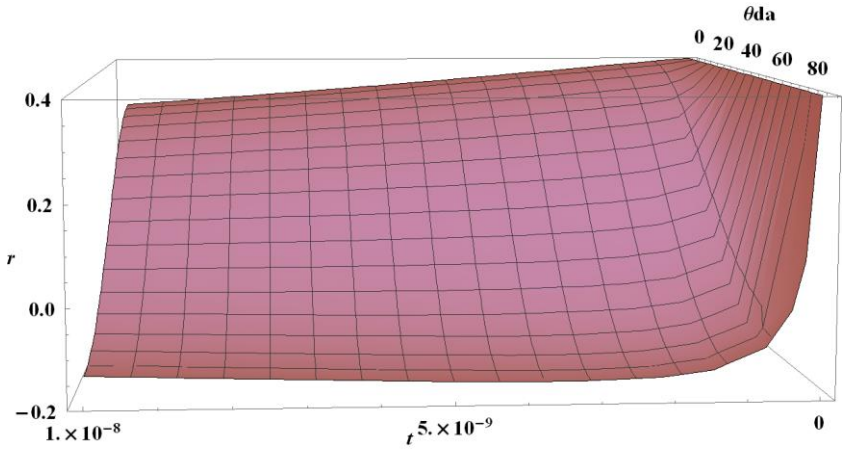
```
(*Variables/Constants*)
F1 = 1;  (*Interacting Fraction*)
F2 = 0.1;
Ro = 4.8*^-9; (*ECFP/Citrine*)
Ra = 4.8*^-9;
B = 30; (*Acceptor-to-Donor Overlap Factor in Acceptor Channel || low overlap*)
B2 = 5.89; (*Acceptor-to-Donor Overlap Factor in Acceptor Channel || Citrine/ECFP*)
kaf = 1/(3.6*^-9); (*Radiative rate - Acceptor || Citrine*)
kfret = (1/(1/kdf))*(Ro/Ra)^6; (*FRET rate*)
kdf = 1/(3*^-9); (*Radiative rate - Donor || ECFP*)
(*θda =  90 Degree; (*Donor-Acceptor TDM angle*)*)
δ = 0.01; (*Absorption cross section Acceptor/Donor @ Donor Excitation*)
(*ANI = 1;*)
(*AI = 1;*)
krot=1/(30*^-9);

(*X= (kfret/(kfret + kdf - kaf))*)

R[t_,θda_]=(2/5)*(((Exp[-(kfret+kaf)*t])*(F1*(1-(B*(kfret/(kfret + kdf - kaf))/2)*(3*(Cos[θda
Degree]^2)-1)*Exp[-krot*t]))+F1*B*(kfret/(kfret + kdf - kaf))*Exp[-kaf*t]*0.5*((3*(Cos[θda
Degree]^2)-1)*Exp[-krot*t])+((1-F1)*Exp[-kdf*t]*Exp[-krot*t])+(B*δ*Exp[-krot*t]*Exp[-
```

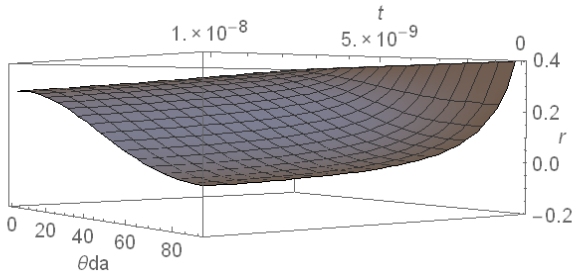
kaf*t]))/((F1*(1-B*(kfret/(kfret + kdf - kaf)))*Exp[-(kfret+kaf)*t])+(F1*B*(kfret/(kfret + kdf - kaf))*Exp[-kaf*t])+((1-F1)Exp[-kdf*t])+(B*δ*Exp[-kaf*t])));

p1=Plot3D[R[t,θda],{t,0,1*10^-8}, {θda,0,90},PlotStyle->RGBColor[0.75,0.61,1.],PlotRange->{-0.2,0.4}, AxesLabel->{t,θda,r},LabelStyle->{FontSize->16,FontFamily->"Times",Black,Bold}]



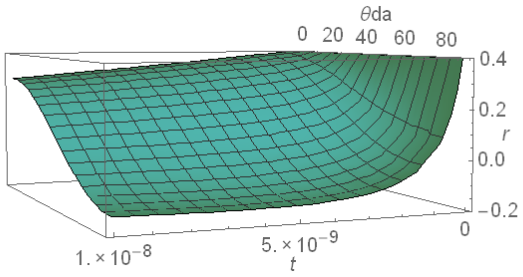
R1[t_,θda_]=(2/5)*(((Exp[-(kfret+kaf)*t])*(F2*(1-(B*(kfret/(kfret + kdf - kaf))/2)*(3*(Cos[θda Degree]^2)-1)*Exp[-krot*t]))+F2*B*(kfret/(kfret + kdf - kaf))*Exp[-kaf*t]*0.5*((3*(Cos[θda Degree]^2)-1)*Exp[-krot*t])+((1-F2)*Exp[-kdf*t]*Exp[-krot*t])+(B*δ*Exp[-krot*t]*Exp[-kaf*t]))/((F2*(1-B*(kfret/(kfret + kdf - kaf)))*Exp[-(kfret+kaf)*t])+(F2*B*(kfret/(kfret + kdf - kaf))*Exp[-kaf*t])+((1-F2)Exp[-kdf*t])+(B*δ*Exp[-kaf*t])));

p2=Plot3D[R1[t,θda],{t,0,1*10^-8}, {θda,0,90},PlotStyle->RGBColor[0.5`,0.61`,1.`],PlotRange->{-0.2,0.4}, AxesLabel->{t,θda,r}]

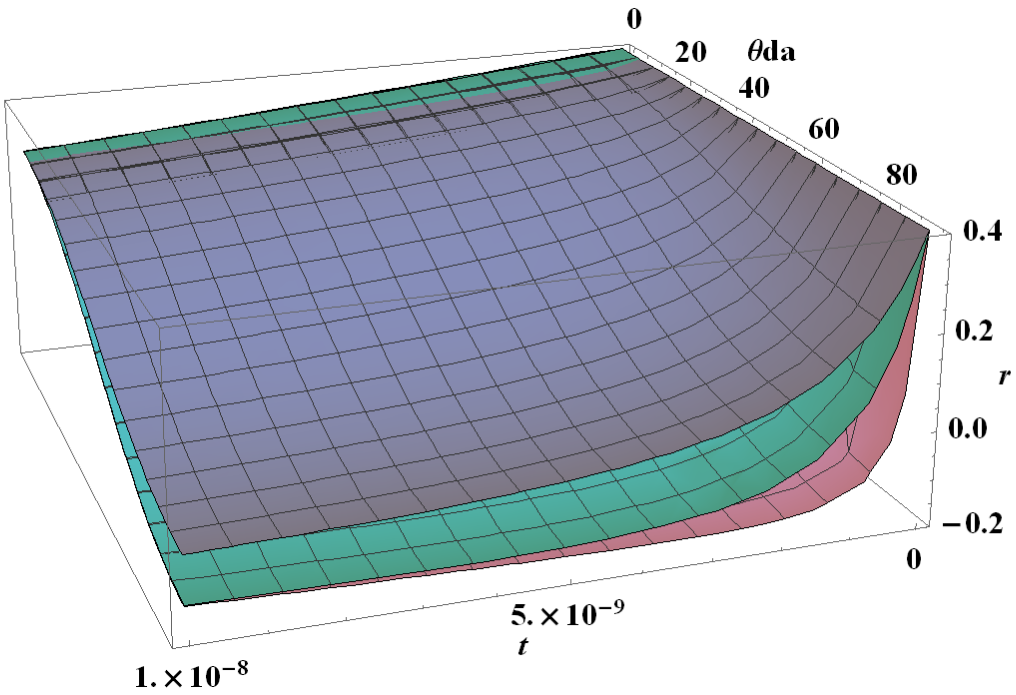


R2[t_,θda_]=(2/5)*(((Exp[-(kfret+kaf)*t])*(F1*(1-(B2*(kfret/(kfret + kdf - kaf))/2)*(3*(Cos[θda Degree]^2)-1)*Exp[-krot*t]))+F1*B2*(kfret/(kfret + kdf - kaf))*Exp[-kaf*t]*0.5*((3*(Cos[θda Degree]^2)-1)*Exp[-krot*t])+((1-F1)*Exp[-kdf*t]*Exp[-krot*t])+(B2*δ*Exp[-krot*t]*Exp[-kaf*t]))/((F1*(1-B2*(kfret/(kfret + kdf - kaf)))*Exp[-(kfret+kaf)*t])+(F1*B2*(kfret/(kfret + kdf - kaf))*Exp[-kaf*t])+((1-F1)Exp[-kdf*t])+(B2*δ*Exp[-kaf*t])));

p3=Plot3D[R2[t,θda],{t,0,1*10^-8}, {θda,0,90},PlotStyle->RGBColor[0.3`,0.8`,1.`],PlotRange->{-0.2,0.4}, AxesLabel->{t,θda,r}]



pa=Show[p1,p2,p3]


0
20
θda
40
60
80
0.4
0.2
r
0.0
−0.2
0
5. × 10^−9
t
1. × 10^−8

B.3 Mathematica Code for Microfluidic Device

****Adapted from code by Dr. Jennifer Lubbeck****

2 D device (uniform height)
Resistance:

R = Resistance (in units of N s m^-5)
\[Eta] = Viscosity (in units of N s (m^-2))
x = Channel Length (in units of m)
w = Channel Width (in units of m)
h = Channel Height (in units of m)
Q = Flow Rate
Vmax = Max Velocity
P = Pressure (in units of Psi)

NB: Widths are assumed to be independent of x.

```
R[x_, w_, h_] := 12 \[Eta] x/((h^3 w) (1 - 0.630 h/w))
```

Resistance of center input channels :

```
h = 45 10^-6 ;
xc = 47.646 10^-3;
xmix = 0 10^-3;
wc = 50 10^-6;
\[Eta] = 0.00089;

Rc = N[R[xc, wc, h] + R[xmix, wc, h]]
```

2.5793*10^14

Resistance of oil input channels :

```
xs = 43.2795272 10^-3;
ws = 50 10^-6;
\[Eta] = 0.00124;

Rs = N[R[xs, ws, h]]
```

3.2643*10^14

Total input resistance :

Rinput = 1/(1/Rc + 2/Rs)

9.9961*10^13

Resistance of delay

xm = 221.744 10^-3;
wm = 100 10^-6;

Rm = N[R[xm, wm, h]]

5.0536*10^14

Resistance of outputs :

xkj = 0.6697 10^-3;
xk = 8.2904128 10^-3;
xwj = 0.6526 10^-3;
xw = 2.926 10^-3;
wo = 200 10^-6;
ww = 140 10^-6;

Ro = N[1/(R[xkj, wm, h] + R[xk, wo, h]) + 1/(R[xwj, ww, h] + R[xw, wo, h])]

3.7376*10^-13

Total Output resistance :

Routput = 1/Ro

2.67551*10^12

Total Device Resistance :

TotalDeviceResistance = N[Rinput + Rm + Routput]
ResistanceRatio = (Routput + Rm)/Rinput

6.07997*10^14

5.08234

Necessary Pressure for velocity of (input below) :

Vmax = 0.03;

In Helle - Shaw limit : FOR RECTANGULAR CHANNELS THIS IS ONLY APPROXIMATE

Q[h_, w_, v_] := 2 h w v/3

FlowRate = N[Q[h, wm, Vmax]]

9.*10^-11

P = FlowRate*TotalDeviceResistance/6894.7

7.93649